4-27-2020 10:00 AM

Design Wind Loads for Air-Permeable Multilayer Cladding Systems

Connell S. Miller, *The University of Western Ontario*

Supervisor: Kopp, Gregory A., *The University of Western Ontario*
A thesis submitted in partial fulfillment of the requirements for the Doctor of Philosophy degree in Civil and Environmental Engineering
© Connell S. Miller 2020

Abstract

Monetary losses from severe wind storms continue to rise despite improvements to building codes. This is because air-permeable multilayer cladding systems such as vinyl siding and roof pavers are a major component of the monetary losses in severe wind storms, but there are not legal requirements for these products. Some air-permeable multilayer products have manufacturing standards that deal with design loads by eliminating the cavity flow and applying a pressure equalization factor to account for the reduction in net load caused by this cavity flow. The objective of this thesis was to develop design guidelines for wind loads on air-permeable multilayer cladding systems.

A multi-chamber airbox system for testing air-permeable multi-layer cladding was developed and compared to a benchmark study performed by the Insurance Institute for Business & Home Safety by implementing a latex barrier system and examining the control strategy for the Pressure Loading Actuators. The results indicate that using multi-chamber, pressure-based, testing to obtain wind loads for air-permeable, multi-layer wall systems with flexible cladding is sufficiently accurate. It also showed that the pressure equalization factor (the ratio of the net pressure over the external pressure) for vinyl siding is inaccurate, which could be leading to the common failures seen in damage surveys.

Another issue with the codification of the wind loads on air-permeable multilayer systems is that design approaches to determine loads on different types of building cladding elements can vary significantly by product type, even though they may have similar geometries. Using the full-scale wind tunnel at the Insurance Institute for Business & Home Safety, external and net wind loads on two discontinuous metal roof systems were measured. The results indicate that cavity pressures in air-permeable multilayer cladding, such as discontinuous metal roofs are approximately uniform across individual panels and closely related across multiple panels which share the same cavity. The testing also showed that there is a short time lag between the peak net loads and the peak spatial gradient of the external pressure across the cladding elements. The two types of discontinuous metal roofing products, which have significantly different cavity geometries, have similar ratios between the net and external wind loads. This suggests that design values have the potential to be fairly simple for typical residential building products, in spite of fairly complex aerodynamics.

With that goal in mind, a unified approach to the pressure equalization factor for air-permeable multilayer cladding was created by enveloping the worst case pressure equalization factor values for each type and taking into account the effect that exposed edges and parapets have on the net loads. The design recommendations could be used to fill the current gap in knowledge in air-permeable multilayer cladding in building codes such as ASCE 7 or NBCC.

Keywords

Summary for Lay Audience

Monetary losses from severe wind storms (including downbursts and tornadoes) continue to rise despite improvements to building codes. This is because cladding failures are a major portion of the monetary losses in these severe wind storms. Cladding is a broad term used to describe the outer layer of a building that protects it from the elements. It is present on most buildings and comes in many variations. Air-permeable (has gaps for drainage and installation purposes) multilayer (does not sit flush to the surface) cladding is one of the most common types of building material in North America. It includes such materials as vinyl siding, roof pavers, and asphalt shingles. Despite it being such a common type of building material, there is little guidance in the building code for how to design these types of cladding. This is because the air-permeability of this cladding makes determining the wind loads challenging.

The objective of this thesis was to develop a design guideline for the wind loads for all types air-permeable multilayer systems. To do this, manufacturing standards that have attempted to calculate the wind loads on this type of cladding were examined to highlight the current inaccuracy of the wind loads. Then, the aerodynamics of air-permeable multilayer cladding were examined to see what causes peak wind loads on these systems. Finally, many types of air-permeable multilayer systems were examined to develop a unified approach to calculating the design wind loads on these systems.

Co-Authorship Statement

Three full Chapters (Chapter 2, Chapter 3, and Chapter 4) and portions of Chapter 1 used in this integrated article thesis are co-authored by myself, my supervisor Dr. Gregory Kopp, and others. For these articles, all of the experiments, analyses, and the preparation of the manuscripts were carried out by me under the supervision of Dr. Gregory Kopp. The co-authorship is as follows:

Chapter 2: A multichambered, pressure-based test method to determine wind loads on air-permeable multilayer cladding systems.

Connell Miller, Gregory Kopp, Murray Morrison, Gary Kemp, and Nick Drought
Published in *Frontiers of the Built Environment* on February 10, 2017

In this paper, I was primarily responsible for the experiments and direct analysis of the experimental data, along with the preparation of the manuscript. Dr. Gregory Kopp assisted in the analysis of the data and provided significant instruction and feedback in the preparation of the article. Dr. Murray Morrison contributed information from the full-scale testing at IBHS. Gary Kemp and Nick Drought contributed information about the development of the PLA system.

Chapter 3: Aerodynamics of air-permeable multilayer roof cladding.

Connell Miller, Gregory Kopp, Murray Morrison
Submitted to *Journal of Wind Engineering & Industrial Aerodynamics* on October 20, 2019.

In this paper, I was primarily responsible for the development of the neutral pressure line model, experiments and direct analysis of the experimental data, along with the preparation of the manuscript. Dr. Gregory Kopp assisted in the development of the neutral pressure line model and provided significant instruction and feedback in the preparation of the article. Dr. Murray Morrison was responsible for the setup of the full-scale building and instrumentation.

Chapter 4: A unified approach to the pressure equalization factor.

Connell Miller, Gregory Kopp
Not currently submitted for publication.

In this paper, I was primarily responsible for the synthesis and analysis of the data from pressure equalization studies, along with the preparation of the manuscript. Dr. Gregory Kopp provided significant instruction and feedback in the preparation of the article.

Acknowledgments

It turns out the phrase "it takes a village" is true of graduate studies as well as raising children. Firstly, I'd like to thank my supervisor, Dr. Gregory Kopp. I first began working with Dr. Kopp as an undergraduate student in 2014; six years later and I know I've grown considerably in my research capabilities thanks to his expertise, advice, and patience. Thank you for continuing to push me to challenge myself, and for providing opportunities for learning outside the scope of my Ph.D.

I would also like to thank Dr. Murray Morrison, not only for helping to obtain the data that was instrumental in this thesis, but for providing me with the amazing opportunity to work at the full-scale wind tunnel at the Insurance Institute for Business & Home Safety. Thank you for all your technical assistance and expertise. I'd also like to thank Andrew Klazinga and Randy Van Straaten for their technical expertise, especially at the beginning stages of this work.

On a personal note, I'd like to thank my officemates - especially Emilio Hong, Sarah Stevenson, and Aaron Jaffe, for allowing me to bounce stupid questions and ideas off them for six years. Thank you also for keeping me destressed thanks to "Board Game Fridays".

None of this would be possible without the love & support of my family. Most importantly, I'd like to thank my wife and life partner, Sasha. Thanks to her support, encouragement, and occasional therapy, I was able to accomplish what I previously thought was impossible. Thank you for the countless hours you listened to me ramble about my research. Finally, thank you to my parents, Sheila & Byron, for always pushing me to be better, and to my sisters, Ceilidhe & Molly, for always keeping me grounded.

Table of Contents

List of Tables

List of Figures

Nomenclature

A	area
A_0	area of openings
C_d	discharge coefficient
C_{eq}	pressure equalization coefficient
C_L	orifice loss coefficient
Cp_c	cavity pressure coefficient
Cp_e	external pressure coefficient
Cp_i	internal pressure coefficient
Cp_n	net pressure coefficient
f	Coriolis force
g	force of gravity
G	gap between panels on the outer layer
GCp_c	cavity pressure coefficient (ASCE 7-16)
GCp_e	external pressure coefficient (ASCE 7-16)
GCp_i	internal pressure coefficient (ASCE 7-16)
GCp_n	net pressure coefficient (ASCE 7-16)
h	distance from neutral pressure line
h_p	parapet height
H	height of cavity between layers
$I_u(z)$	turbulence intensity as a function of height
l_e	effective length of the fluid passing through the gap, G
L	panel length
p_{AE}	area-averaged external pressure
p_c	cavity pressure
p_e	external pressure
p_i	internal pressure
p_n	net pressure
p_0	atmospheric pressure
Q_g	flow rate through an opening

r	radius from the center of pressure
R_a	gas constant
σ_u	standard deviation of the longitudinal fluctuating wind
t	time
T	air temperature
U	wind speed
U_H	mean wind speed at the roof height of a building
$\overline{U(z)}$	mean wind speed as a function of height
$\overline{U_{10}}$	mean wind speed at a height of 10m from the ground
U_g	average velocity of flow in the gap, G
x	length
x_{NPL}	location of neutral pressure line
z	height
α	terrain roughness exponent
γ_A	proposed effective area factor
γ_ϵ	proposed exposed edge factor
γ_P	proposed parapet factor
$\delta p/\delta n$	pressure gradient
dU/dt	change in wind speed over time
Δp_e	external pressure difference
ρ	air density
$\rho(A, B)$	Spearman's rho correlation coefficient
τ	system time constant
θ	wind direction

Symbols & Abbreviations

ASTM	American Society for Testing & Materials
ASCE	American Society for Civil Engineers
ATI	Architectural Testing Inc.
BRERWULF	Building Research Establishment's real time wind uniform load follower
C&C	components & cladding
CFM	cubic feet per minute
DMR	discontinuous metal roofing
IBHS	Insurance Institute for Business & Home Safety
IRLBH	Insurance Research Lab for Better Homes
MSU	Mississippi State University
OSB	oriented stand board
PEF	pressure equalization factor
PID	proportional integral derivative
VSD	variable speed drive
VSI	Vinyl Siding Institute

1 Determining Wind Loads on Air-Permeable Multilayer Cladding

1.1 Background

Severe wind storms around the world continue to cause significant economic losses (Munich RE, 2018). While there have been significant advances and successes with building codes, design standards, and construction methods, which have reduced major structural failures (e.g., Gurley & Masters., 2011), losses caused by extreme wind storms continue to grow. These tend to be due to failures of the building envelope and connections, e.g., cladding failures caused by either net pressure loads or wind-borne debris impacts, failures of nailed connections, etc. Entry of rainwater through the resulting openings is a significant source of damage (e.g., Sparks et al., 1994; Gurley & Masters 2011). Where structural members fail in wind storms, they are often due to failure of an envelope component first, such as a window or door that allows internal pressurization. Thus, mitigation of economic losses in wind storms is strongly dependent on enhanced performance of cladding systems and their connections. Figure 1.1 and Figure 1.2 show photographs from damaged residential structures in Dunrobin, Ontario and Nepean, Ontario, respectively, where significant cladding failure occurred, but the structural components of the building are left intact.

Figure 1.1: Photograph of a two-story residential building with significant component and cladding failure in Dunrobin, Ontario taken on September 21, 2018.

Figure 1.2: Photograph of a two-story residential building with significant component and cladding failure in Nepean, Ontario taken on September 21, 2018.

1.2   Air-Permeable Multilayer Cladding

Cladding is a broad term used to describe the outer layer of a building that protects it from the elements. It is present on most buildings and comes in many variations. Air-permeable multilayer cladding is one of the most common types of building material in North America. It includes such materials as vinyl siding, roof pavers, discontinuous metal roofing, and asphalt shingles. A feature of this cladding is that it has an air cavity separating the cladding from the sheathing, studs, and other interior layers. The primary use of this air cavity is for installation purposes and drainage of rainwater. A useful geometric ratio in helping to determine the effect of the air flow through the cavity is the width of its openings in the cladding (G) over the height of the cavity (H). Figure 1.3 shows a sketch of a typical air-permeable multilayer system, along with the definition of these useful geometric parameters. From the diagram, it is clear the geometry is hard to define, and can vary wildly at different locations on the cladding. Based on this, as well as observations made during damage surveys: air-permeable multilayer cladding have three major potential problems when trying to determine the wind load resistance of these products:

- Installation issues – based on the field observations from damage surveys, although installation issues can play a role in specific circumstances, there is not enough evidence to show that they are solely responsible for all air-permeable multilayer cladding failures.

- Inadequate test standards for some building products – this is discussed further in Chapter 2, which examines the inadequacy of the single airbox method detail in ASTM D5206 for the wind load resistance of vinyl siding.

- Inadequate test methods in building codes, wind tunnel test methods, and analytical tools for determining the wind loads on air-permeable multilayer systems.
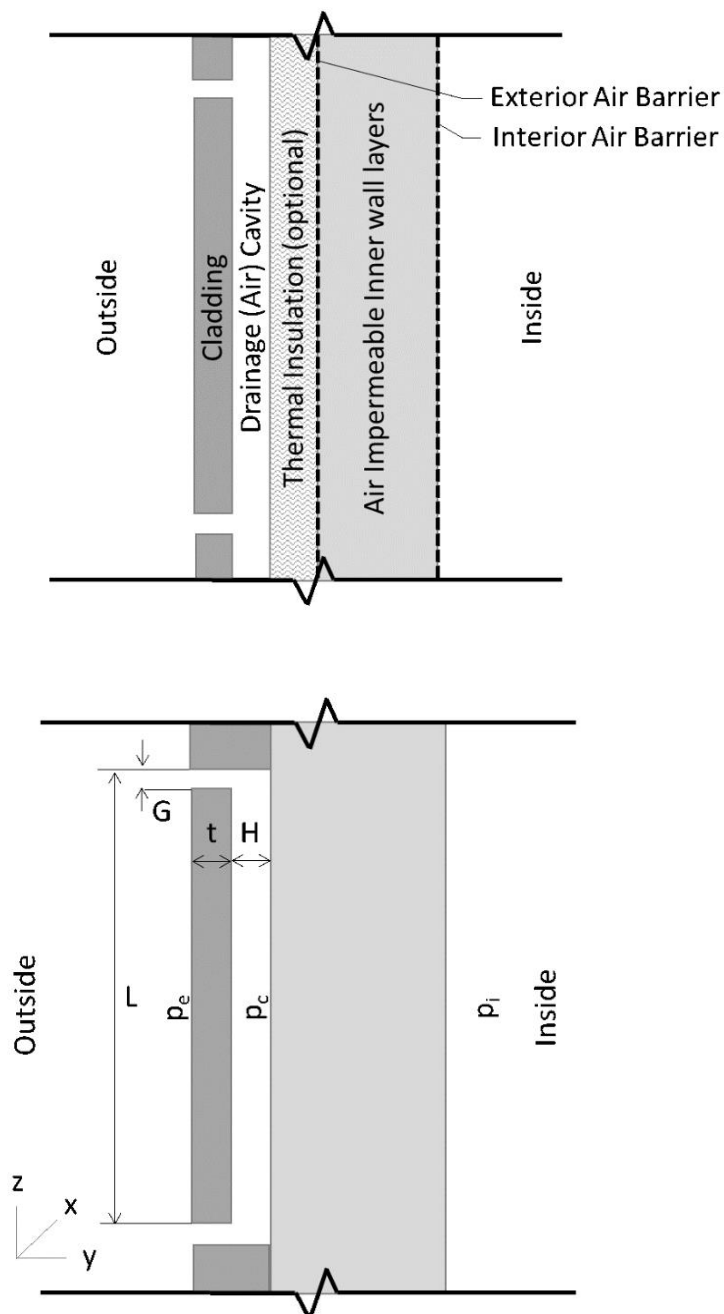
Figure 1.3: A definition sketch of a typical air-permeable multilayer system, along with important geometric parameters, and the location of the air-impermeable inner wall layers (courtesy of Randy Van Straaten, originally published in Van Straaten (2017)).

1.3 External Wind Flow Around Residential Buildings

Wind in the atmosphere is created both by the rotation of the Earth (expressed as the Coriolis effect), and the pressure gradient of air caused by the uneven solar radiation from the sun. The geostrophic wind speed, which is expressed as:

$$U_g = \frac{1}{\rho f} \frac{\delta p}{\delta n} \qquad [1.1]$$

where ρ is the air density, f is the Coriolis force, and $\frac{\delta p}{\delta n}$ is the pressure gradient, occurs at high altitudes above the layer of wind affected by the Earth's surface. However, this equation assumes that the isobars of the pressure gradient are completely straight. Realistically, the pressure gradient is curved around areas of low pressure, adding a centrifugal force that must now be account for. This is commonly expressed as a gradient wind speed:

$$U_{gr} = -\frac{rf}{2} + \sqrt{\left(\frac{rf}{2}\right)^2 + \frac{r}{\rho} \frac{\delta p}{\delta n}} \qquad [1.2]$$

where r is the radius from the center of pressure to the location in question. As you approach the surface of the Earth, the surface roughness of the terrain creates a gradient in the wind flow (reducing the wind speeds at lower altitudes) known as the atmospheric boundary layer.

Typically, wind speeds and pressures used in design codes for residential buildings are obtained from extreme value analysis of weather station data obtained at a height of 10 m. Building codes commonly give design wind speeds for a certain return period at a certain

location at a height of 10 m, corrected to the equivalent values in an open terrain (for example: q_{50} in NBCC). This reference pressure at a height of 10 m can then be expressed as a reference pressure at the roof height by characterizing the wind gradient of the atmospheric boundary layer as a function of altitude (height) using a power law, expressed as:

$$\overline{U(z)} = \overline{U_{10}} \left(\frac{z}{10}\right)^{\alpha} \qquad [1.3]$$

where α is the terrain roughness exponent, U_{10} is the mean wind speed taken from meteorological data at a height of 10 metres, and z is a function of height.

Wind in the atmospheric boundary layer is also turbulent, which can be expressed as a turbulence intensity:

$$I_u(z) = \sigma_u / \overline{U(z)} \qquad [1.4]$$

where σ_u is the standard deviation of the fluctuating component of the wind. These fluctuations are generally due to either the wake of upwind terrain or buildings, or local vortex shedding in regions of separated flow near the edges of a low-rise building, as shown in Figure 1.4.
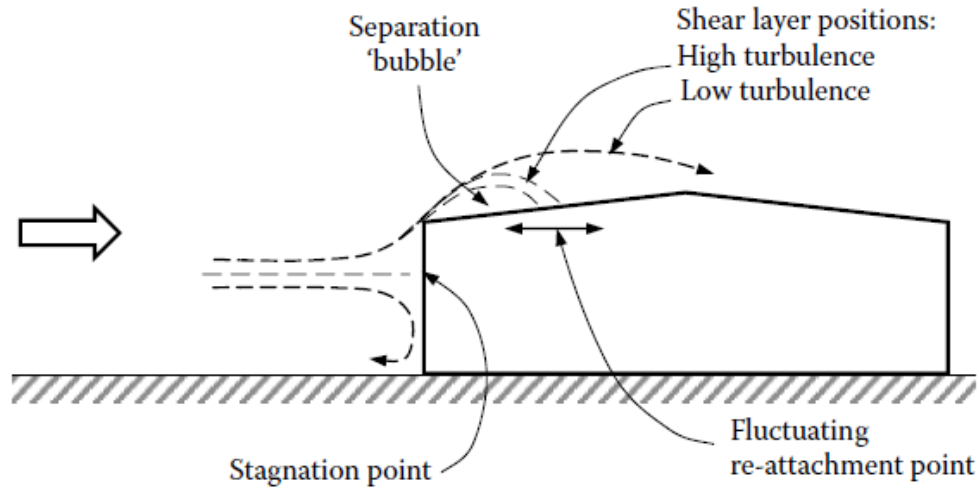
Figure 1.4: Schematic of wind flow around a low-rise building, showing the separation bubble and reattachment point due to flow around the leading edge of the roof (published in Holmes, 2013).

In a typical low-rise building, the flow separates at the leading edge of the roof and reattaches at a further region of the roof. This separation bubble creates significant spatial and temporal variation of pressure across the building surface. These pressures are typically defined by building codes such as ASCE 7-16 as pressure coefficients. This is because external pressures will increase with roof height since the mean wind speed increases with the height of the building. Therefore, pressure coefficients are typically defined relative to the mean wind speed at the roof height to remove the influence of the building height on the magnitudes of the minimum and maximum pressure coefficients. Or:

$$C_{pe} = \frac{p_e - p_0}{\frac{1}{2}\rho U_H^2}$$

[1.5]

where p_e is the external pressure, p_0 is the atmospheric pressure, and U_H is the mean wind speed at the roof height of the building. These pressure coefficients are also highly dependent on the shape of the building. This is because the location of the reattachment point, and the size of the separation bubble change depending on the roof height, and roof slope, leading to different turbulence conditions and therefore, different pressures Figure 1.5 shows how the shape of the building including the roof height and slope can affect the pressure coefficients across the roof of a low-rise building.
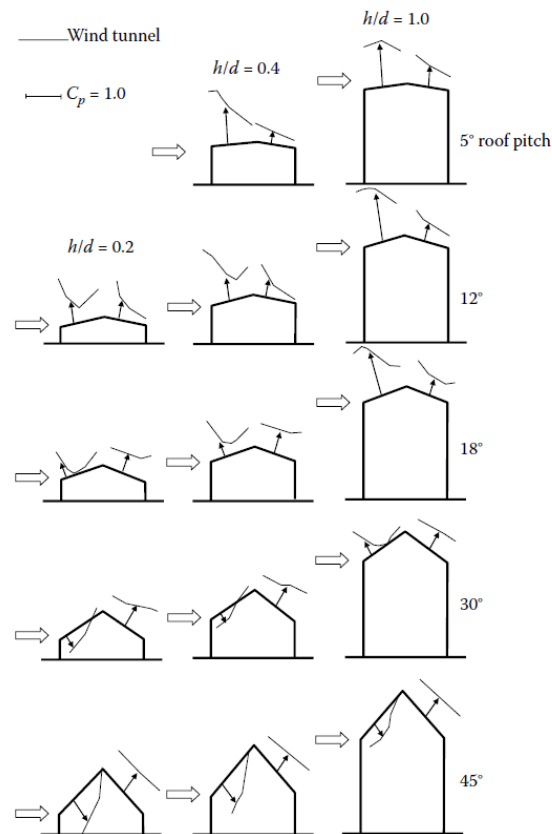
Figure 1.5: Mean pressure distributions on sloped roofs, demonstrating the effect that the building shape has on the turbulence across a low-rise building roof (published in Holmes, 2013).

Because spatial correlations are not perfect, peak load coefficients are reduced significantly by area-averaging. This effective wind area is an important parameter for cladding, as is location on the building.

Wind can also produce internal pressures inside the building, regardless of the size or number of the openings of the building. The internal pressure coefficient is defined in a similar manner to the external pressure coefficient:

$$C_{pi} = \frac{p_i - p_0}{\frac{1}{2}\rho U_H^2} \tag{1.6}$$

where p_i is the internal pressure. Since internal pressures are difficult to determine, they are usually defined using the relationship between the internal pressure and the external pressure, the unsteady Bernoulli equation for losses through a sharp orifice for any opening can be used:

$$p_e = p_i + C_L \frac{\rho U^2}{2} + \rho l_e \frac{dU}{dt} \tag{1.7}$$

where p_e & p_i are the external and internal pressures respectively, C_L is the loss coefficient (which can be determined from the pipe orifice equation to be approximately 2.8), ρ is the density of air, U is the wind speed, dU/dt is the change in wind speed over time. Finally, l_e is a slug of air which moves in or out of the opening. For internal pressures, we usually solve the equations by explicitly considering this slug of air in the Helmholtz resonator model. Rearranging the unsteady Bernoulli equation, yields:

$$p_e - p_i = C_L \rho \frac{\dot{x}|\dot{x}|}{2} + \rho l_e \ddot{x} \qquad [1.8]$$

The position of the mass of air, x, is related to the internal pressure because it controls the density change. Using the principles of adiabatic flow and conservation of mass, one obtains:

$$\dot{x} = \frac{V_0}{A_0 n p_0} \dot{p} \qquad [1.9]$$

$$\ddot{x} = \frac{V_0}{A_0 n p_0} \ddot{p} \qquad [1.10]$$

Finally, using the equations for internal and external pressure coefficients (referencing them to a neutral atmospheric pressure), and combining the two previous equations, one obtains:

$$\frac{\rho l_e V_0}{n p_0 A_0} \ddot{C p_i} + \left(\frac{\rho l_e V_0}{2 n p_0 A_0}\right)^2 C_L \dot{C p_i} |\dot{C p_i}| + C p_i = C p_e \qquad [1.11]$$

When there are multiple openings, one can obtain an equation like this for each opening. This is an engineering model, which involves empirical coefficients. The true flow is given by the Navier-Stokes equations, so while this model can accurately estimate the internal pressures, there are also situations where it will break down. However, it does demonstrate a few important concepts. Most importantly, if the external pressure is static (i.e., not varying), the internal pressure will equal the external pressure. This shows that the internal pressure is dependant only on the temporal variations of the external pressures.

Since this is complicated for design purposes, building codes generally account for internal pressures by providing a static internal pressure depending on the number and size of openings in the building. The assumption made here is that the volume of the internal area of the building is sufficiently large that the internal pressure become spatially and temporally uniform. This allows for the net load on the structural elements of low-rise buildings to be calculated:

$$C_{pn} = C_{pe} - C_{pi} \qquad\qquad [1.12]$$

However, as shown in Figure 1.3, when trying to define the net loads on air-permeable multilayer systems, not only is there an external pressure and an internal pressure, but there is also a cavity pressure. This cavity pressure is similar to the internal pressure, but since the volume of the cavity is much smaller, the pressure inside ceases to be uniform, especially with air-permeable multilayer cladding, where there can be multiple openings with lots of flow through the cavity volume.

1.4   Pressure Equalization

1.4.1   Definition

There is little design guidance in building codes for determining the wind loads on air-permeable multilayer cladding systems, for example, ASCE 7-16 (2017), section C30.1.5. indicates that:

"[...] If the designer desires to determine the pressure differential across a specific cladding element in combination with other elements comprising a specific building envelope assembly, appropriate pressure measurements should be made on the applicable building envelope assembly or reference should be made to recognized literature [...]"

In other words, this tells the designer that they need to go and find the answer. The lack of developed design guidelines for these products is due to the complexity of the interaction of external wind loads with the flows in and through air-permeable multilayer cladding, This interaction is sometimes called pressure equalization, which is the mechanism whereby the pressures on the external building surfaces are partially transmitted through air-permeable outer layers to interior layers (Kumar, 2000). Due to the air-permeability of the cladding, the external wind loads can transfer into the cavity in between the cladding, and the outer layer of sheathing.

To try and account for pressure equalization, some manufacturing standards have adopted the use of a "Pressure Equalization Factor" (PEF). There are different ways to empirically define PEF (which are explored in Chapter 4). However, the basic definition of PEF is the proportion of the external load that is acting on the cladding. This concept is different than that of internal pressurization as the adjacency of external and internal pressures are much more critical. Understanding pressure equalization is crucial to understanding how loading is transferred through multi-layer systems, and ultimately, to mitigating failures. Although building codes do little to address this reduction in cladding, manufacturing standards attempt to set guidelines for these products. As an example, the American Society for Testing & Materials (ASTM) provides manufacturing and testing standards used for

guidelines of different material properties of products and materials typically used in the construction industry. Examples of standardized tests that are used to evaluate product performance under wind loads include ASTM D5206 (2013) for vinyl siding, ASTM E1592 (2012) for metal roofing, and ASTM E1300 (2012) for glazing and glass. Most of these standardized tests make use of a sealed airbox system, where the pressure required to fail the particular product is obtained. Many of these standardized tests use uniform, static pressures or slowly increasing pressures, such as those listed above. For components that have low-cycle fatigue as a failure mechanism, sinusoidally-varying pressures at various frequencies and amplitudes are applied (Henderson et al., 2013). In all cases, the pressures applied by these standard tests are uniform over the component. This, of course, provides applied loads that are significantly different than real wind loads, but which are relatively simple and inexpensive to apply (Kopp et al., 2012). In the case where pressure equalization is eliminated from the test, related standards then provide PEF values to interpret the test results. For example, in ASTM D5206, pressure equalization is eliminated by placing an air-tight barrier between the siding layer and internal sheathing layer or insulating layer. Uniform, static pressures are then applied via an airbox in order to determine the capacity of the siding. This yields the net pressure at the limit state (assuming that the failure mechanism and capacity are not substantially altered by the approach). The level of pressure equalization in the real system is then assumed via ASTM D3679 (2013) where a reduction factor of 64% (i.e., the failure load is multiplied by a value of 0.36) is given "due to the effects of pressure equalization". This factor was based on the 2002 study done by Architectural Testing Inc. (ATI) for the Vinyl Siding Institute (ATI, 2002). In that study, wall samples were subjected to a series random, uniform gust loads at a low,

medium, or high-pressure level. Results from this study showed that pressure equalization factors from these tests ranged from 0.03 to 0.18 (i.e., pressure equalization reduced the net loads on the siding by 82 – 97%). The highest result was then doubled to create the design pressure equalization factor of 0.36. However, this is problematic as well, since the use of uniform wind loads creates near perfect pressure equalization, resulting in the low PEF values shown in this study.

1.4.2   Aerodynamic Mechanisms

Generally, there are two different types of mechanisms that are assumed to control the net wind loads on air-permeable multilayer cladding. The first type of model develops aerodynamic or area-averaged pressure coefficients related to the local flow around the cladding element assuming that the wind pressures due to the larger building itself fully equalize across the layers of the cladding. Thus, this mechanism is based on the local flow near the building / cladding surface. One example of this is wind loads on shingles, which assumes that the uplift on the tabs (which leads to the failure of the asphalt adhesion) is caused by flow separating from the tabs (Peterka et al., 1997). Roof-mounted solar panels with fairly high tilt angles can also be subjected to this type of wind loading with local flows governing (Kopp et al., 2012). The second type of mechanism considers the pressure differences across the outer and inner surfaces of the cladding element, with the outer, or external, pressure controlled by the large-scale flow around the building and the location of the element on the surface. In contrast, the inner, or cavity pressure, is controlled by the openings in the cladding layer, the cavity geometry, and the flow through these. This

mechanism is called pressure equalization. Rain screen walls rely on pressure equalization (Kumar, 2000), although it has also been shown that solar panels parallel (or close to parallel) to a roof surface (Stenabaugh et al., 2015), roof pavers (Bienkiewicz & Sun, 1992; 1997), and vinyl siding (Morrison & Cope, 2015) also rely on this mechanism.

The distinction between these two mechanisms is not completely clear. For example, Moravej et al. (2016) have shown that flow emerging through gaps between roof pavers, from the cavity below, alters the local flow around individual pavers and, ultimately, the net loads. Peterka et al. (1997) neglect the pressure below the shingle, while pressure equalization models neglect the effects of the local gap flows on the external pressures (e.g., Sun & Bienkiewicz, 1993; Oh et al., 2014). In addition, the flow mechanism of Peterka et al. (1997) neglects building aerodynamic effects such as the magnitude of pressures above the roof. This effectively assumes that multilayer systems such as shingles are perfectly pressure equalizing with the resultant net loading due only to the local flow and load effects caused by the step change at the tabs. The implication of this is that the locations of worst loading are associated with the highest wind speeds close to the roof surface and not where the external surface pressures have the largest magnitude.

Due to its reliance on the geometry of the cladding and historical developments which considered each type of cladding system separately, PEF values (and by consequence, net wind loads) have not been standardized. However, several methods have been developed to measure PEF, which are detailed in the following sections.

1.4.3   Field Measurements

Field measurements are not typically used to determine peak net loads on air-permeable multilayer cladding for design. Rather, these studies tend to use differential pressure measurements through cladding to calculate ventilation for moisture and frost accumulation studies (e.g., Uvslokk, 1996; Straube, 1999). These types of studies cannot be used for design wind loads. Since they are not concerned with capturing high wind conditions. Gerhardt & Jansen (1994) instrumented cladding panels on an office building to compare pressure equalization on regular panels vs. panels which had the cavities sealed on the vertical edges. This study showed that the modified panels increased pressure equalization (i.e., reduced wind loads) due to compartmentalization. Geurts et al. (2013) also instrumented solar panels in the field to provide a first estimate of the wind loading on solar panels.

1.4.4   Model-Scale Wind Tunnel Measurements

Model-scale wind tunnel measurements have been a critical tool to developing the knowledge about pressure equalization, notably in the area of loose-laid roof pavers and solar panels. However, cladding with small gap openings (e.g., vinyl siding, shingles, discontinuous metal roofing) cannot be tested at model-scale due to errors created by scaling. Proper scaling is necessary to capture flow behavior over entire structures (Gerhardt and Jansen, 1994; Oh & Kopp, 2014). Applying these scales, which are typically 1/100 to 1/500, means cavity heights cannot be manufactured accurately (for example, a

cavity height of 1 mm at a 1/100 scale is impossible to manufacture). The gaps and openings in the cladding have a similar scaling problem and are not manufacturable. In addition, scaling down cavities behind the cladding can result in Reynolds number effects where cavity air flow is forcibly laminar, which may alter the overall net load on the cladding (Cheng & Melbourne, 1986; Gerhardt & Jansen, 1994).

Gerhardt & Jansen (1994) highlighted these issues by conducting wind tunnel tests on a scaled building with cladding. They showed that the full-scale field measurements did not match the wind tunnel testing and commented it was likely due to sensitivity in gap flow resistance between the scale model and the full-scale measurements. Cheng & Melbourne (1986) examined the size of the gaps of the cladding and cavity volume, and the role they play in the net load on air-permeable multilayer cladding systems. They showed that increasing the size of the gaps in cladding or increasing viscous effects in the cavity can decrease the net pressure. Kala et al. (2008) conducted a similar wind tunnel study on rainscreen walls, in order to examine the parameters affecting pressure equalization. Van Bentum et al. (2012) also conducted wind tunnel tests on a 600 mm cube, with cladding of varying depths that were open at the edges only. They showed that the smallest cavity depth resulted in the highest net pressure. However, this is likely inaccurate as mentioned by the authors due to the openings being at corners only, as well as the scaling issues mentioned in the previous paragraph.

One of the first studies to examine pavers and how the pressure equalizes across the cladding was Kind & Wardlaw (1982) who conducted a study to examine the failure (lifting / overturning) of roof pavers. They showed that the net wind loads on the pavers were much lower than the external pressure values on an air-impermeable roof. These lower loads

reduced the chance of failure of the pavers. This study was furthered by Kind et al. (1988)
to predict the wind speeds that caused failures of the roof pavers. However, Okada & Okabe
(1991) showed that the cavity height can decrease the failure load of the pavers if the cavity
height is too high.

Bienkiewicz & Sun (1992, 1997) also conducted wind tunnel tests on a flat roof with roof
pavers, comparing the net pressures on the pavers when there was no cavity, compared to
a small cavity. This study showed that increasing the cavity height resulted in a more
uniform cavity pressure distribution, which reduced the pressure equalization and
increased the net loads. It also showed that reducing the spacing between the pavers had a
similar effect. Bienkiewicz & Endo (2009) also conducted a similar study to try and
account for the effect of the gap between pavers on the net load on the pavers. They showed
that the overall net loads on the pavers is dependent on the permeability of the outer layers
(i.e., permeability increases when the gaps in the pavers increases).

The previously mentioned paver studies were all conducted at a 1:25 scale, but Mooneghi
et al. (2014) conducted a 1:2 scale model of roof pavers using the large fans at the Wall of
Wind facility on a small building. This study tested different ratios of the gaps between the
pavers over the height of the cavity (G/H). The results show that increasing the G/H ratio
resulted in lower mean and peak net loads on the pavers, as well as also showing that the
cavity pressure is uniform at low G/H ratios.

Pressure equalization is also critical for developing design wind loads for solar panels. As
solar panels have become increasingly popular to install on roofs of buildings, there has
been a lot of research to determine the wind loading mechanisms on these panels. Ginger

et al. (2011) examined the effect that roof angle has on the net loads of solar panels when they are parallel to the roof. The results showed that the cavity depth did not play a role in the net loads on the solar panels. However, the solar panel was assumed to be one large array with no gaps in a large panel. Similar studies were also conducted by Stenabaugh et al. (2010) and Aly & Bitsuamlak (2014), which determined that with no gaps between the panels, the net loads on the panels were like the external loads on a bare roof surface. Kopp et al. (2012, 2013) examine array geometry and their effect on the net load of the panels. They showed that the mechanism that governed the net load depended on the tilt angle of the panels. Panels were governed by pressure equalization when they were either parallel to the roof, or with a low tilt. The studies also showed that the spacing of the row and the height above the roof surface had minimal impact for the geometries examined.

Stenabaugh et al. (2015) examined the role that the G/H ratio has on the net loads on solar panels. It was shown that a high G/H ratio lowered the net loading on solar panels, and consequently the PEF. This shows similarities with roof pavers, and how their net loads are affected by the G/H ratio. This study was the basis for codifying a pressure equalization factor in ASCE 7-16 (2017). This is the first instance in a building code where any sort of consideration for pressure equalization is considered on the net loading of an air-permeable system. However, these provisions are only valid for solar panel arrays, whereas other air-permeable multilayer cladding still must be designed as if pressure equalization does not occur, as discussed in section 1.4.1.

The main findings of these model scale studies are that the geometric ratio of the gap size to the cavity height (G/H) is an important parameter in determining the pressure equalization on air-permeable multilayer system. Or, in other words, how the ratio of the

resistance of the orifice flow to the cavity flow affects pressure equalization. For example, when the cavity flow resistance is low compared to the orifice flow resistance, the pressure equalization is high, leading to a negative impact on the net loads on cladding.

1.4.5   Full-Scale Measurements

Similar wind load testing methods have been conducted before at the Insurance Research Lab for Better Homes (IRLBH); most notably, in the study done by Gavanski & Kopp (2011) where vinyl siding was tested in a similar airbox chamber system as mentioned in the ASTM D5206 (2013) standard. It was determined from that study that pressure equalization occurs across the air-permeable wall layers and substantially increases the maximum critical wind speed of the wall system. More specifically, vinyl siding equalizes almost perfectly and sees little to no net load when a uniform pressure is applied. Also noted were the limitations of this airbox system:

> *"[…] First, for very flexible cladding elements (e.g., vinyl siding), the requirement of mechanical attachment means that, for failure tests, only uniform pressures can be applied by using a single air- box which surrounds a relatively large test sample (and not contacting the surface of the sample). So, while time varying loads can be used, any spatial effects cannot be identified simultaneously with failure mechanisms. […]"*

This study by Gavanski & Kopp (2011) also obtained similar PEF values from static, uniform airbox tests conducted by Architectural Testing Inc. (ATI, 2002). Recently, using full-scale wind tunnel tests from the Insurance Institute for Business and Home Safety (IBHS) Research Center (Cope et al., 2012; Cope et al., 2014, Morrison and Cope, 2015), a PEF of 0.8 was obtained, indicating load coefficients that are more than double those of ASTM D3679 (2013), all else being equal. Clearly, there is a disconnect between standardized testing, and recent full-scale testing methods, demonstrating the need to develop appropriate methodologies for assessing net pressures for air-permeable, multi-layer assembles. More recently, Moravej et al. (2016) also measured differential pressures across vinyl siding using the Wall of Wind facility at Florida International University. Net pressures were calculated by comparing the peak external pressure along with cavity pressure coefficients, which led to low net pressure coefficients due to the values not being coincident with each other. The instantaneous PEF values were also calculated over a tributary area. These values matched with the study done by Cope et al. (2012), demonstrating that the current standard for some air-permeable multilayer cladding is underestimating design wind loads.

Full-scale measurements have also been performed on rainscreen walls (Stathopoulos, 1981). Similar testing done by Kumar et al. (2003) has shown that there are discrepancies between the codes for loads on rainscreen walls, and the results obtained in these studies.

1.4.6   Analytical / Computational Models

Killip & Cheetham (1984), Fazio & Kontopidis (1988), Baskaran & Brown (1992), and Xie et al. (1992) were some of the first studies to attempt developing an analytical model for pressure equalization by using the discharge equation of flow through small openings, while assuming the flow was incompressible. Van Schijndel & Schols (1988) and Burgess (1995) took this a step further by incorporating the ideal gas law into these equations.

The models were then further developed by Inculet & Davenport (1994), Choi & Wang (1998) and Kumar & Van Schjindel (1999) by introducing unsteadiness through the Helmholtz resonator model developed by Holmes (1979) and Vickery (1986). Although these models match the experimental data, they could only consider a spatially uniform external pressure with a single opening. The models for cavity pressures were also improved by Amano et al. (1988), Trung et al. (2010), and Lou et al. (2012) by including the discharge model spatially varying cavity pressures.

Although the discharge equation has been widely used to model flow through an opening by multiple studies (Sharma & Richards, 1997; Oh et al., 2007; Kopp et al., 2008; Ginger et al., 2010), it does not consider the viscous effects in the cavity flow. This is critical because cavities on air-permeable multilayer systems tend to be thin and long, which would amplify the role that viscous effects have on the cavity flow. Sun & Bienkiewicz (1993) attempted to incorporate viscous effects into the pressure distributions in the cavity by using Darcy's Law. However, the model is only useful for the mean flow (or flows with low turbulence).

Kumar et al. (2000) noted that continuous cavities are not always efficient, and that compartmentalization improves pressure equalization. If the cavity is divided into compartments, it could reduce the external pressure gradients, and the flow between the adjacent cavities would be minimized. This would improve pressure equalization by reducing the flow in the cavity and, therefore, reducing the overall net load on the cladding. Furthermore, a study from Morrison & Hershfield (1990) suggested that compartmentalization should be required at the corners of buildings using a vinyl siding clad wood-framed wall. Doing this can reduce the pressure drop across the inner surface as well as the volume of air required for equalization, reducing the response time of cavity pressures.

Figure 1.6 shows a model for a cavity with two openings developed by Oh & Kopp (2014). Assuming that the flow through the gap is like an orifice flow, the flow in the cavity is unsteady Couette flow, and the cavity pressures are formed by this series of pressure drops, the formula for flow between parallel plates can be used to form the three following equations:
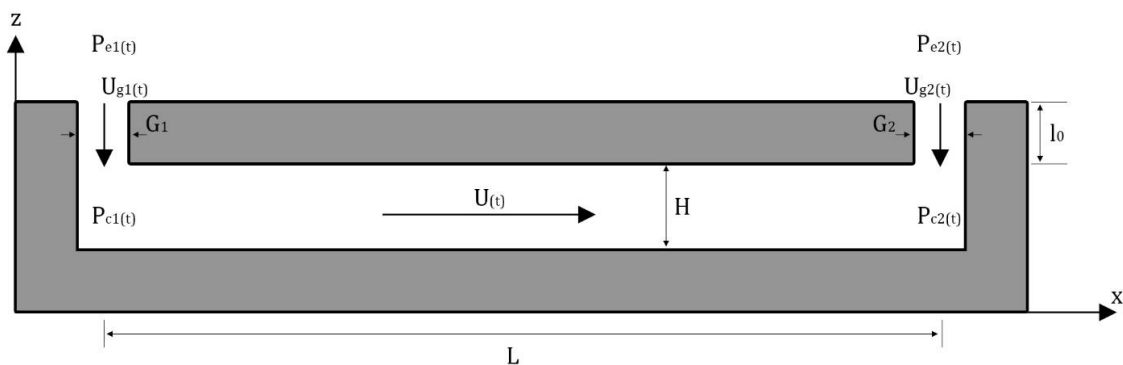
Figure 1.6: Pressure model of a flow in a double-layer system with two openings.

$$\rho l_{e1} \dot{U}_{g1}(t) + C_{L1} \frac{\rho}{2} U_{g1}(t) |U_{g1}(t)| + \frac{12\mu l_{01}}{G_1^2} U_{g1}(t) = p_{e1}(t) - p_{c1}(t) \qquad [1.13]$$

$$\rho L \dot{U}(t) + \frac{12\mu L}{H^2} U(t) = p_{c1}(t) - p_{c2}(t) \qquad [1.14]$$

$$\rho l_{e2} \dot{U}_{g2}(t) + C_{L2} \frac{\rho}{2} U_{g2}(t) |U_{g2}(t)| + \frac{12\mu l_{02}}{G_2^2} U_{g2}(t) = p_{e2}(t) - p_{c2}(t) \qquad [1.15]$$

1.5　Neutral Pressure Line

The concept of using neutral pressure lines to determine the internal pressures acting on a building was first introduced by Emswiler (1926) and built upon by Tamura & Wilson (1966). The neutral pressure line is the location where there is no pressure difference across the building envelope due to the external pressure and the cavity pressure being equal. On a tall building, this neutral pressure line is created by the stack effect of the building. The stack effect is the upward flow of heated gas either through the chimney, elevator shaft, or other large openings on the building. Figure 1.7 shows the mean pressure distributions on a tall building due to the stack effect.

In cold climates, the outdoor air is denser than the indoor air, shown in equation 1.14 as a derivation of the ideal gas law:

$$\rho = \frac{p_0}{R_a T} \qquad [1.16]$$

where p_0 is the atmospheric pressure, R_a is the gas constant, and T is the air temperature. This leads to the dense cold air flowing into the building, which warms the air and lowers the density. This warm air travels up the stack and exits the building at the top due to the high external suctions from the outdoor wind. The external pressures outdoors change more rapidly with height, leading to pressure differences across the building enclosure, creating a neutral pressure line. Assuming the external pressure distribution is linear along the height of the building, an expression for the net pressure at a distance h from the neutral pressure line is given as:

$$p_n = gh(\rho_{outside} - \rho_{inside}) \tag{1.17}$$

Equation 1.14, and equation 1.15 can be combined to show how the net pressure changes with respect to the neutral pressure line, and temperature difference:

$$p_n = \frac{ghp_a}{R_a}\left(\frac{1}{T_{outside}} - \frac{1}{T_{inside}}\right) \tag{1.18}$$
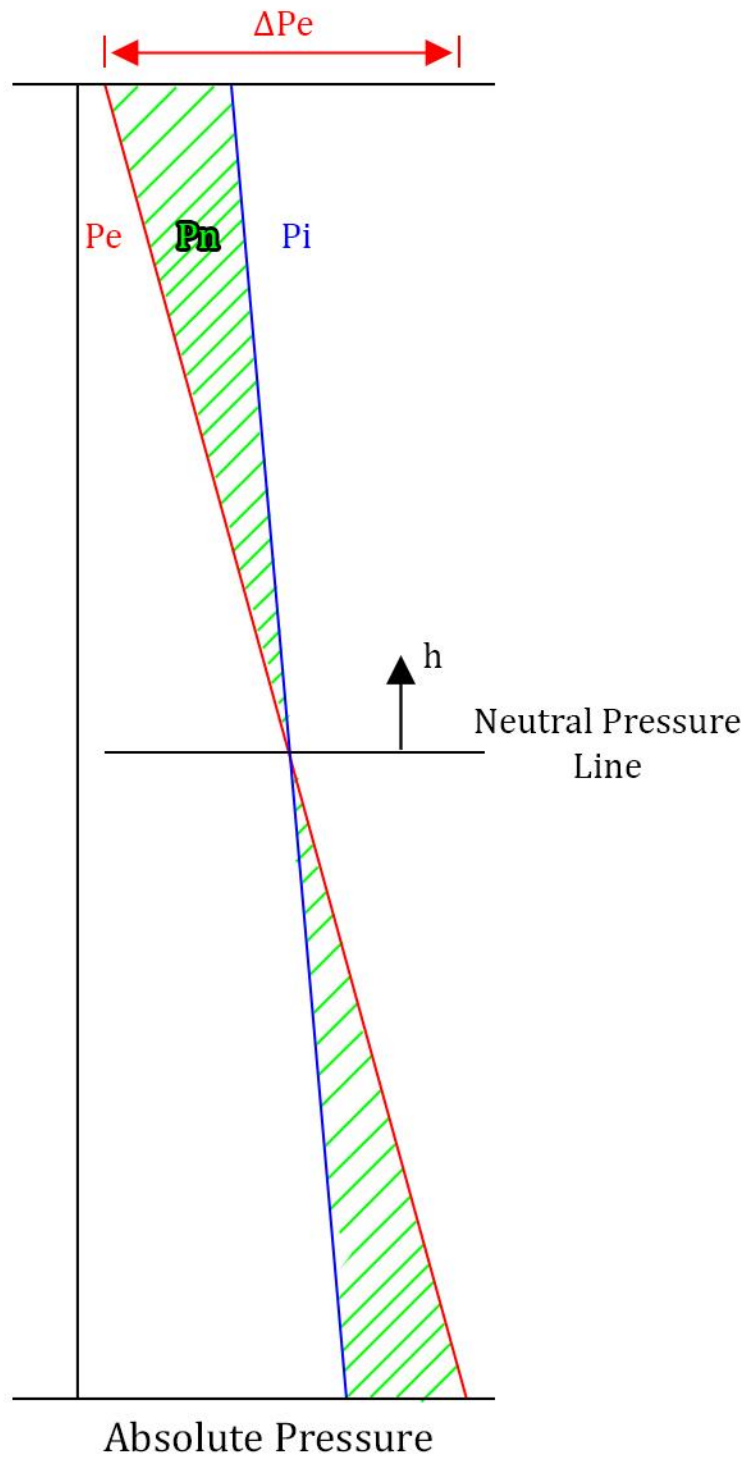
Figure 1.7: Mean pressure distributions on the external surface and internal volume of a tall building, demonstrating stack effect.

Along with developing an analytical model for cavity flow, Oh & Kopp (2014) also examined a similar neutral pressure line concept for cavity pressures in air-permeable multilayer cladding systems. Consider a panel of a double-layered system with two openings with flow entering and leaving the cavity based on the external pressure distribution, similar to Figure 1.6. As mentioned earlier, cavity pressures are often uniform, which occurs when the losses through the gaps are significantly larger than the friction losses of the flow through the cavity volume. Typical stack effect models have a slight variation in the internal pressures (as shown in Figure 1.7). However, since a typical cavity is much smaller than a tall building, the assumption of a mostly uniform cavity pressure will hold for this model. As well, temperature effects are ignored due to the fact that cavity temperatures will not be any different than external temperatures. A schematic demonstrating the concept of a neutral pressure line on a double layered system is shown on Figure 1.8:
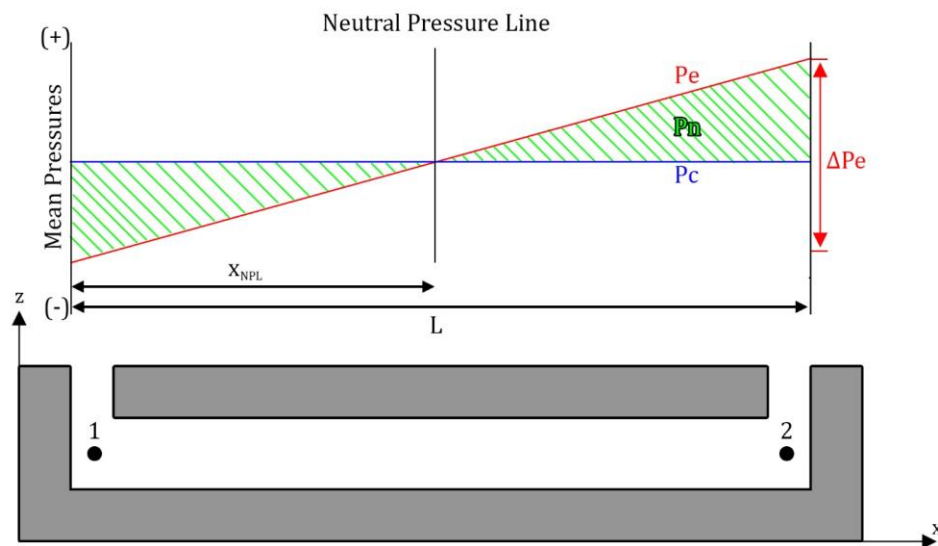
Figure 1.8: Ideal mean pressure distributions on the external surface and cavity of a panel, demonstrating the effect of a neutral pressure line.

Sreevedi (2017) took the concept of a neutral pressure line and combined it with Oh & Kopp (2014) to introduce the idea of a lumped leakage approach. In this model, the losses due to flow through the openings are lumped across areas defined by the neutral pressure line, by using Bernoulli's obstruction theory to create an effective loss coefficient:

$$K_L = \frac{1 - \left(\frac{A_0}{A}\right)^2}{C_d^2} \qquad [1.19]$$

where A_0/A refers to the ratio of the area of openings to the area of the region, and C_d is the discharge coefficient through the lumped openings. This can be applied to the Oh & Kopp (2014) model for a lumped leakage approach to pressure equalization.

$$\rho l_{e1} \dot{U}_{g1}(t) + K_{L1} \frac{\rho}{2} U_{g1}(t) \left| U_{g1}(t) \right| + \frac{12 \mu l_{01}}{G_1^2} U_{g1}(t) = p_{AE1}(t) - p_c(t) \qquad [1.20]$$

where p_{AE1} is the area-averaged external pressure for that region. This model assumes that the cavity pressure is uniform, which holds for small G/H ratios, typical for air-permeable multilayer systems.

1.6 Objectives

In summary, although the concept of pressure equalization has been well documented in air-permeable multilayer cladding systems, there has been no attempt to unify the many different studies on different systems, or to determine which factors govern the cavity pressure (and consequently, the PEF) of the system. This has led to an inadequacy in design standards for these systems. Therefore, the overall objective of this thesis is to provide

design recommendations for a unified approach to the pressure equalization factor for use in design standards such as ASCE 7. Since it has been shown that model-scale experiments are not appropriate for this material type, full-scale experiments will be required. The first step is to confirm that current airbox testing is inadequate by using the Pressure Loading Actuators (PLAs) at the Insurance Research Lab for Better Homes (IRLBH) to create spatially varying loads using a multichambered airbox system and comparing it to a single chamber airbox system. Next, the main aerodynamics of cavity flow and how that affects cavity pressure in a realistic air-permeable multilayer system should be examined to determine the factors that govern PEF. To do this, the full-scale wind tunnel at the Insurance Institute for Business & Home Safety (IBHS) will be used. Finally, comparing these results to other studies done on other air-permeable multilayer cladding, along with the knowledge obtained of what factors govern PEF will be used to create a unified approach to the pressure equalization factor for all systems.

1.7 Layout of Thesis

Chapter 2 examines the current standard airbox test for vinyl siding and replicates the IBHS study on the same study to show the importance of spatial variations in standardized testing. Chapter 3 discusses the aerodynamics of the cavity flow of air-permeable multilayer cladding, and how that affects pressure equalization. Finally, Chapter 4 synthesizes the data from multiple studies on air-permeable multilayer cladding to create a unified approach to the pressure equalization factor for all of these systems.

2 A Multichambered, Pressure-Based Test Method to Determine Wind Loads on Air-Permeable Multilayer Cladding Systems

2.1 Objectives

As shown in Chapter 1, current airbox testing for the standardized testing of wind load resistance relies on uniform applied pressures from a single chamber airbox system to apply loads on the cladding. However, since the cavity pressures should perfectly equalize across a system with uniform pressure, this method may be leading to inaccuracies in design methods of air-permeable multilayer products. The objective of this study is to apply spatially varying loads using a multichambered airbox system to demonstrate the inaccuracies of the current testing methods, as well as the need for updated pressure equalization factors, since many pressure equalization factors in manufacturing standards were created using this method.

2.2 The Multichambered, Pressure Loading Actuator Method

2.2.1 Background

One of the first systems to replicate realistic fluctuating pressures on a scale suitable for representative sections of the building envelope is the Building Research Establishment's real time wind uniform load follower (BRERWULF; Cook et al. 1988). While this test method was a significant advance, the main disadvantage of the BRERWULF system is that it could not accommodate air flow through the specimen, which is common in many standard building materials. As such, a multi-chamber BRERWULF system for testing air-

permeable cladding would not function well because of the necessity to allow airflow between chambers.

A loading system capable of applying spatially and temporally varying loads on standing seam metal roof cladding was developed at Mississippi State University (Sinno et al. 2003; Surry et al. 2007). The test rig used large capacity electromagnets to apply an array of quickly varying uplift loads on top of a uniform positive pressure applied from an air-box underneath the cladding. Importantly, the MSU system brings the application of realistic (temporally and spatially varying) wind pressures to the test specimen. The disadvantages of this technique are that it only works with metal cladding elements and there is a significant amount of tuning to the system required before a specific loading trace could be applied to a specimen.

Kopp et al. (2010, 2012) presented a loading system based on "pressure loading actuators" (PLAs), which overcame the limitations of the BRERWULF and MSU loading systems. The PLA system uses multiple pressure chambers to capture the spatial variations of the wind loads while each individual PLA is able to capture pressure fluctuations up to about 10 Hz with peak pressures of up to about 23 kPa in pressure and -20 kPa in suction (Kopp et al. 2010). Thus, very large loads, at the limit states of wood-frame houses, could be applied (Morrison et al., 2012; Henderson et al. 2013) to buildings with significant leakage through the building envelope via a system of flexible, independent airboxes.

2.2.2   Pressure Chambers

All pressure-based loading systems require a chamber in which to apply the pressures. Usually these are nominally airtight and of fixed volume, i.e., they have solid side walls. Thus, the PLAs also require pressure chambers in order to apply the load to a building surface. However, for applying loads to the surface of a house, Morrison et al. (2012) developed a system of multiple, independent, flexible airbags with rigid supporting frames. These pressure chambers consisted of a rigid modular lid, which incorporated a molded inlet duct with air-filter, the surface of the building (test specimen), which forms one surface of the chamber, and a flexible vinyl skirt that encloses the space between the lid and building surface, which forms the walls of the chamber. This system was required to be at least nominally airtight so that the pressure traces could be controlled reliably with leakage coming only through the building surface (such as, e.g., bricks or cracks). The lids of the pressure chambers were connected to a rigid reaction frame. The skirt or membrane was required to be flexible since the building or component could deflect (on the order of 15 cm or more). Each pressure chamber was independent of the others because they were separated by approximately 2 inches (5 cm) with no physical communication between them.

This pressure-chamber system was adequate for testing the structural response of buildings, but there is a significant issue that needs to be addressed for cladding tests. The surface areas outside of the chambers, but part of the test sample, are problematic for multi-layer cladding tests where the intent is to determine the net pressures across layers of the cladding. The reason for this issue is that the cavity pressures depend significantly on the

external pressure gradients, as discussed above. Thus, these non-pressurized areas need to be eliminated (or only located at non-porous areas of the cladding surface) because they artificially alter the pressure gradients. For vinyl siding, where there may be continuous leakage, the only solution is to eliminate the unloaded areas on the external surface of the cladding by having common "skirts" for adjacent pressure chambers. This poses a challenge for the PLA control system because there are two forms of communication between adjacent chambers: (i) net flows through the interior volume of the cavity between layers from one chamber to another, and (ii) the changes in chamber volume due to the movement of the skirt because of the time-varying differences in pressure between adjacent chambers. Details of the implemented pressure chamber solution for testing vinyl siding are provided in Section 2.4. To understand the control solution, the operation of the PLAs is described next.

2.2.3   Flow-Reversing Valves

Conceptually, the control of the pressure in an airbox can be done in two different ways. One can vary the supply pressure into the airbox by varying the fan speed and direction using a variable speed drive (VSD). Alternatively, one can use a flow-reversing valve to control the pressure inside a pressure chamber. The first option provides the simplest and cheapest solution; however, it is not technically feasible to change the fan speed fast enough to be able to meet both the pressure magnitudes and frequencies required to simulate realistic wind loads on cladding elements. As such, the conceptual design consists of a fan or blower to produce the pressures, a valve system to regulate the applied pressures

and a feedback control system in order to monitor the applied pressure and adjust the valve system accordingly.

Different valve configurations could be employed to quickly reverse airflow to and from a fan operating at constant speed. The minimum number of ports required would be four, with one into the low pressure side of the fan, one out of the high pressure side of the fan, one connected to atmosphere, and one to the airbox. However, for the current, as well as for the previous BRERWULF design, a 5-port design was employed, with the additional port also connected to atmosphere. The advantage of a 5-port design is that it avoids a closed loop between the fan inlet and outlet which would result in heat building up in the system. It should be noted that individual valves could be used on the different ports to change the flow direction, but to minimize the number of components, moving parts, and control complexity, a rotating disc within the valve was chosen. This has the advantage of one moving part, which is on the axis of rotation of a servomotor.

Figure 2.1 shows a schematic of a 5-port valve and rotating disk concept along with Figure 2.2 which shows a flow schematic demonstrating operation. The valve is made in two halves (i.e., two castings), one with two ports and the other with three, with a slotted disk between them. Figure 2.3 depicts an assembly drawing of all the parts making up the valve. The two ports in the two-port half of the valve are connected to the fan with "i" (in Figure 2.1) representing the connection to the inlet (low-pressure side) of the fan and "o" representing the connection to the outlet (high-pressure side) of the fan. The direction of flow through these ports is also shown in Figure 2.1. For the three-port half of the valve, there is inflow from the atmosphere into port "a" and outflow to the atmosphere from port "c". Port "b" is connected to the pressure chamber and flow can be either into or out of this

chamber, depending on the position of the slotted disk. It is for this reason that this device is called a flow-reversing valve.

Figure 2.2 shows the three limiting states of the valve: (i) neutral, with no flow into or out of the pressure chamber, (i) full flow out of the pressure chamber, and (iii) full flow into the pressure chamber. The position of the slotted disk, which is controlled by a servomotor, determines which state occurs. For example, when the disk is in the position such that port "a" is entirely blocked, there is no inflow from the atmosphere and the flow is from the pressure chamber through port "b" into the fan inlet, through the fan, and out to atmosphere. This state leads to lower than atmospheric pressure (i.e., suction) in the pressure chamber. This is depicted in the middle schematic of Figure 2.2 while the other two schematics in Figure 2.2 depict the other two limit states discussed above.

As noted above, the slotted disk is positioned by a servomotor, which can move the slotted disk to any angle. Depending on the disk angle, a range of positive and negative pressures can be achieved, which is determined by the fan characteristics, flow losses (i.e., pressure drops) in the ducts, valve and other flow elements, and leakage into (or out of) the pressure chamber. Figure 2.3 presents the final assembly of the different valve components, along with the symmetric slotted disk design. The final shape of the valve was determined by using computational fluid dynamics to minimize the losses, improving the overall performance of the system (i.e., reducing power requirements to achieve particular pressures at particular leakage flow rates). The next section discusses the development of the valve in detail, and how it controls the pressure under different leakage conditions.
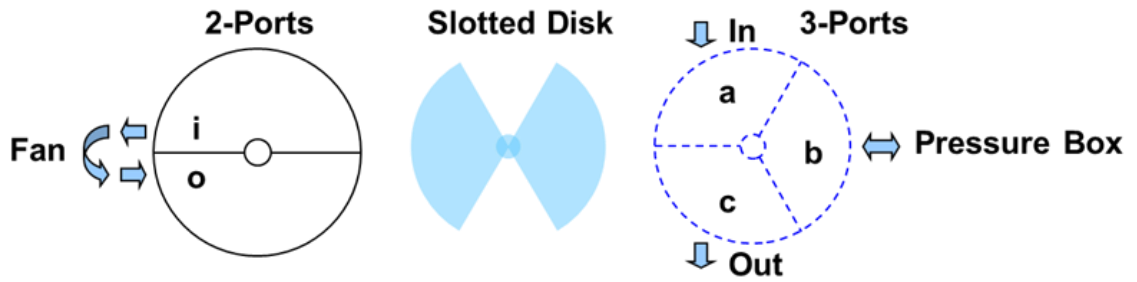
Figure 2.1: A schematic drawing of the five-port valve concept.
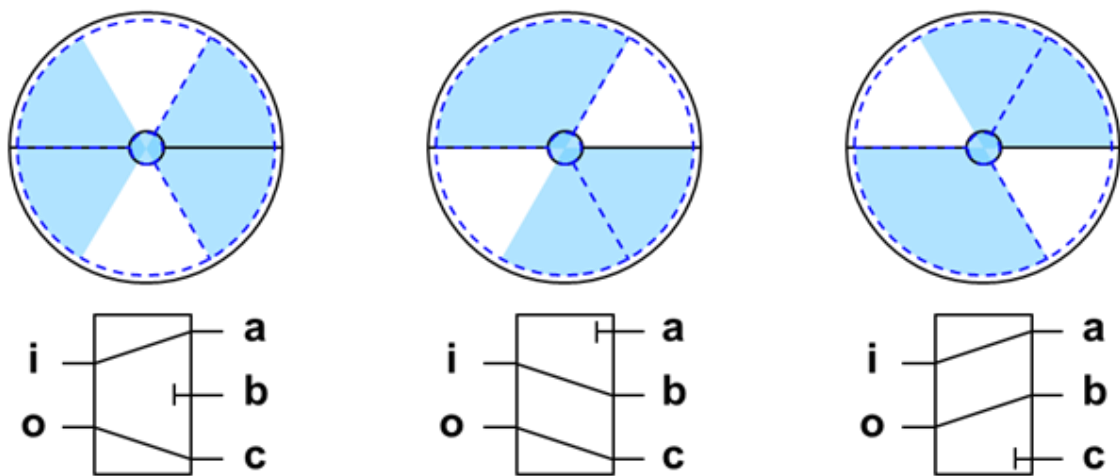
Figure 2.2: An operational flow diagram showing the three limiting states of the valve.
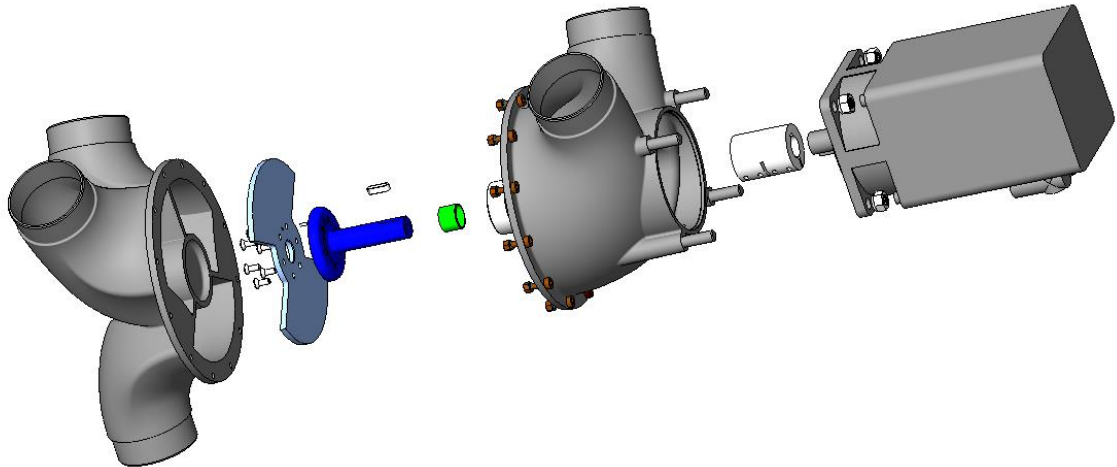
Figure 2.3: An assembly drawing showing an exploded view of the final valve design and symmetric disk.

2.2.4   Performance & Control Under Variable Leakage Flows

One of the critical aspects of simplifying the computer control system was the linearization of the valve, i.e., ensuring a nearly linear relationship between airbox pressure and valve position. Figure 2.4 depicts the "valve map" (the static-flow relationship between pressure and velocity) for the perfectly symmetric valve/disk arrangement (which is shown schematically in Figure 2.2) in a pressure chamber with fixed volume and very small leakage. The gradient of pressure with respect to valve position at high magnitudes of suctions and pressures is roughly 30 times the gradient in regions closer to 0 pressure (neutral position). This non-linearity would result in increased complexity of an already complex control system, significantly increasing the time critical computing resources required, particularly when operating multiple PLAs. In order to improve the linearity of the valve map with the symmetric disk, stationary tabs with a suitable profile were

introduced to the valve housing. The improved linearity of the modified system can be seen in Figure 2.4. Overall performance of the PLA in fixed volumes and high peak pressures is discussed in Kopp et al. (2010). At much lower pressures, with interconnected pressure chambers, the PLAs still function with high accuracy, as discussed below. Figure 2.5 shows the pressure versus valve position of the symmetric disk under different leakage conditions as indicated. While the pressures at a given valve position reduce with increasing leakage in the airbox, it decreases linearly with increasing leakage. The linearity of pressure versus leakage flow at each valve position allows the control system to automatically adjust to different initial leakage conditions or to adapt to changing leakage conditions during a test.
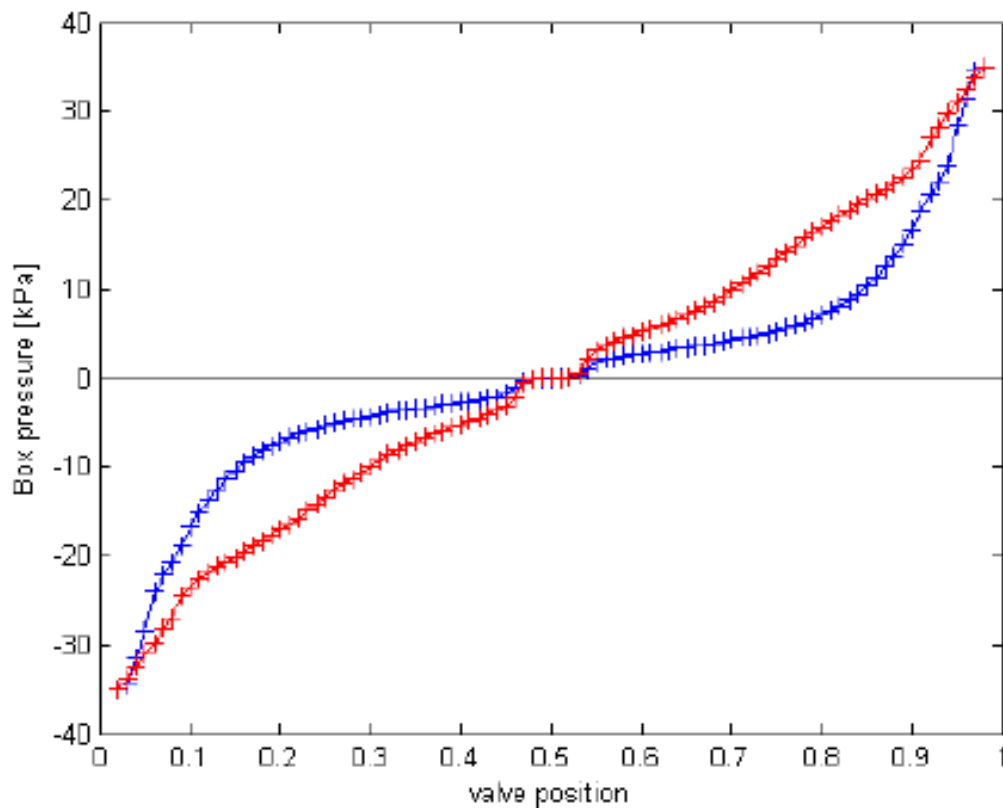
Figure 2.4: A valve map showing the comparison between the 1st generation disk (blue) and the final symmetric disk (red).
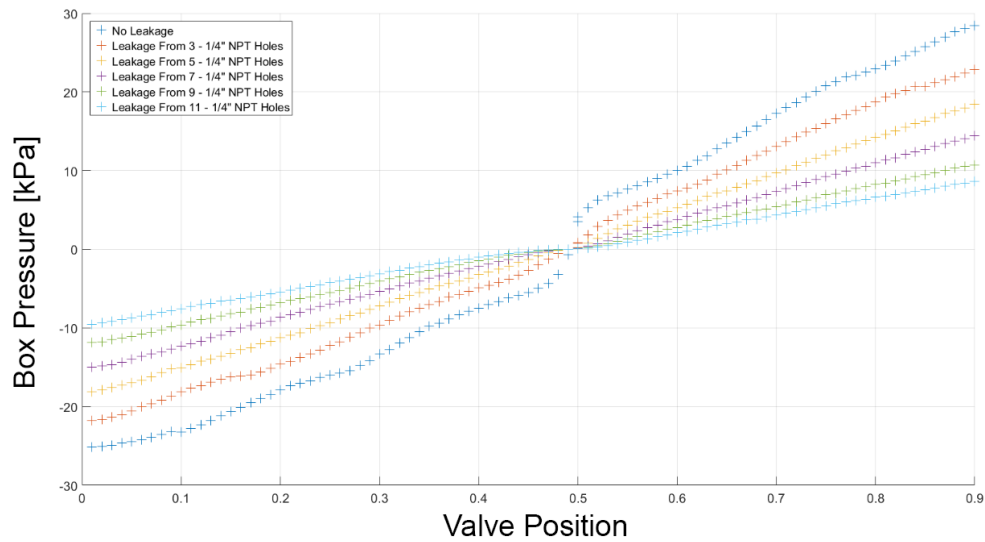
Figure 2.5: A valve map of the final symmetric disk at different leakage conditions.

As can be inferred from the valve maps presented in Figure 2.4 and Figure 2.5, the PLA is a single-input – single-output system with the valve position as the input and the required pressure as the output. Thus, the requested valve position and the measured pressure are an input-output pair for use in a proportional-integral-derivative (PID) control system. The control system is effectively approximated to a linear first-order model as the required pressure trace, whether fluctuating or a simple ramp, is preloaded as a feed-forward term. The feedback PID term is based on the tracking error which is simply the difference between the required and measured pressures. The valve map is used to determine what valve position is required to meet the applied pressure under steady-state conditions resulting in a known system time constant, τ, for the PID control. In calculating τ from the requested pressure and achieved pressure in real-time, the adjacent pressures from the current and previous time steps are used.

Changes in leakage and air-chamber volume cause the time constant, τ, to vary enormously. The solution for this issue was to use gain scheduling, the real-time estimation of τ is used to determine the system gain from a suite of preloaded lookup tables which are generated for known leakage and volumes. However, the system gain (K) increases with increasing τ which (in rare cases) can lead to instabilities with an overestimation of τ, particularly for very small volumes relative to power or input traces that have minimal changes in time (i.e. static pressures or ramp loads). This is only an issue at start up when the control system has no information on τ, that is, the pressure chamber and test element properties. Therefore, a median value of τ and a limit on the increase in K is set for the first 10 seconds of program control. The system learns the chamber's characteristics within this time frame. In cases where absolute control is required in the first 10 seconds, a user defined value of τ can be used. However, this necessitates additional experiments to determine the correct system time constant. With the lookup tables and the linearization of the valve chamber with disc position, the PID control system then can adapt rapidly to changing chamber conditions. The control system was designed this way so that it could adapt to any pressure chamber and input trace (within certain bounds), and still run effectively without any user input into the PID.

The lookup tables scale by a constant factor over the fan speed range of 30 to 70 Hz. (Note that the lower fan speeds are used to avoid operating in a narrow region of the valve control curve, to maintain accuracy in tests that require small excursions around neutral pressure.) The control system predicts the required position of the valve up to 1 second into the future based on the current estimations of air-chamber leakage, user requested pressures and system gain. If the control system anticipates the valve will be unable to meet the pressure

requirements of the user defined input pressure time history, referred to as valve saturation, the fan speed will be increased to meet the demands of the experiment (when possible). This avoids the need for the user to predefine the required fan speed time history in addition to the input pressure time history for the airbox.

Adaptation of the control system is also required when sudden leakage, volume change, or flow change through the cavity occurs. Figure 2.6 shows results from a sinusoidal load applied to a section of metal roof cladding using a 1.8 m x 0.9 m airbox. The achieved pressure trace deviated from the requested trace at approximately 882.2 seconds. This occurred due to a sudden increase in the leakage and the volume of the air-chamber. As can be seen, the system adapts within a tenth of a second. This fast response in adaptation of the PLA control system is important since it is able to maintain the correct pressure loading even as onset of failure of the test specimen occurs.
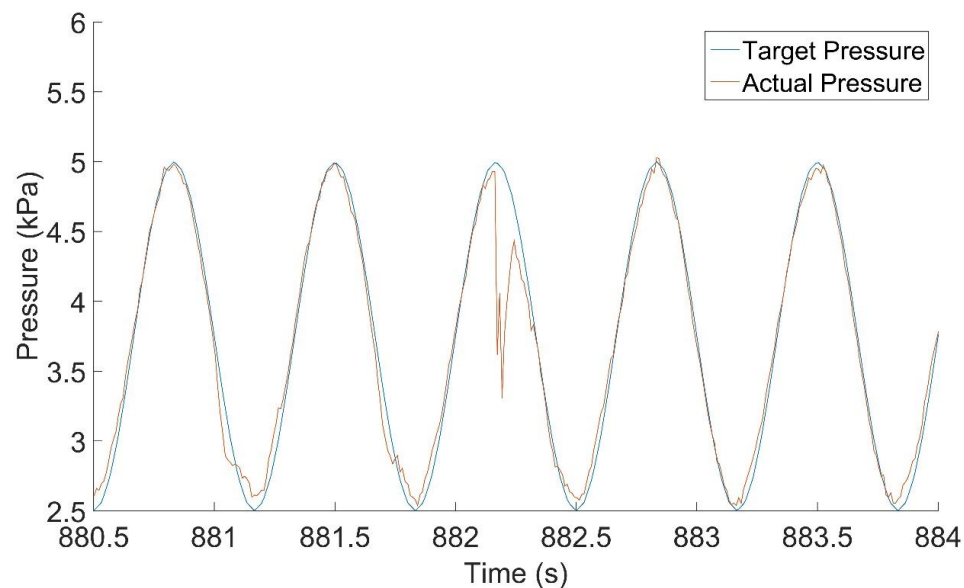
Figure 2.6: A pressure time history showing adaptation of the PID to the change in volume and leakage after the failure of a cladding element. (Data provided courtesy of Dr. David Henderson.)

2.2.5   Airbox Leakage & Fan Performance

Airbox leakage is an extremely important system parameter, and has two possible sources: the test specimen, and leakages through the valve and pressure chamber. The former can be a combination of material porosity and cracks or holes in the test specimen. The latter can be a combination of the pressure chamber fit to the test specimen, the chamber, or the pipes and fittings connected to the pressure chamber. The overall performance of the system, i.e., maximum pressure and frequency response is highly dependent on the amount of leakage. Ultimately the amount of allowable leakage in the system is a function of size of fan or blower used, and, as such, significantly influences the power required to operate the system.

While it may be desirable to purchase the largest fan possible to provide the system with the maximum flow rate possible, there are several practical constraints of why this is not the optimal solution for the current loading system. Such a large fan would require high power consumption even for small, nominally sealed boxes; moreover, the physical size of the fan would be large and make applying spatial gradients, with many pressure chambers in close proximity, more difficult. Finally, in order to accommodate the large flow rates, the size of the valve would also need to be increased so that the air velocity through to valve is kept to a minimum, and consequently the losses. The performance of the entire fan-valve-airbox (nominally sealed) was evaluated by using an orifice plate to measure the flow rate going into the airbox and measuring the achieved pressure. Leakage flow rates were obtained by creating controlled openings within the airbox. In addition, these test were repeated at numerous fan frequencies ranging from 30-70 Hz. The results of these

tests are shown in Figure 2.7. In addition to meeting other requirements such as physical size, the manufacturer's fan curve for the chosen fan is shown in Figure 2.7. The fan combined with the tuned valve is capable of providing flow rates of up to 300 CFM at ~10 kPa and 100 CFM at 20 kPa at a fan speed of 60 Hz. However, as can be seen from the figure, the system does not need to run the fan at full speed, which leads to consequent changes in maximum pressures and flow rates. This, in turn, allows the total power consumption to be reduced in aggregate for an array of PLAs that are running different pressure traces.
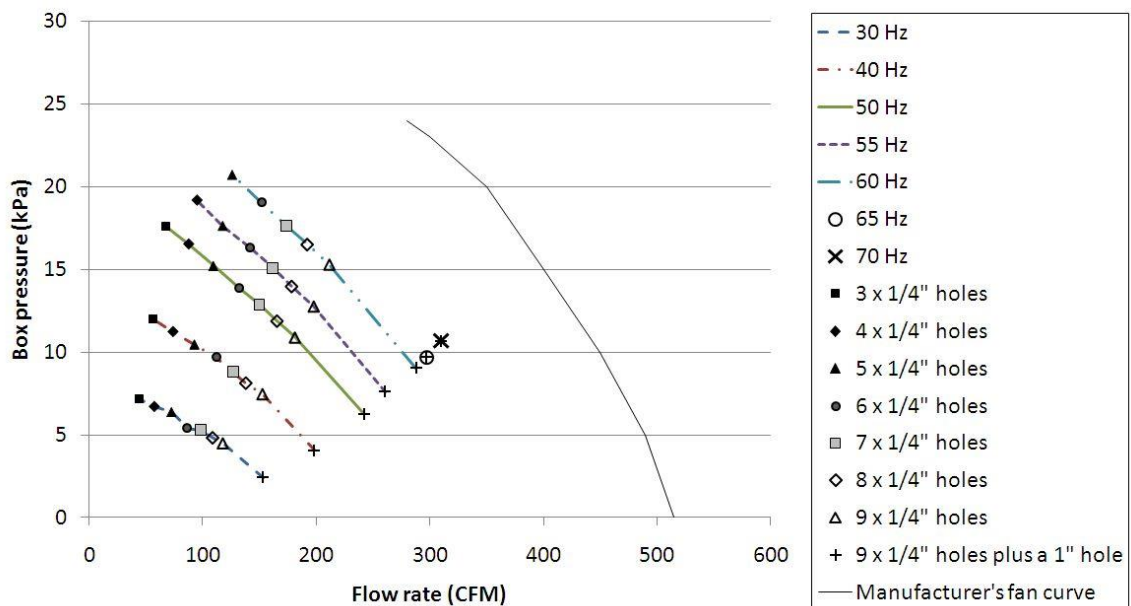
Figure 2.7: A graph of box pressure vs. flow rate for the selected fan at different VSD speeds, along with the manufacturer's fan curve, demonstrating the effect of leakage on the pressure.

To allow greater flexibility, the PLA loading system can be run in three different configurations depending on the application. The first configuration is the simplest where a single PLA unit is connected to a single chamber. The second configuration uses a single

fan/blower connected to two independent valve and servo motors. Each valve is connected to its own box, with its own feedback pressure transducer allowing two airboxes to be controlled independently of each other using only a single fan. This configuration is ideal for small airboxes with minimal leakage and has the advantage of reducing the power consumption of the system, along with reducing the per airbox capital cost of the entire system. The third PLA configuration uses one airbox with multiple individual PLA units. Under this configuration only the first PLA (leader unit) has a pressure transducer and the remaining units mimic the valve movements of the leader exactly. Under this configuration significantly higher flow rates can be realized while maintaining the performance characteristics required to simulate the real wind loads.

These issues led to the development of the Pressure Loading Actuator (PLA) system, which will be used to generate the pressures at the Insurance Research Lab for Better Homes on air-permeable multi-layer cladding systems. Figure 2.8 shows a three-dimensional assembly drawing of the PLA. A fan is used to generate the flow and create the pressure applied to the system. A rotating disk inside the valve, which is controlled by a servomotor, is used to regulate the pressures applied to the system. Further information on how this process operates can be found in Kopp et al., (2010). The PLAs are attached to the pressure chambers, where the wall assembly provides one of the surfaces in the pressure chamber.
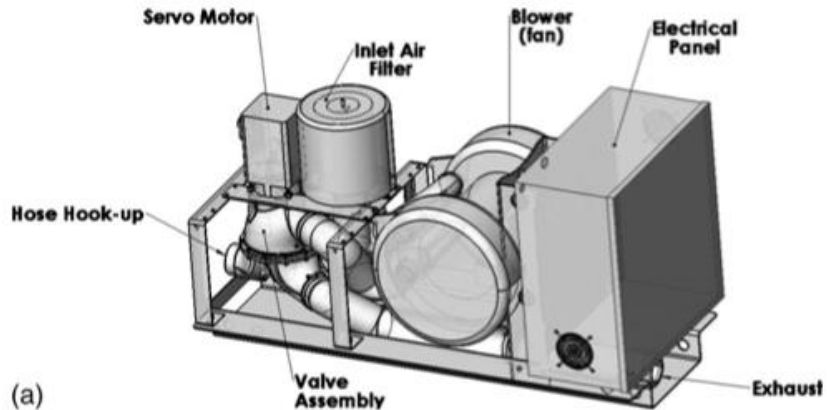
Figure 2.8: Three-Dimensional assembly drawing of a Pressure Loading Actuator (Kopp et al., 2010).

2.3 Full-Scale Pressure Measurements on Vinyl Siding

Recent tests at the Insurance Institute for Business & Home Safety (IBHS) examined the loads on various siding systems using their full-scale wind tunnel (Cope et al., 2012, Cope et al., 2014, Morrison and Cope, 2015). Pressures were measured on the walls of a full-scale, single story wood-frame house with plan dimensions of 9.1 m (30 ft.) x 12.2 m (40 ft.), a mean roof height of approximately 3.7 m (12 ft.), and a roof slope of 4-on-12. The walls of the test building were 2.4 m (8 ft.) high and clad with 11.1 mm (7/16") OSB. In the study done by Morrison and Cope (2015), a total of four siding products were tested: vinyl siding, foam backed vinyl siding, wood siding and hardy board. In order to test all four products simultaneously the walls of the building were divided into eight sub-wall assemblies. The long walls were divided in half resulting in a test wall 6.1 m (20 ft.) long, while the shorter walls extended 3.7 m (12 ft.) from the corner leaving 6 ft. in the center of

the short wall to access the interior of the building. All siding products were installed

following the manufacturer's guidelines; drywall was installed on the interior of the walls

so that the wall assembly matched, as accurately as possible, real construction. Along the

6.1 m (20 ft.) walls, wind-induced pressures were measured at 16 locations, while along

the 3.7 m (12 ft.) walls, they were measured at 12 locations. At each measurement location,

the external pressure, the net pressure across the siding and the net pressure across the OSB

were measured simultaneously. Experiments were conducted in an open exposure at four

different wind speeds (Morrison et al., 2012). The orientation of the building to the wind

was varied over a full 360° in 10° increments. The results of these tests indicate that

pressure equalization has a significant effect on the outer layer of these systems. For

example, results have shown that vinyl siding must carry a net load of up to 75-80% of the

peak net load across the entire wall assembly. Given this 20-25% reduction in loads, the

IBHS results are substantially different than the results obtained using a single-partitioned

pressure chamber or considered through ASTM D3679 (2013). This study is used to

provide benchmark data for validating the multi-chamber pressure-loading approach using

PLAs. In particular, Figure 2.9 shows segments of the measured external pressure time

histories at five locations along the wall from the IBHS experiments – it is these time

histories that are applied in the multi-chamber tests described below.
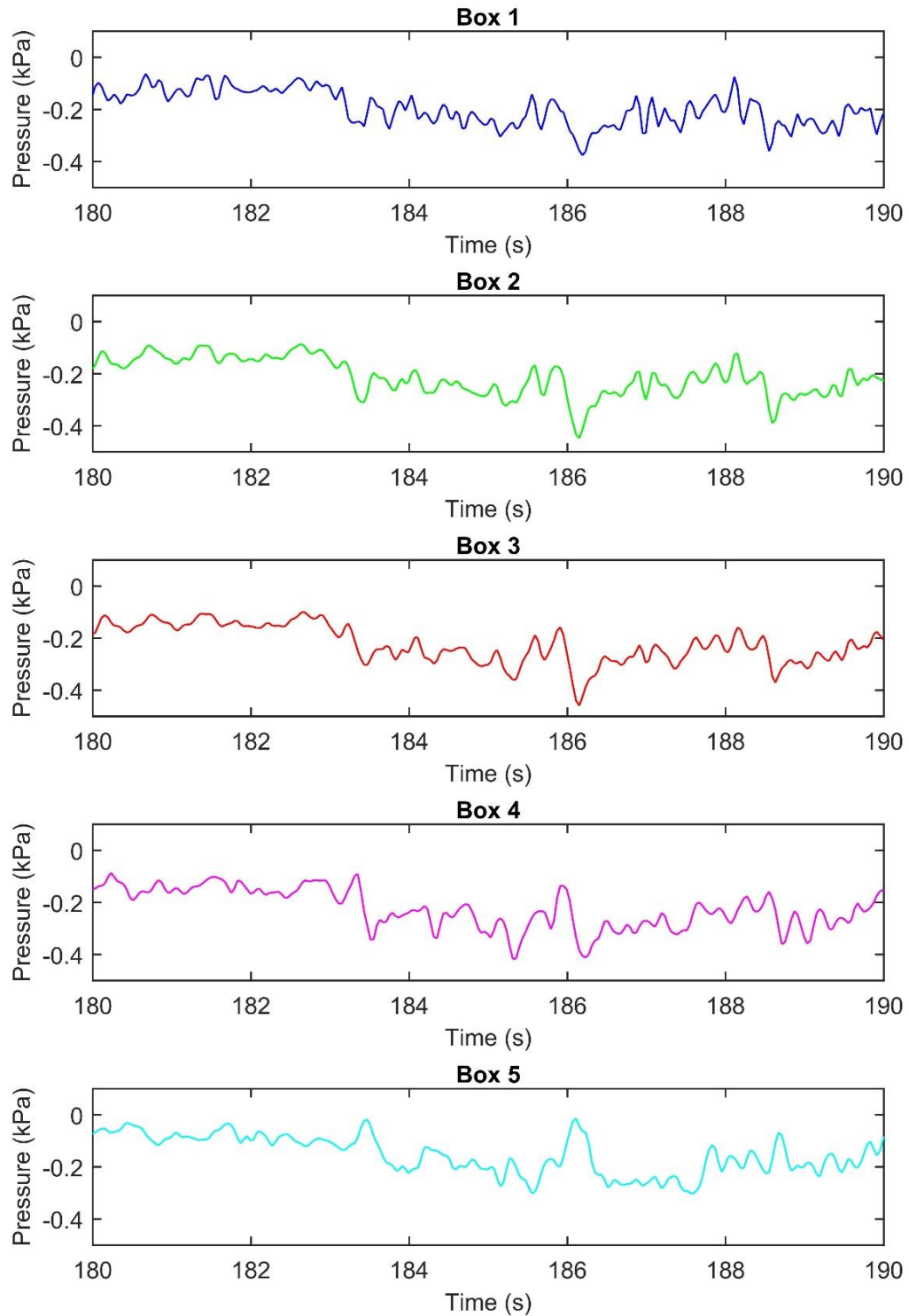
Figure 2.9: A graph showing a portion of the external pressure time history for each individual airbox.

2.4 Multichambered Pressure Test Setup

As described earlier, a new pressure-chamber system is required for testing air-permeable multi-layer cladding systems. The main task is to ensure that the unloaded surfaces are minimized because of the importance of the external pressure gradients on setting the cavity pressure. In addition, the chamber walls should be (i) nominally air-tight, so as to minimize the direct flows between chambers, (ii) flexible, so that the barriers have limited effects on the performance or deformations of the flexible cladding, (iii) strong enough to be robust through a range of test conditions, and (iv) easily installed & repeatable. After taking the material properties into consideration, a latex-barrier system was constructed. Small-scale testing showed that latex worked well in all of its required functions, and, therefore, was implemented for the full-scale testing.

Since the objective was to replicate the IBHS results, test specimens were built with the same siding. These walls were 12 ft. long by 8 ft. high, with 2-by-4s used as the studs. The sheathing was ¾" plywood, however, a polyurethane sheet was placed in between the studs and the plywood to seal the pressure chamber, which is slightly different in set-up compared to the IBHS tests, but which ensures that leakage between the pressure chamber to the atmosphere was minimized. House wrap was then placed over the plywood to replicate typical construction practice, since the focus of the study is the net loads on the outer (i.e., vinyl siding) layer. Pressure taps were then installed through the plywood and house wrap at the same locations as for the IBHS wall. Vinyl siding was installed on to the wall using appropriate nails at 16" intervals along the length of the wall. All pieces of vinyl siding were cut to be 12 ft. long in order to not have any lap splices in the test chamber.

Starter strips, ending strips and utility trim were also used to model typical construction practice. The test wall could then be placed in a rigid-sided chamber of slightly larger dimensions than the test wall, which in this case is the same chamber used by Gavanski & Kopp (2011). Five chambers were created within the airbox for this test by placing four latex barriers within the larger rigid box. These five chambers coincided with the pressure tap layout from the IBHS tests: four of the chambers were 2 ft. long, with one being 4 ft. long. Figure 2.10 gives a technical drawing of the airbox testing rig, and Figure 2.11 gives the locations of the latex barriers and pressure taps on a sample test specimen. All latex barriers ran vertically across the siding, as can be seen in Figure 2.12, which presumes that the primary external gradient was along the length of the wall. This is a reasonable approximation for the side walls when they are under suction, although further work is needed to examine the effects of these gradients. In the current case, with five pressure time histories available, five pressure chambers are used. These data were obtained from the IBHS experiments, as depicted in Figure 2.9. (Regarding the effects of pressure gradients and the use of one set of pressure time histories, as discussed in Biekiewicz & Sun (1997), Oh & Kopp (2014), and shown below, the pressure gradient is clearly one of the governing parameters of the net wind loads on air-permeable cladding elements, with high net loads being associated with high pressure gradients. Due to this, further work is required to determine both appropriate design pressure gradients and the resulting number of required pressure chambers to obtain sufficient accuracy in the tests. This will involve additional wind tunnel testing to examine how the pressure gradients and pressure time histories change with overall building geometry and terrain conditions, compared to the single test case from IBHS).

ELEVATION VIEW SIDE VIEW
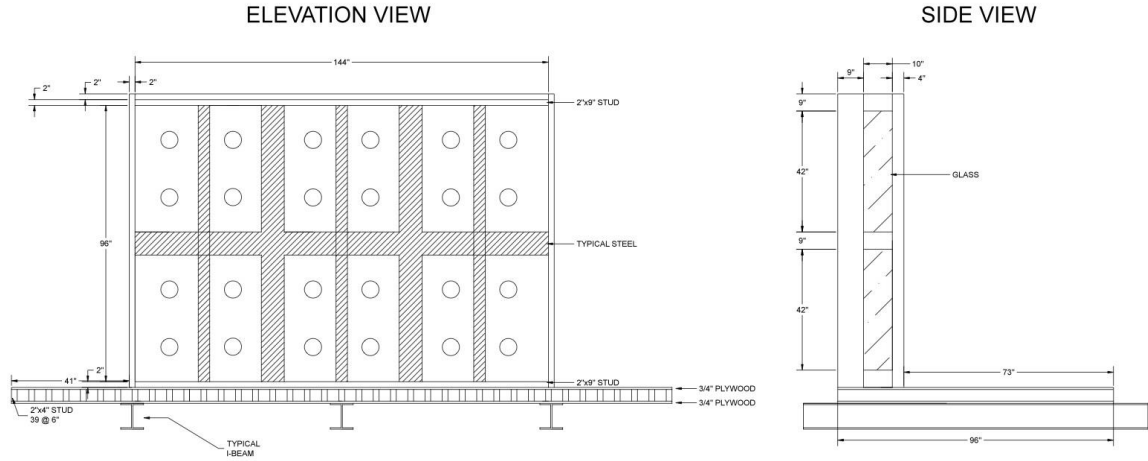
Figure 2.10: Technical drawing of multichamber airbox testing mechanism.

STUD PLACEMENT

PLYWOOD & PRESSURE TAP LAYOUT

LATEX BARRIER SYSTEM LAYOUT

CONSTRUCTION NOTES:

1. All dimensions are edge-to-edge.
2. All dimensions are in inches, unless otherwise stated.
3. Studs are 2'x4', with the long dimension going into the page.
4. All studs should be cut, or provided to the lengths shown on this drawing.

PT LOCATIONS								
PT #	X-Coordinate	Y-Coordinate	PT #	X-Coordinate	Y-Coordinate	PT #	X-Coordinate	Y-Coordinate
1	14"	82"	6	14"	48"	11	14"	23"
2	35"	82"	7	35"	48"	12	35"	23"
3	56"	82"	8	56"	48"	13	56"	23"
4	82"	82"	9	82"	48"	14	82"	23"
5	115"	82"	10	115"	48"	15	115"	23"

Figure 2.11: Technical drawing of a sample test specimen, showing the location of the studs, latex barriers, and pressure taps.

Figure 2.12: A photograph showing the latex barrier system, creating separate airboxes attached to a vinyl siding specimen.

2.5   Results & Discussion

The primary objective of the current tests is to determine whether multi-chamber pressure tests are capable of assessing net pressures on an air-permeable cladding system. This is done by applying the IBHS measurements of external pressures through the PLA system and measuring the resulting pressure equalization factors. Figure 2.13 shows a plot of a segment of the resulting time histories of the differential pressures across the cladding layer (i.e., the vinyl siding) for two cases: one with the external pressures from the IBHS data (see Figure 2.9 above) and one with spatially uniform pressures at each location. For the latter case, the pressure time history with the largest peak external pressure from the IBHS

data was repeated identically in all five chambers. The different colours represent the net

pressures in each separate airbox. The pressure equalization factor is defined as

$$PEF(x) = \frac{P_{external}(x) - P_{cavity}(x)}{\hat{P}_{external}} \qquad [2.1]$$

where $P_{external}(x)$ & $P_{cavity}(x)$ represent the external and cavity pressures, respectively,

at the location on the wall, at a moment in time. While $\hat{P}_{external}$ is the peak external

pressure across the entire wall. (Note that in these experiments there should be negligible

flow or pressure transferred from the interior of the wall because the house wrap provides

a sealing layer. Thus, the net pressure over the assembly from the outside (siding) layer to

the sealed layer is equal to the external pressure. For this reason, we use the external

pressure instead of the net wall pressure in the definition of the *PEF*.) The data in Figure

2.13 indicates that the peak differential pressures across the siding layer are about 350 Pa,

while the peak external pressures are about 400 Pa. Thus, under spatially and temporally

varying pressures, the reduction of the largest net pressure to the largest external pressure,

is about 12%, leading to an approximate peak PEF of 0.88. This result is substantially

different when compared with the data obtained from uniform, but time-varying, external

pressures, where the largest peak differential pressure across the siding layer is about 40

Pa. Thus, under fluctuating uniform pressures, the net reduction relative to the peak

external pressure is about 90%. This result is consistent with the findings of Gavanski and

Kopp (2012) but leads to an even larger reduction than that used in ASTM D3679-13

(although it is reasonably consistent with the data obtained from the study performed by

Architectural Testing Inc. who obtained PEFs between 0.03 to 0.18; (ATI, 2002). These results definitively show that the spatial pressure gradient is a critical parameter for the process of pressure equalization and neglecting it leads to highly erroneous loads for these types of cladding systems.

Figure 2.14 presents a comparison of the pressure equalization factors from the IBHS full-scale wind tunnel experiments and the current multi-chamber pressure-based experiments. As with the previous plots, the different colours represent the PEF in each chamber, with the colours from the two experiments matched. Between the two results, the multi-chamber airbox results seem to be deviating less from the mean. This is most likely because, although this new method of multi-chamber airbox testing is a step forward in the accuracy of the net pressure on cladding elements due to the application of spatial gradients, the spatial gradients being applied are still highly simplified. Due to limited tap resolution from IBHS, there may be subtle differences in the spatial distribution between tap locations that were not captured in original testing and which are made uniform within each airbox in the current tests. Although, to match this spatial distribution, further airboxes would need to be added, which would further affect the stiffness of the system.

a)
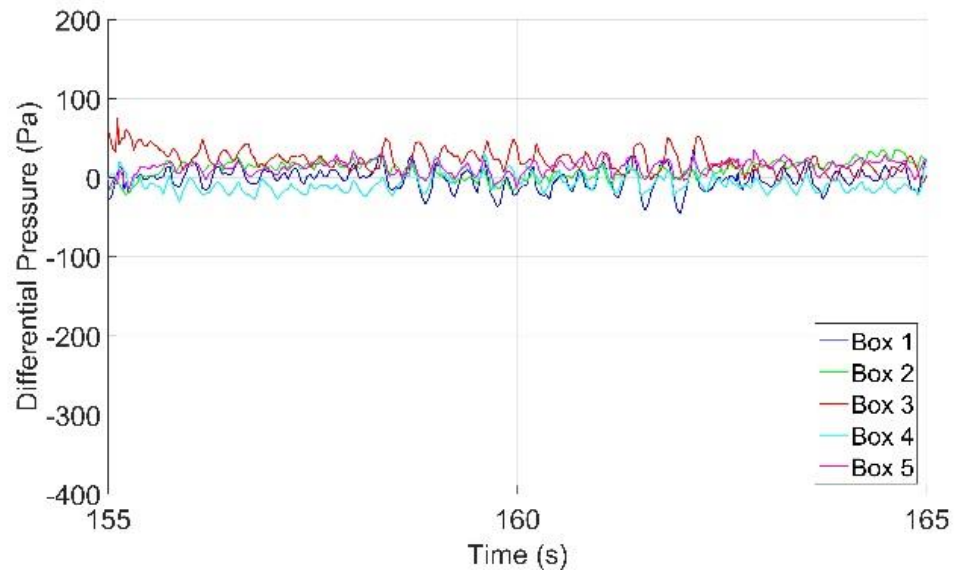
b)
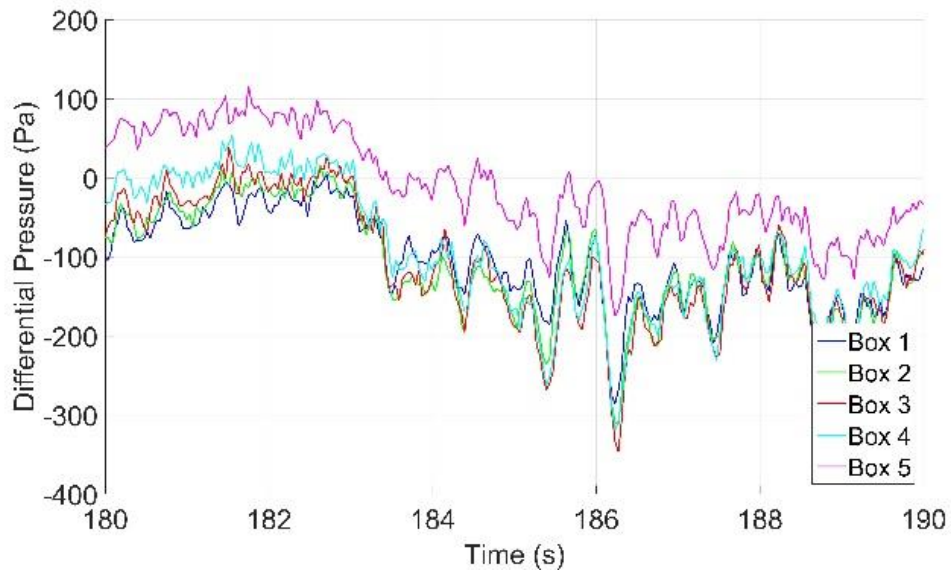
Figure 2.13: Measured differential pressure time histories under (a) uniform and (b) gradient external pressures.

(a)
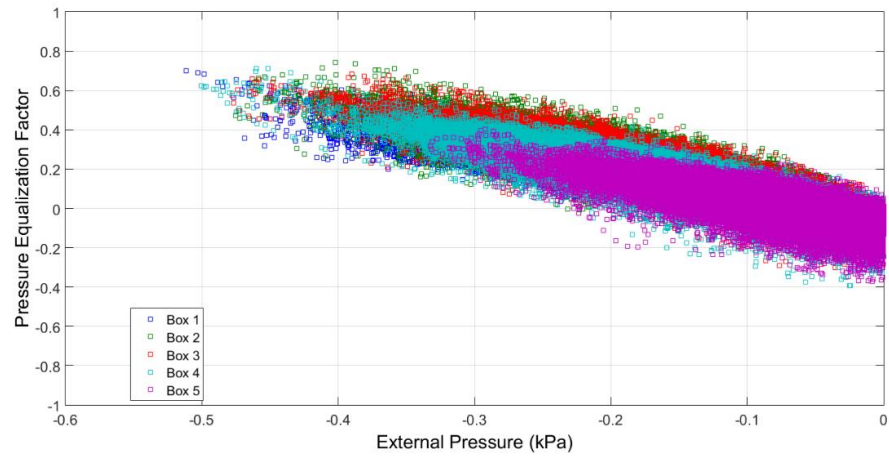
(b)
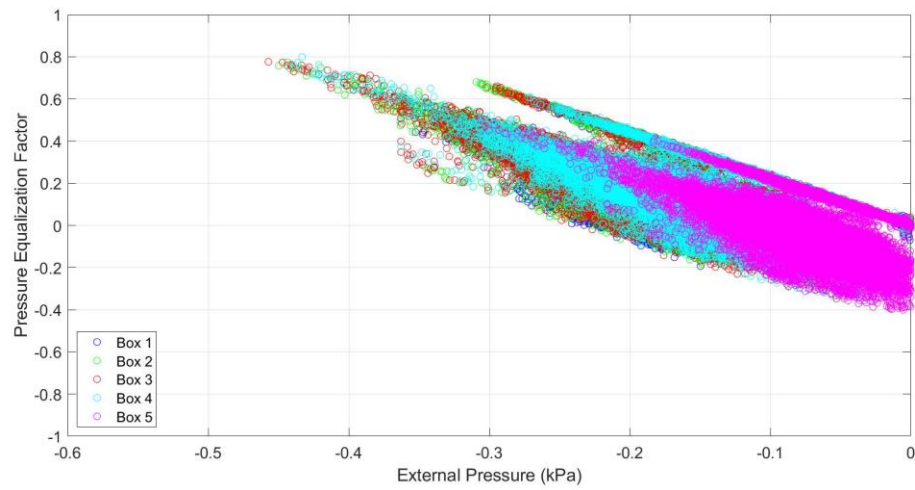
Figure 2.14: Measured pressure equalization factor, normalized by the peak external pressure from the (a) IBHS wind tunnel and the (b) current multi-chamber pressure tests.

The PLA system was able to simulate the applied external pressure time histories from IBHS results, with minor smoothing of the peak pressures. Recent model scale testing of multi-layer roof systems suggests that the short duration, localized peak pressures control the cavity pressure, and the resulting net wind loads, to a significant extent. (Oh & Kopp, 2014) This will have some effect on the results, but as shown in Figure 2.14, the distributions of the PEF values are similar, even with the minor smoothing of peak pressures. In fact, the pressure equalization factor values are higher during the multi-chamber airbox testing, when compared to the IBHS wind tunnel experiments. In addition, further research is needed to define the number of pressure chambers actually required, along with analysis of data to determine design pressure gradients to go with the peak pressures.

To determine whether a static, multi-chamber pressure test may be useful for a test standard, the external pressures at the moment that caused the peak pressure equalization factor in Figure 2.14 were applied (i.e., all temporal variations were eliminated except for the rapid change in external pressure from zero to the target values). Figure 2.15 shows the resultant PEF value, plotted against time. The results of this test show that the largest steady-state PEF is slightly larger than that obtained in the dynamic tests, although it is only about 5% higher. This suggests that static, but multi-chamber, pressure tests are feasible for a test standard so that the complexity of using the PLA system may not be required in standardized product tests. Interestingly, the temporal gradient of the rapidly changing pressure in the test caused a temporary increase of the maximum PEF in two of the five pressure chambers, which, considering that the PEF in the dynamic test is due to peak pressures that also had rapid variations, indicates there is a complexity in the temporal

aspects of pressure equalization, as found by Oh and Kopp (2014). In the present case, having the pressures jump from zero to their final values, the magnitude of the load was only altered by about 10% compared to the final steady values.
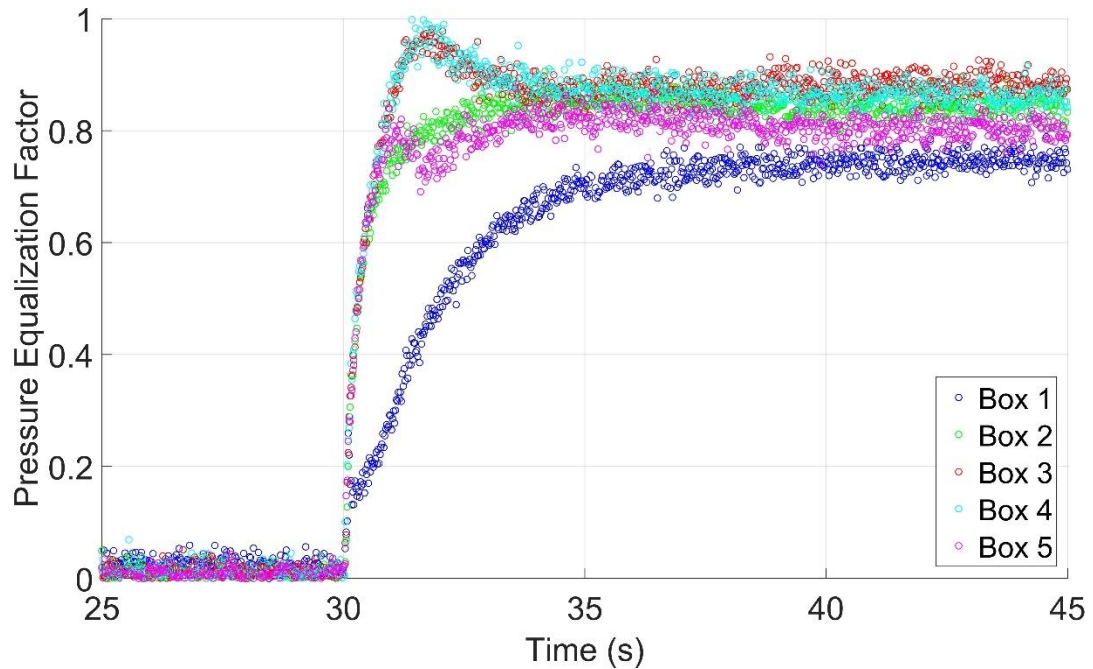
Figure 2.15: Pressure Equalization Factor as a function of time for a sudden change of the pressure with time, including external spatial pressure gradients.

2.6 Summary

An experimental study was conducted to determine whether multi-chamber airbox testing is feasible for assessing wind loads on air-permeable, multi-layer cladding systems. Although there is airflow between individual airboxes and uncontrolled volume changes caused by shared barriers for the pressure chambers creating complications for the PLA control system, the concept of creating a multi-chamber, pressure-based, testing apparatus

that can accurately obtain wind loads for air-permeable, multi-layer wall systems with flexible cladding has been shown to work. This was accomplished by (i) the creation of multiple flexible latex barriers to enable the application of multiple, discrete, time-varying loads across a test specimen, (ii) the development of linearized five-port, flow-reversing valve, in conjunction with (iii) an adaptive PID control strategy. Using this multi-chamber pressure loading system together with external pressure data obtained at the full-scale IBHS wind tunnel, cavity pressures and pressure equalization factors were found to match the full-scale results reasonably well. The results confirm the conclusion of Cope et al. (2013) that the pressure equalization factor in ASTM D3679-13 is unconservative. The good news is that static multi-chamber-based pressure tests are able to capture the important features of pressure equalization. However, the lack of design spatial gradients make it challenging to determine an appropriate amount of airboxes.

3   Aerodynamics of Air-Permeable Multilayer Cladding

3.1   Objectives

Roof cladding systems, such as the discontinuous metal roofing (DMR) system in Figure 3.1, raise questions about which mechanism governs since there is a relatively large volume cavity between the panels and the (inner) roof surface, while having larger steps between the rows of panels. As explained in Chapter 1, it is unclear whether the mechanism that creates peak net loads on these systems is related to local flow around the panel creating uplift, or whether pressure equalization governs. Figure 3.2 shows a sketch of a typical air-permeable multilayer system. In this drawing, the distinction between a cavity pressure and the internal pressure of the building is shown, while various geometric parameters are defined. Since DMR is shaped like shingles, this would suggest that the uplift model is appropriate, but it does have gaps with a cavity beneath it, suggesting that pressure equalization occurs. The reason for these conflicting models is due to the fact that, while the external wind loads are known, air flow through the cavity is not. Due to that, the mechanism that creates peak net loads on air-permeable multilayer systems is unknown.

With this in mind, the objective of the chapter is to determine what factors generate peak net loads in theses air-permeable multilayer cladding systems. In order to accomplish this, this study will measure and examine both external and cavity pressures for two discontinuous metal roofing products in order to determine the wind loads on these products and assess which mechanism controls the wind loads. Full-scale experiments are used to eliminate any uncertainty caused by Reynolds number effects and the manufacturing of fine geometric parameters at model scale.

Figure 3.1: Photograph of the test building located in the IBHS test chamber. The two halves of the roof are clad with two different discontinuous metal roofing products.

Pe = External Pressure
Pc = Cavity Pressure
Pi = Internal Pressure
G = Gap between panels
H = Cavity Depth
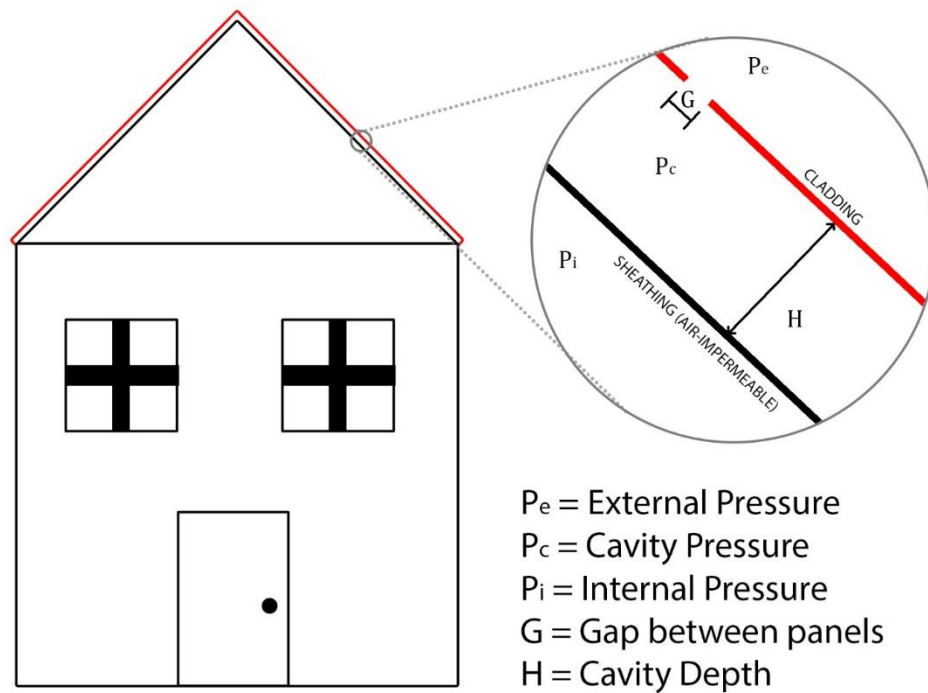
Figure 3.2: Definition sketch for a typical air-permeable multilayer residential cladding system, assuming a mostly air-impermeable inner sheathing layer.

3.2   Cavity Flow Theory

3.2.1   Internal Pressures

In general, models for internal pressures (which assume a uniform pressure within the internal volume) do not work for cavity pressures due to the unsteady flow through the cavity, and spatial pressure gradients within relatively small volumes, which have multiple openings. The analytical modeling of internal pressures using a Helmholtz resonator model was introduced by Holmes (1979). From that model, it has since been shown through multiple studies (e.g., Vickery, 1986; Sharma, 1997; Oh et al., 2007) that it is possible to compute the internal pressure time history via the external pressure time history, the location and geometry of the openings, and the internal volume. Kumar (2000) used the Helmholtz resonator model to model loads on rainscreen walls, considering the effects of unsteadiness on uniform cavity pressures, making it similar to the internal pressure problem. This model relies on compartmentalization of the cavity pressures, which is not necessarily the case for other air-permeable multilayer cladding.

Sun and Bienkiewicz (1993) improved on this by modeling the mean cavity flow for on roof pavers but neglected the temporal fluctuations of the surface pressures. Oh & Kopp (2014) extended the work of Sun and Bienkiewicz (1993) by developing a numerical model using the unsteady Bernoulli equation, and the equation for flow between parallel plates to determine the cavity pressures within a double-layer roof system. These authors showed that the flow through the opening in a building is mostly driven by the pressure difference at the openings, and not momentum driving the flow into the opening, and were able to capture the spatial and temporal pressure gradients within the cavity.

3.2.2   Neutral Pressure Line

The concept of using neutral pressure lines to determine the internal pressures acting on a building was first introduced by Emswiler (1926) and built upon by Tamura & Wilson (1966). The neutral pressure line is the location where there is no pressure difference across the building envelope due to the external and the internal pressures being equal. On a tall building, a neutral pressure line can be created by the stack effect of the building, which is the upward flow of heated gas either through a chimney, elevator shaft, or other large openings in the building due to the difference in temperatures (and therefore, the densities) between the inside air and the outside air.

Along with developing an analytical model for cavity flow, Oh & Kopp (2014) also examined a similar neutral pressure line concept for cavity pressures in air-permeable multilayer cladding systems. As mentioned earlier, cavity pressures are often uniform, which occurs when the losses through the gaps are significantly larger than the friction losses of the flow through the cavity volume. Typical stack effect models have a slight variation in the internal pressures. Using this assumption, a schematic demonstrating the concept of a neutral pressure line for a double-layered system is shown in Figure 3.3.
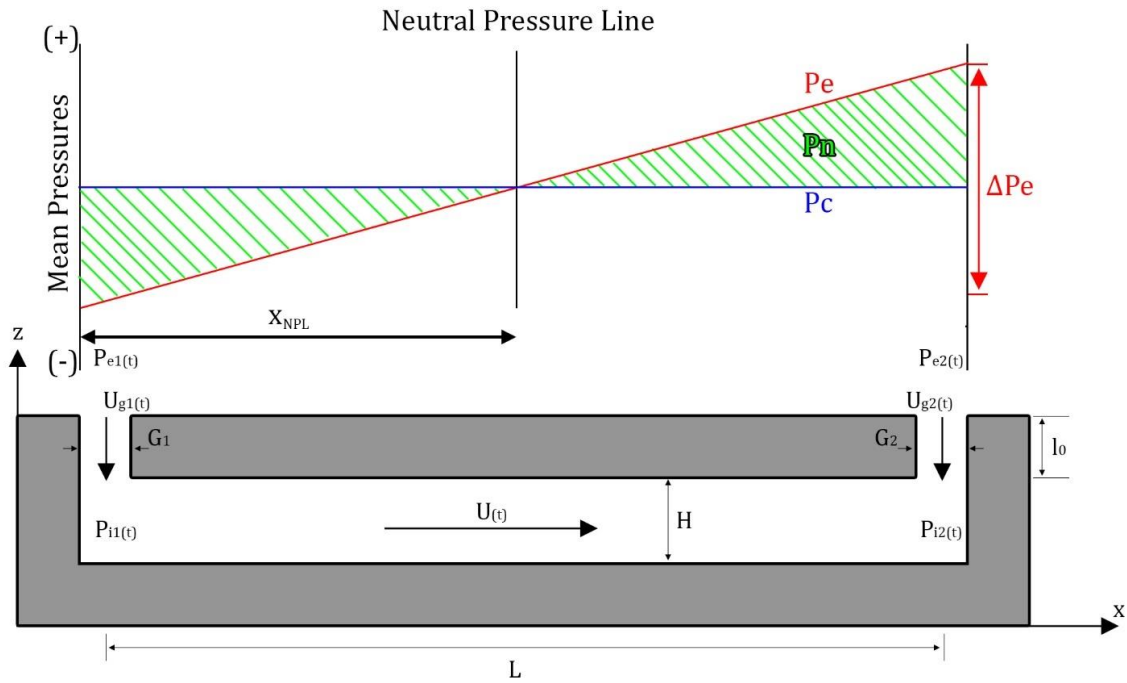
Figure 3.3: Ideal mean pressure distributions on the external surface and cavity of a panel, demonstrating the effect of a neutral pressure line.

If L is the length between the two cavities and x_{NPL} is the location of the neutral pressure line, the ratio of net pressures at the openings to can be defined as a function of the neutral pressure line,

$$\frac{x_{NPL}}{L - x_{NPL}} = \frac{|p_{n_1}|}{|p_{n_2}|}$$

[3.1]

where p_n is the net pressure and the subscripts indicate locations 1 & 2 as shown on Figure 3.3. The flow rate through an opening is given as:

$$Q_g = AU_g$$

[3.2]

The Bernoulli equation applied to the flow through the sharp orifice gap in the panel (and neglecting unsteady flow, for the moment) is:

$$p_e = p_c + C_L \frac{\rho U_g^2}{2} \qquad [3.3]$$

where p_e & p_c are the external and cavity pressures respectively, C_L is the loss coefficient, ρ is the density of air, U_g is the wind speed through the gap in the cladding, and assuming $G \ll H$. Substituting equation 3.3 with equation 3.2 allows for an expression of the flow rate through a gap as a function of the net pressure,

$$Q_g = A \sqrt{\frac{2p_n}{C_L \rho}} \qquad [3.4]$$

Implementing conservation of mass (i.e., $Q_{g1} = Q_{g2}$) through the cavity

$$A_1^2 \frac{2p_{n_1}}{C_L \rho} = A_2^2 \frac{2p_{n_2}}{C_L \rho} \qquad [3.5]$$

and rearranging for the net pressure ratio allows for a substitution into equation 3.1, such that

$$\frac{x_{NPL}}{L - x_{NPL}} = \frac{A_2^2}{A_1^2} \qquad [3.6]$$

assuming $C_{L_1} = C_{L_2}$. Solving for the location of the neutral pressure line,

$$x_{NPL} = \frac{L}{1 + \dfrac{A_1^2}{A_2^2}} \qquad [3.7]$$

or, re-arranging

$$1 + \frac{(G_1 l_1)^2}{(G_2 l_2)^2} = \frac{L}{x_{NPL}} \qquad [3.8]$$

where G is the gap width (see Figure 3.3) and L is the length (out of the page in Figure 3.3). If all cavity openings have the same length and only differ in their width (i.e., $l_1 = l_2$),

$$\frac{G_1^2}{G_2^2} = \frac{L}{x_{NPL}} - 1 \qquad [3.9]$$

Using the equation for conservation of mass,

$$G_1 U_{g1} = -G_2 U_{g2} \qquad [3.10]$$

noting the sign convention for the flow speeds in Figure 3.3, yields,

$$\Delta p_e = p_{e1} - p_{e2} = C_L \frac{\rho}{2} U_{g1}^2 \left[1 + \frac{G_1^2}{G_2^2} \right] = C_L \frac{\rho}{2} U_{g1}^2 \frac{L}{x_{NPL}} \qquad [3.11]$$

An interesting point to note is that for any anti-symmetric external pressure distribution, if the neutral pressure line is located in the middle of the panel, the overall net pressure on the panel is zero. This occurs when both openings are of equal width (i.e., $G_1 = G_2$). Any external distribution passing through the same external pressures at the openings will lead to the same cavity flows, and, therefore, the same cavity pressures; however, the overall net loading will be different. Since the external pressure distribution across a building surface is quite varied, the net loads can also be quite varied. Thus, presuming that external pressures can generally be known, determination of the cavity pressures becomes the objective (which is easier than measuring the flow rates through the cavity or openings).

3.2.3   Cavity Pressures

With the knowledge that cavity flows in air-permeable multilayer cladding are related to external pressure differences, one could define the peak cavity pressures as a function of the peak external pressure differences. For a segment of cladding with, for example, four relatively small openings (as illustrated in Figure 3.4), and a large cavity volume, along with incompressible laminar flow, the Oh & Kopp (2014) model can be expressed as:
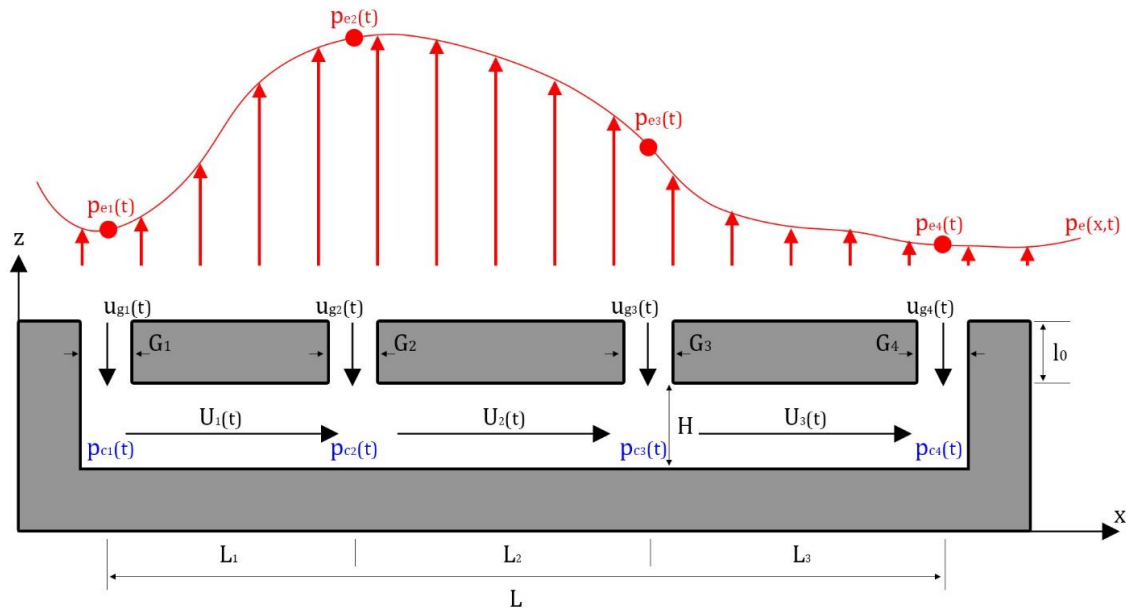
Figure 3.4: Pressure model of a flow in a double-layer system with four openings (after Oh & Kopp (2014)).

$$\rho l_{e1}\dot{U}_{g1}(t) + C_{L1}\frac{\rho}{2}U_{g1}(t)|U_{g1}(t)| + \frac{12\mu l_{01}}{G_1^2}U_{g1}(t) = p_{e1}(t) - p_{c1}(t) \qquad [3.12]$$

$$\rho L_1\dot{U}_1(t) + \frac{12\mu L_1}{H^2}U_1(t) = p_{c1}(t) - p_{c2}(t) \qquad [3.13]$$

$$\rho l_{e2}\dot{U}_{g2}(t) + C_{L2}\frac{\rho}{2}U_{g2}(t)|U_{g2}(t)| + \frac{12\mu l_{02}}{G_2^2}U_{g2}(t) = p_{e2}(t) - p_{c2}(t) \qquad [3.14]$$

$$\rho L_2\dot{U}_2(t) + \frac{12\mu L_2}{H^2}U_2(t) = p_{c2}(t) - p_{c3}(t) \qquad [3.15]$$

$$\rho l_{e3}\dot{U}_{g3}(t) + C_{L3}\frac{\rho}{2}U_{g3}(t)|U_{g3}(t)| + \frac{12\mu l_{03}}{G_3^2}U_{g3}(t) = p_{e3}(t) - p_{c3}(t) \qquad [3.16]$$

$$\rho L_3\dot{U}_2(t) + \frac{12\mu L_3}{H^2}U_3(t) = p_{c3}(t) - p_{c4}(t) \qquad [3.17]$$

$$\rho l_{e4}\dot{U}_{g4}(t) + C_{L4}\frac{\rho}{2}U_{g4}(t)|U_{g4}(t)| + \frac{12\mu l_{04}}{G_4^2}U_{g4}(t) = p_{e4}(t) - p_{c4}(t) \qquad [3.18]$$

where, U is the wind speed through the cavity, $\dot{U}$ is the time-derivative of the speed, and the numbered subscripts indicate the x location in Figure 3.4. This model assumes that the flow is one-dimensional and laminar although generalizing for turbulent flow is straightforward. To find the net load on a single panel (in this case, the panel between locations 2 & 3) in this system, Figure 3.5 shows a section of Figure 3.4 that simplifies the 7 equations by only considering the equations that are required for this portion of the system.
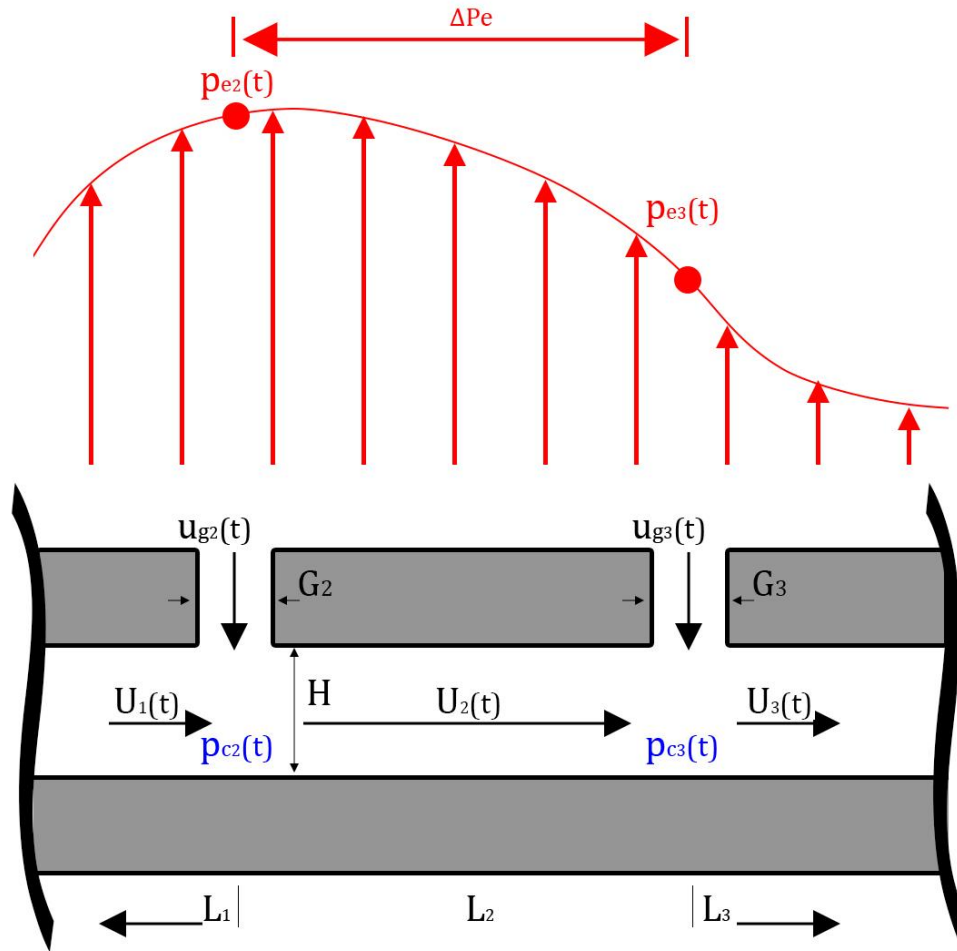
Figure 3.5: Segment of the flow in a double-layer system with four openings (after Oh & Kopp (2014)).

$$\rho l_{e2} \dot{U}_{g2}(t) + C_{L2} \frac{\rho}{2} U_{g2}(t) |U_{g2}(t)| + \frac{12\mu l_{02}}{G_2^2} U_{g2}(t) = p_{e2}(t) - p_{c2}(t) \qquad [3.19]$$

$$\rho L_2 \dot{U}_2(t) + \frac{12\mu L_2}{H^2} U_2(t) = p_{c2}(t) - p_{c3}(t) \qquad [3.20]$$

$$\rho l_{e3} \dot{U}_{g3}(t) + C_{L3} \frac{\rho}{2} U_{g3}(t) |U_{g3}(t)| + \frac{12\mu l_{03}}{G_3^2} U_{g3}(t) = p_{e3}(t) - p_{c3}(t) \qquad [3.21]$$

However, cavity pressures are often uniform, which occurs when the losses through the gaps are significantly larger than the friction losses of the flow through the cavity volume. So, if the assumption of local uniformity is made, along with negligible friction losses at the openings (i.e., $l_0 \ll G$), equations 3.19 – 3.21 above can be simplified to,

$$C_L \frac{\rho}{2} U_{g2} |U_{g2}| = p_{e2} - p_c \qquad [3.22]$$

$$U_2 = -\frac{\rho H^2}{12\mu} \dot{U}_2 \qquad [3.23]$$

$$C_L \frac{\rho}{2} U_{g3} |U_{g3}| = p_{e3} - p_c \qquad [3.24]$$

Using the equations for conservation of mass,

$$G_2 U_{g2} = H(U_2 - U_1) = H\left(-\frac{\rho H^2}{12\mu} \dot{U}_2 + \frac{\rho H^2}{12\mu} \dot{U}_1\right) = \frac{\rho H^3}{12\mu}(\dot{U}_1 - \dot{U}_2) \qquad [3.25]$$

$$G_3 U_{g3} = H(U_3 - U_2) = H\left(-\frac{\rho H^2}{12\mu} \dot{U}_3 + \frac{\rho H^2}{12\mu} \dot{U}_2\right) = \frac{\rho H^3}{12\mu}(\dot{U}_2 - \dot{U}_3) \qquad [3.26]$$

where equations 3.25 – 3.26 can be rearranged to express the cavity pressure,

$$p_c = p_{e2} - \frac{C_L \rho^3 H^3}{288 G_2^2 \mu^2}(\dot{U}_1 - \dot{U}_2)|(\dot{U}_1 - \dot{U}_2)| \qquad [3.27]$$

and

$$p_c = p_{e3} - \frac{C_L \rho^3 H^3}{288 G_3^2 \mu^2}(\dot{U}_2 - \dot{U}_3)|(\dot{U}_2 - \dot{U}_3)| \qquad [3.28]$$

The external pressure difference across the panels can be expressed from this,

$$\Delta p_e = p_{e2} - p_{e3} = \frac{C_L \rho^3 H^3}{288 G_3^2 \mu^2} \left[\frac{(\dot{U}_1 - \dot{U}_2)^2}{G_2^2} - \frac{(\dot{U}_2 - \dot{U}_3)^2}{G_3^2} \right] \qquad [3.29]$$

Substituting into equation 3.27 yields

$$p_c = p_{e2} - \Delta p_e \frac{G_3^2 (\dot{U}_1 - \dot{U}_2)^2}{G_3^2 (\dot{U}_1 - \dot{U}_2)^2 - G_2^2 (\dot{U}_2 - \dot{U}_3)^2} \qquad [3.30]$$

or substituting into equation 3.28 yields

$$p_c = p_{e3} - \Delta p_e \frac{G_2^2 (\dot{U}_2 - \dot{U}_3)^2}{G_3^2 (\dot{U}_1 - \dot{U}_2)^2 - G_2^2 (\dot{U}_2 - \dot{U}_3)^2} \qquad [3.31]$$

Spatial averaging across the panel yields

$$< p_e > = \frac{1}{L_2} \int_{x_1}^{x_3} p_e(x) \, dx \qquad [3.32]$$

$$< p_c > = p_c \qquad [3.33]$$

$$< p_n > = < p_e > - p_{e2} + \Delta p_e \frac{G_3^2 (\dot{U}_1 - \dot{U}_2)^2}{G_3^2 (\dot{U}_1 - \dot{U}_2)^2 - G_2^2 (\dot{U}_2 - \dot{U}_3)^2} \qquad [3.34]$$

where the brackets represent the spatial panel average.

3.2.4   Applications

External pressures are well known, but cavity pressures are not well known for air-permeable multilayer cladding. Therefore, understanding the theory of cavity flow is critical to understanding how air-permeable multilayer systems behave under peak wind loads. This analysis of cavity flow theory highlights a few key applications for potential design guidelines (which are then examined and expanded upon in the experimental section of this study). Firstly, although equations 3.32 – 3.34 are not practical, they do show that the cavity pressure (and by consequence the net pressure) are dependent on the external pressure magnitude, the external pressure difference across a panel, and the geometry of the panel and openings. This analysis also shows that flow inertia in the cavity plays a role in the net pressures as well. The experimental section also examines the assumption of local uniformity and how continuous leakage across multiple panels affects that assumption.

3.3   Experimental Setup

3.3.1   Wind Tunnel Terrain Simulation

Because small geometric details play a crucial role in developing the wind loads on residential air-permeable multilayer cladding systems, full-scale or large-scale measurements are the only accurate method to obtain such wind loads. In the current study, the IBHS Research Center wind tunnel is used with a scale of 1:1 (i.e., full scale). The flow field in the IBHS wind tunnel has undergone a detailed development and validation process

(Standohar-Alfano et al., 2017, Morrison & Kopp, 2018). Figure 3.6 presents vertical, z, profiles of mean velocity, V, and turbulence intensity, I_u, of the longitudinal velocity component used in the current study. In addition, the theoretical profiles obtained from the Engineering Sciences Data Unit (ESDU, 1982) and the field observations obtained from the Wind Engineering Research Field Laboratory at Texas Tech University (Smith, 2010) are included. The ESDU profiles are for a roughness length of 0.01 m, simulating an open country terrain. The overall comparison between the IBHS results and the benchmark profiles is good. The solid, heavy horizontal lines in Figure 3.6 identify the heights of the fan cell boundaries. Effects of the cell boundary can be observed in both the mean velocity and turbulence intensity profiles. The longitudinal turbulence spectra, shown in Figure 3.7, shows generally good agreement with field and theoretical power spectra. However, a spectral gap (decrease in spectral content) exists between wave numbers of 0.01 and 0.1 in the IBHS flow field as compared to both the field observation and theoretical profiles. For wave numbers above 0.1, spectral content for TTU field data fall below theoretical curves as well as other data obtained from field measurements using equipment with higher frequency response characteristics. Despite this spectral gap, Standohar-Alfano et al. (2017) have shown that the surface pressures on a building in the IBHS test chamber match reasonably well with both field observations and model scale wind tunnel results. Complete details of the flow simulation used in the investigation are presented in Standohar-Alfano et al. (2017). For this investigation, the mean (15-minute average) wind speed at mean roof height is approximately 23 m/s (50 mph) for all experiments. This results in a Reynolds number, Re, based on mean roof height (H=5.2 m) of about 8×10^6.
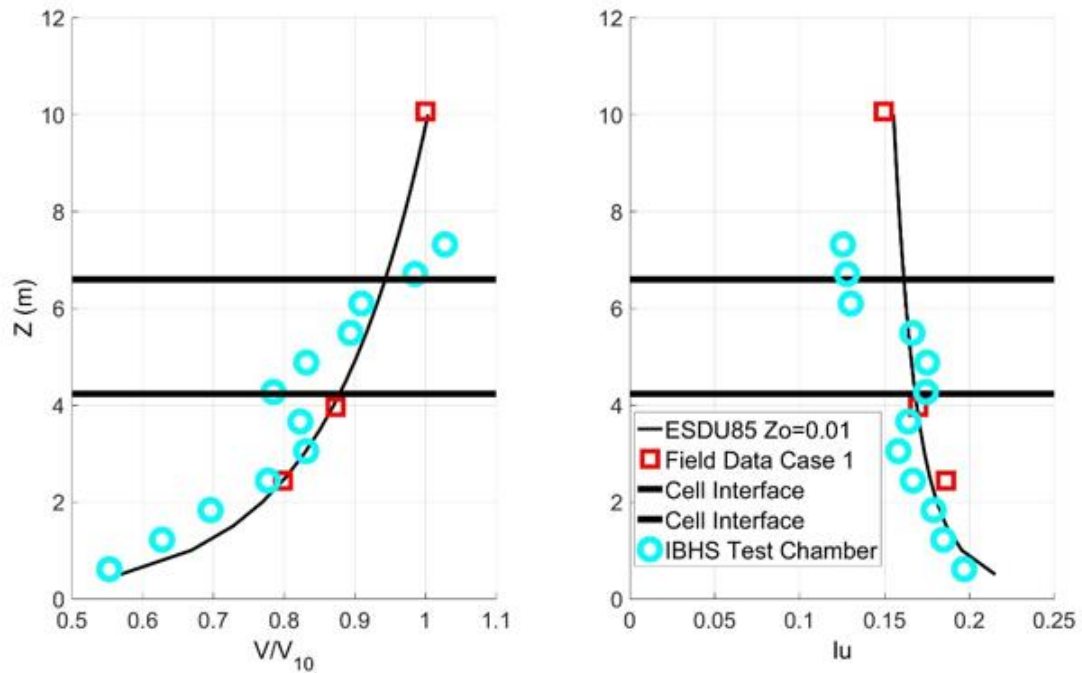
Figure 3.6: Normalized mean velocity and longitudinal turbulence intensity (Iu) profiles.
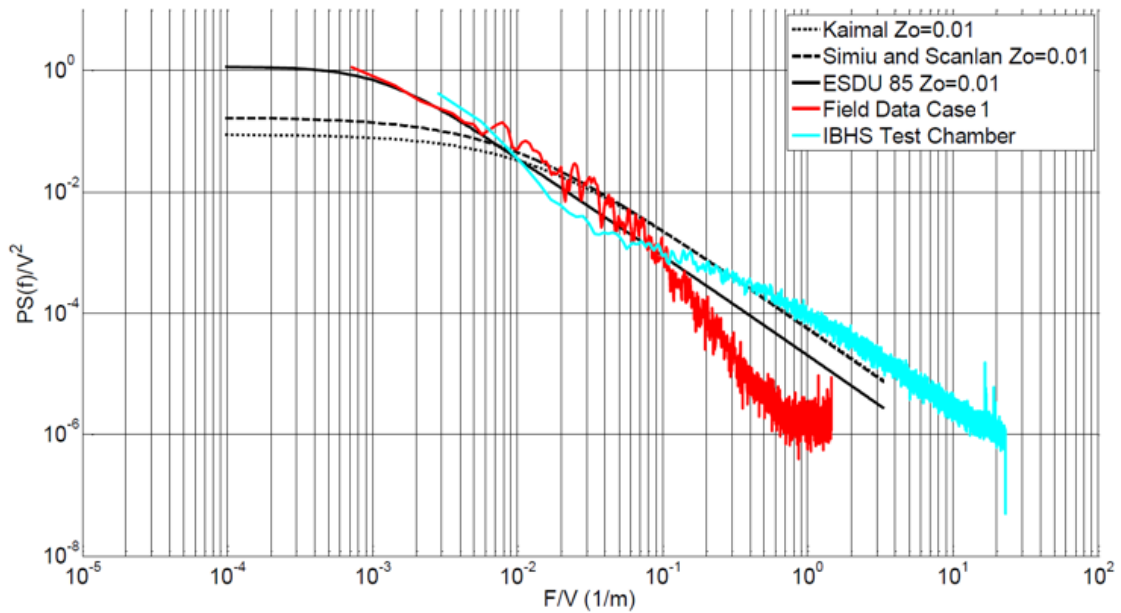
Figure 3.7: Power spectrum of longitudinal velocity component.

3.3.2   Test Specimen – Building Details

A typical single-story residential structure with plan dimensions of 30 ft x 40 ft was used in this study. The mean roof height, H, of the building was 5.2 m (17 ft) with a roof slope of 4:12. The roof was a hip-gable construction; one end of the building had a gable end, while the other had a hip end, as can be seen in Figure 3.1. The roof of the building was built following typical construction practices with oriented strand board (OSB) sheathing and a 30-lb felt with 6-inch lap underlayment. Two different types of discontinuous metal roofing were installed, each taking up one half of the roof. The products selected for testing were determined by the Metal Construction Association and provided to IBHS. Both products were jointly installed by IBHS staff and product manufacturer representatives to ensure that they were installed in accordance with manufacturer guidelines.

Figure 3.8 and Figure 3.9 shows the installation of both products on the roof of the building. Figure 3.8 shows the installation of metal panels on battens attached to the roof sheathing. Figure 3.9 shows the installation of metal shingles, which are attached directly to the roof sheathing. The following section discusses the details of these cladding systems to a much greater extent. Figure 3.1 shows a photograph of the completed test building located on the turntable inside the IBHS test chamber.

Figure 3.8: Photograph of the installation of the metal panels on the test building at IBHS.
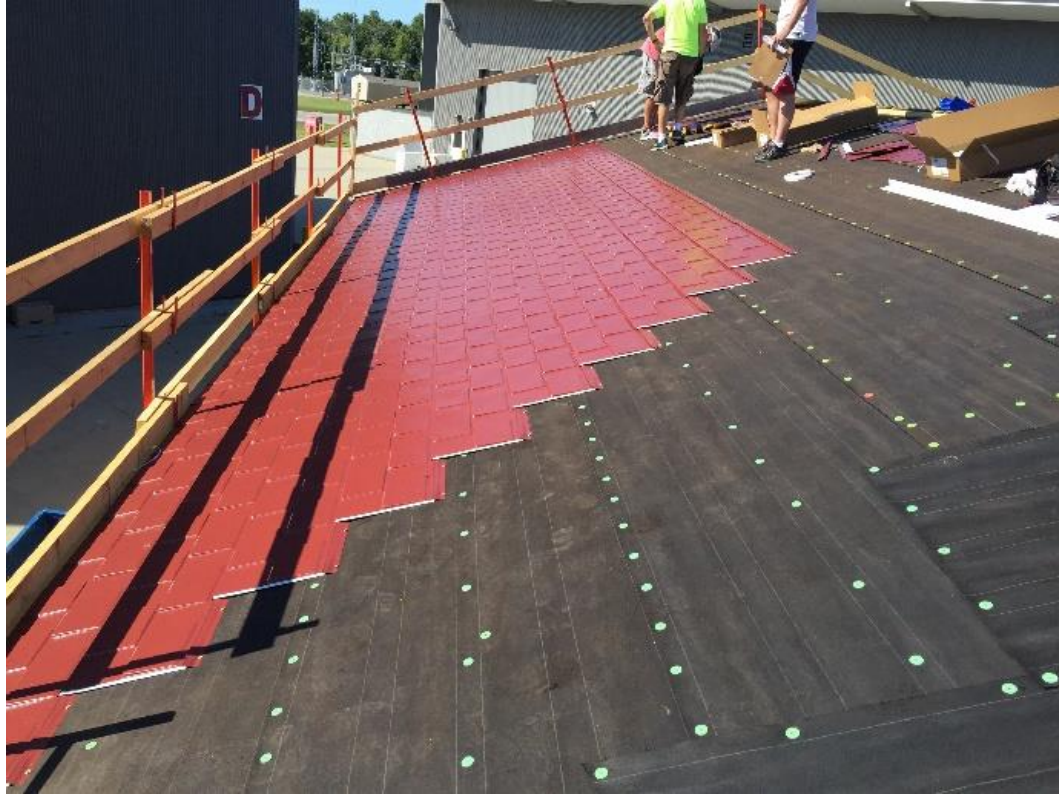
Figure 3.9: Photograph of the installation of the metal shingles on the test building at IBHS.

3.3.3 Test Specimen – Cladding Details

Figure 3.10 and Figure 3.11 show technical drawings featuring the dimensions and connections between panels for the metal shingles and the metal panels, respectively. The metal shingles are nailed through the top of the panel, using the provided guidance holes (pre-manufactured into the cladding), directly into the sheathing. The panels are then connected to one another using lap joints. Trim is used around the edges of the roof to create a complete system. Once nailed to the sheathing, the geometry of the shingles, as shown in Figure 3.10, creates a maximum cavity depth of approximately 12.7 mm (0.5").

Figure 3.12 shows a photograph showing a close-up of the lap joint connections, as well as demonstrating the cavity depth when installed directly on to a flat surface.

The metal panels were installed on 38 mm x 38 mm (nominally labeled as, 2" x 2") battens running lengthwise across the cladding. There are no lap joints used in this system; instead, the cladding is nailed both at the top and bottom through the battens. The cladding overlaps at the top and bottom of each piece of cladding, meaning that when the cladding is nailed to the battens, it goes through both pieces of cladding, creating a pseudo-lap joint. The overlap through the sides of the cladding is not nailed at all. Once nailed to the batten, the geometry of the shingles, as shown in Figure 3.11, creates a cavity depth in the range of 38 mm – 63.5 mm (1.5" - 2.5"). Figure 3.13 shows a photograph showing a close-up of the batten installation, as well as demonstrating the cavity depth when installed on to the battens.

Figure 3.8 to Figure 3.13 show that the two cladding types are markedly different from each other. The metal shingles have a much smaller cavity depth, but the cavity depth is changing linearly across the cladding, with the lap joints restricting the air flowing in and out of the cavity. In contrast, the metal panels have a much larger cavity depth, with a cavity depth varying much more across the cladding. As well, there are no lap joints, allowing air to flow more freely in and out of the cavity. However, since the cavity is not airtight, it is difficult to quantify the size of the gaps, G, into the cavity because this geometry is not specified.
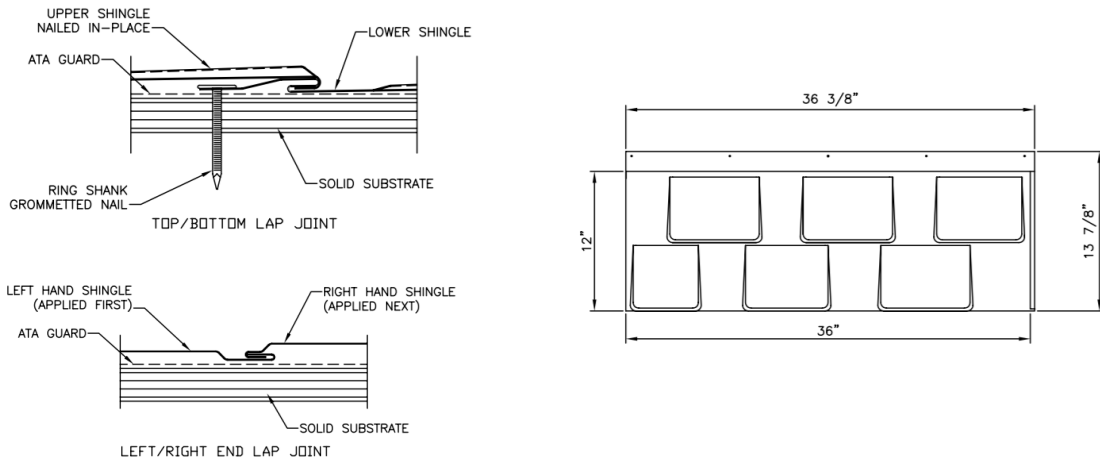
Figure 3.10: Detailed technical drawing of metal shingles, showing dimensions, lap joints, and connections. Dimensions are in inches. (Drawing provided by ATAS International)
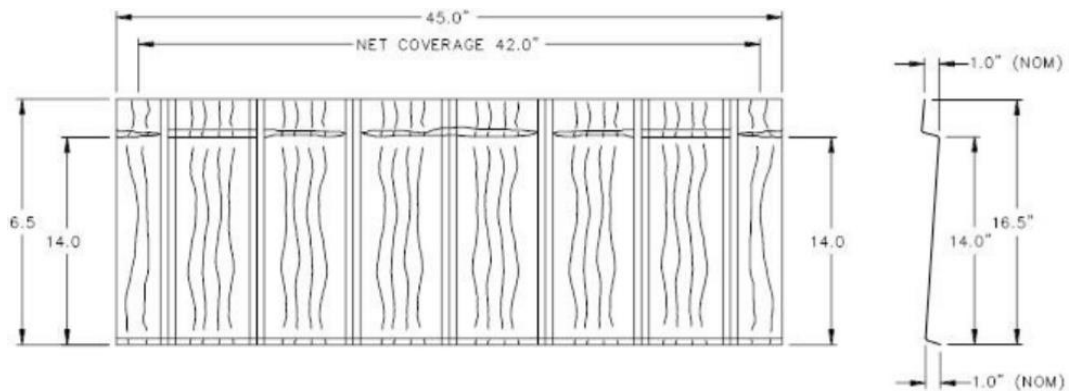
Figure 3.11: Detailed technical drawing of metal panels, showing dimensions, lap joints, and connections. Dimensions are in inches. (Drawing provided by Boral Steel)

Figure 3.12: Photograph of metal shingles being installed on to a flat surface, demonstrating lap joint locations, and cavity details.

Figure 3.13: Photograph of metal panels being installed on to battens, demonstrating nailing locations, and cavity details.

3.3.4   Instrumentation

During the installation of both products, pressure taps to measure the wind-induced pressures were installed on select panels across the roof. At each location where the pressure was measured, two pressure taps were installed. Figure 3.14a provides a schematic of a section view through the roof, showing the pressure transducer configuration at a tap location, while Figure 3.14b provides a schematic of the metal shingle and metal panel showing where each pair of taps is located on each instrumented panel. The top pressure tap is mounted with its opening flush with the outside surface of the metal roofing measuring the external pressure acting on the roof. The bottom pressure tap is mounted with its flush with the roof sheathing measuring the pressure inside the cavity between the metal panels and the roof sheathing. Two differential pressure transducers (sampling at 100 Hz) are used to directly measure the external pressure and the net pressure across the metal roofing as shown in Figure 3.14a. This was accomplished by using one differential pressure transducer to measure the pressure difference between the outside (external) surface and a reference static pressure. The second was then used to measure the pressure difference between the external surface and the cavity pressure. The cavity pressure relative to the static pressure is never directly measured but is calculated by subtracting the measured net pressure from the measured external pressure.

Figure 3.15 shows the layout of instrumented panels and measurement locations for both metal cladding products. The red coloured section of the roof represents the metal shingles, the grey coloured section of the roof represents the metal panels. The pressures were measured at either one or six locations on a single panel, depending on its location on the

roof. The orange tinted panels contained a single pressure tap set, while the yellow tinted panels contained six sets of pressure taps. Single tap locations were used to measure the pressures between the fully instrumented panels. The black dots on the figure show the specific locations of each pressure tap set on a panel. The numbering convention for each panel is also shown on the figure, along with the wind direction, θ, convention for this study. In total, pressures were measured at 106 locations for the metal shingles, and 91 locations for the metal panels, resulting in a total of 394 pressure taps over the entire roof.

a)
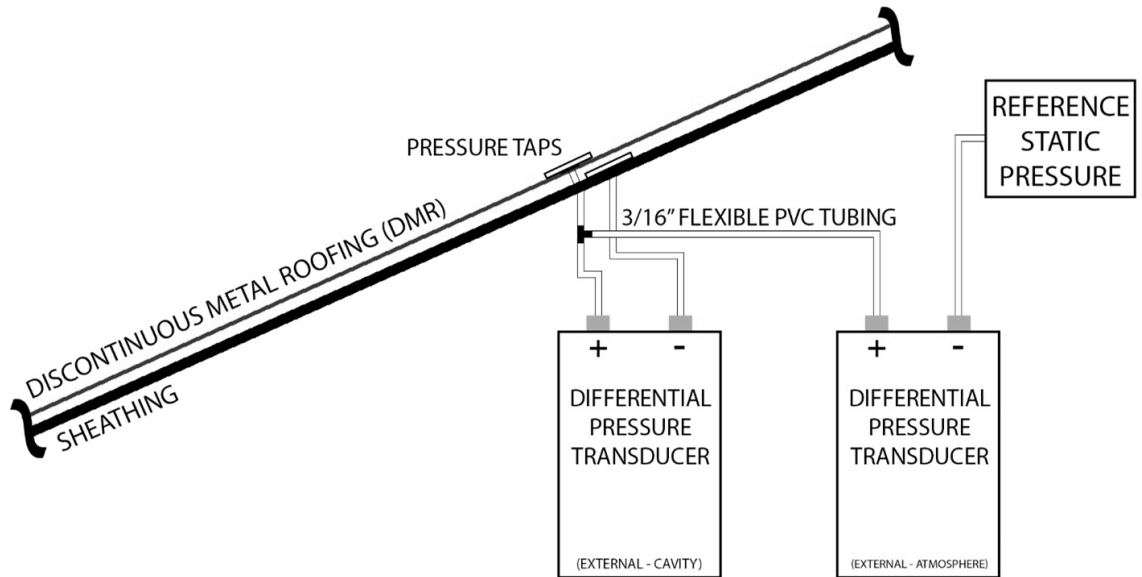
b)
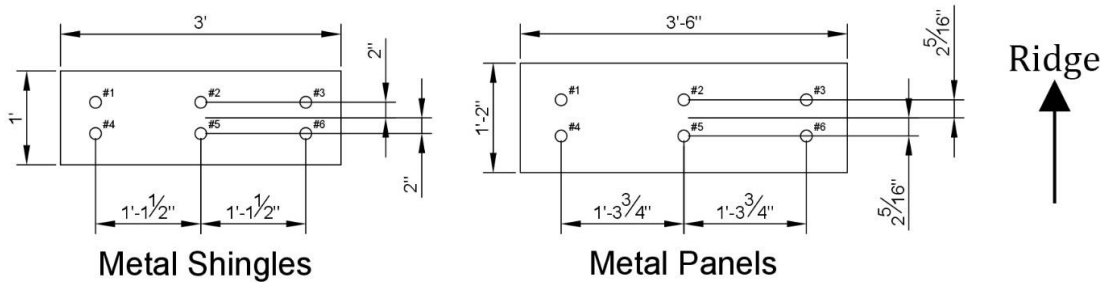
Figure 3.14: (a) Schematic of a section view through the roof, showing the pressure transducer configuration at a tap location. (b) Schematic of metal shingles and metal panels showing the dimensions of the panels, along with the location of the pressure taps.
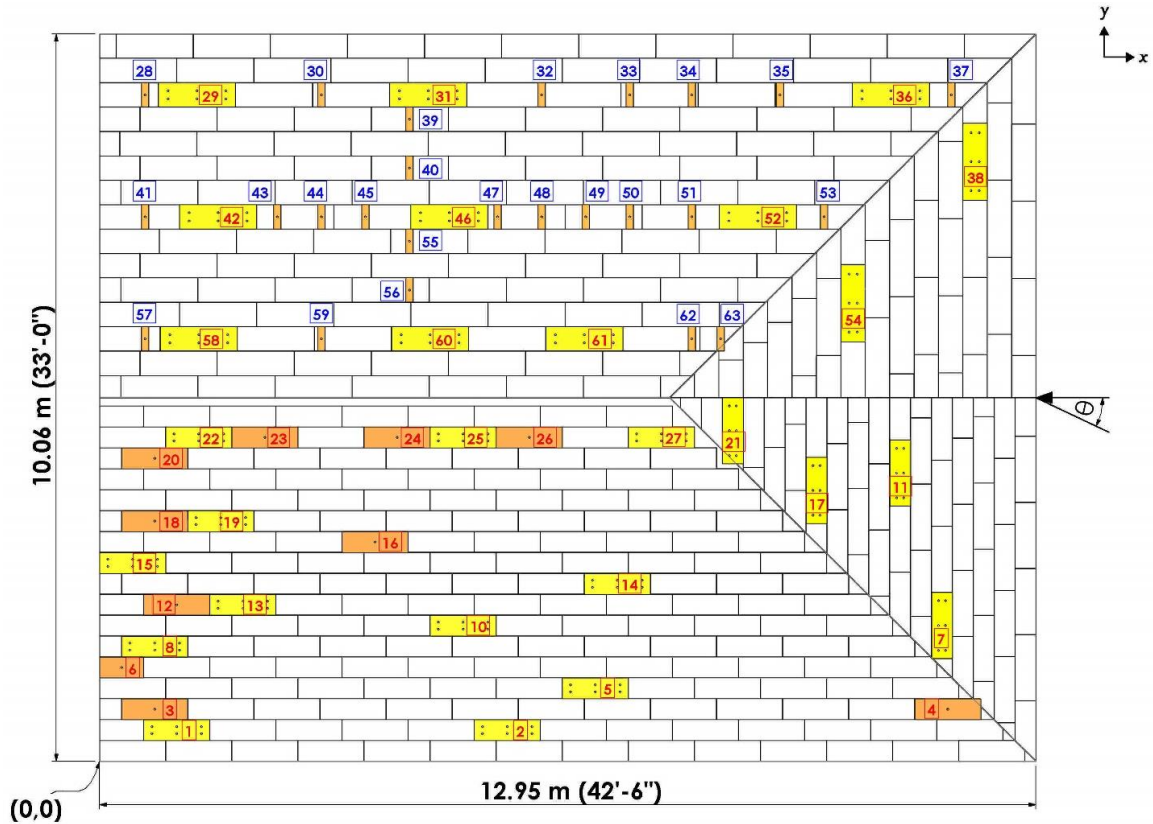
Figure 3.15: Layout of instrumented panels and measurement locations for both metal cladding products.

3.3.5   Data Reduction

The building was tested at wind angles over a full 360 degree range in 10 degree increments. At each wind angle, the pressures were measured from all sensors at a sampling rate of 100 Hz for a duration of 900 seconds. The pressure time histories obtained for each pressure sensor were converted into GCp_{eq} values that are comparable to GCp values provided by ASCE 7-16 (2017). The results presented as GCp_{eq}^{ext} refer to the measured external pressure, GCp_{eq}^{net} refer to the measured net pressure across the panels, and GCp_{eq}^{cav} refer to the calculated cavity pressure. While comparisons can be made between the

measured GCp_{eq}^{ext} and the GCp values provided in ASCE 7-16 (2017), the focus of this study was to examine the net and pressure equalization factors of the roofing products. As such, the placement of the instrumentation is not optimized for a full and rigorous comparison to the design GCp values provided in ASCE 7-16 (2017).

This study presents statistical peak coefficients rather than absolute highest coefficients. This methodology is often used when reporting peak pressures from wind tunnel results (see Gavanski et al. (2016) for a recent, detailed discussion). To obtain these statistical peaks, the pressure time histories were divided into five segments. The peaks from each segment are extracted and fit with a Gumbel distribution using the Lieblein Best Linear Unibiased Estimate (BLUE) method (1974). The peak values reported herein are 78th percentile values from the Gumbel distribution. The PEF values reported are then calculated using these statistical peak external and net pressures.

For typical cladding elements on the roof, the suctions are the most critical for design. As such, the peak pressures discussed below refer to the peak suction (negative) pressure coefficients experienced by the two roofing systems.

3.4   Panel Results

3.4.1   Panel Selection

Unless otherwise stated, the results presented herein are for Panel 1 for the metal shingles or Panel 29 for the metal panels, at a wind direction of 180°. The wind direction was chosen

to reflect the highest external pressures for both panels, in a region of relatively high spatial gradients to obtain high net pressure values. Focusing on a single panel at a single wind direction was done in order to simplify the figures in the analysis and discussion. However, all panels were examined to ensure that any results (including pressure time histories, individual pressure tap statistics and correlation coefficients for a selection of panels representing different ASCE 7-16 (2017) roof zone locations) are representative.

3.4.2   Pressure Trends Based on Wind Direction

Figure 3.16 (top) presents peak GCp_{eq}^{ext}, GCp_{eq}^{net}, and GCp_{eq}^{cav} values for Panel 1 as a function of wind direction, along with the respective PEF values for the metal shingles. Here,

$$PEF = \frac{GCp_{eq}^{net}(\theta)}{GCp_{eq}^{ext}(\theta)} \qquad\qquad [3.35]$$

is obtained from the panel-averaged, peak values for each wind direction, θ. Similarly, Figure 3.16 (bottom) presents peak values for Panel 29, along with the respective PEF values for the metal panels. Note that Panel 1 and Panel 29 are at nearly symmetric locations across the ridge lines, yielding similar external pressures for wind directions of 0° and 180°, 170° and 190°, 160° and 200°, etc.
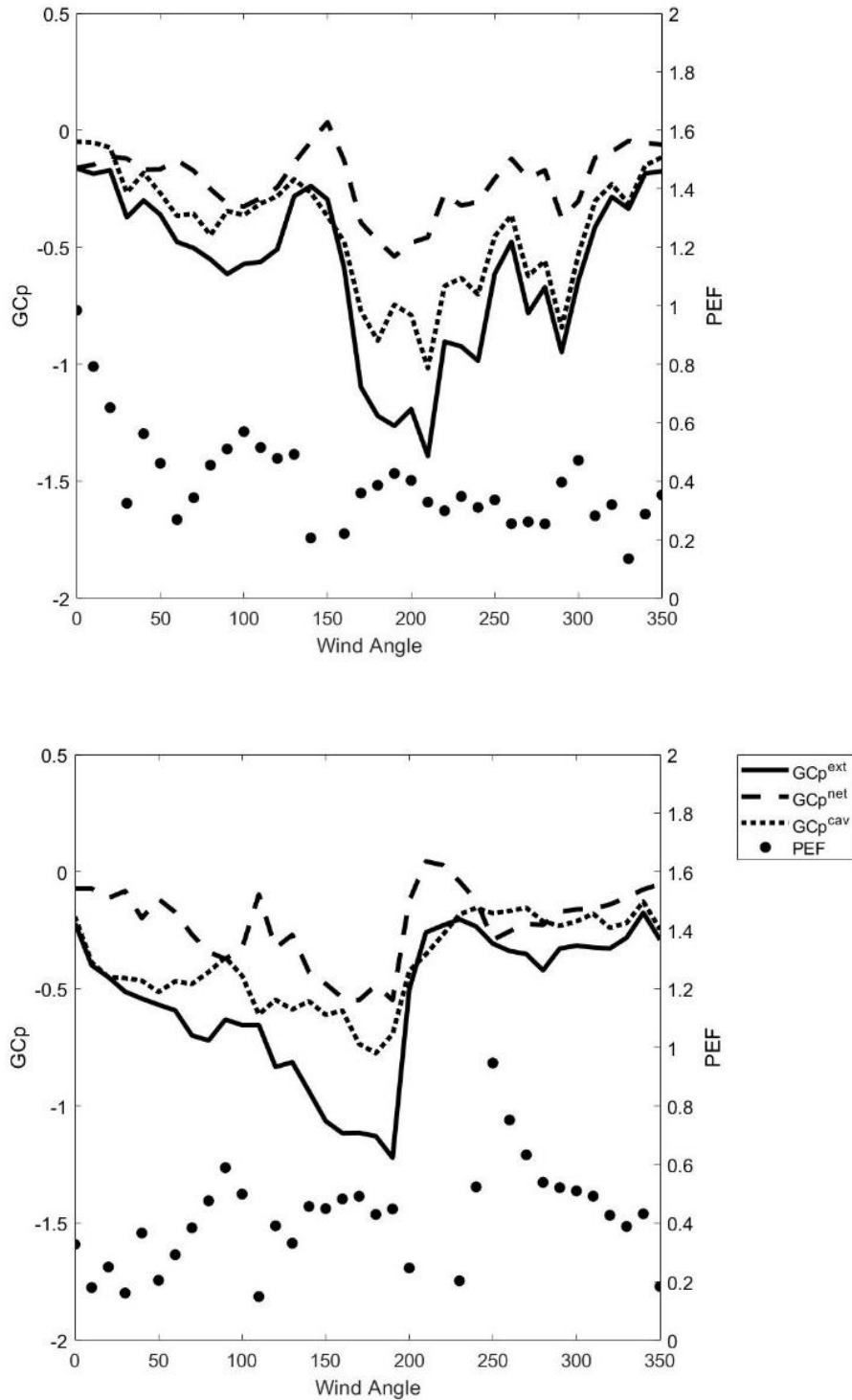
Figure 3.16: Panel-averaged GCp_{eq}^{ext}, GCp_{eq}^{net}, GCp_{eq}^{cav} values along with the corresponding PEF values as a function of wind angle for (top) the metal shingle at the Panel 1 location, and (bottom) the metal panel at the Panel 29 location.

Several observations can be made with respect to this figure. First, the largest magnitude external pressures occur for these panels when the wind directions are approximately normal to the gable end wall such that the panels are in the separation bubble (i.e., $\theta \cong 180°$), or in the corner vortex (i.e., $\theta \cong 30°$ from the normal). Peak GCp_{eq}^{ext} values are between -1.2 and -1.4 for these particular panels. Second, the largest magnitude net pressures are much smaller, with values of about -0.5. While, there is relatively less variation of GCp_{eq}^{net} when compared to GCp_{eq}^{ext}, the pattern with wind direction is similar such that the critical (i.e., worst case) wind directions are similar. This leads to mean PEF values for the critical net panel loads of about 0.4 to 0.5, although larger or smaller values tend to occur when both the net and external loads are small. When the external loads are that low, small changes result in huge changes to the PEF; however, these PEF values are not critical because the overall load is too small to govern design. Thus, the pressure equalization factor is relatively insensitive to wind direction and load level. Finally, in spite of the differences in the cavity and panel geometries, the cavity pressures for both cladding products are similar with peak values just less than half those of the external pressures. Such relative insensitivity to geometry tends to occur when the cavity pressures are relatively uniform across a single panel, as shown by Oh & Kopp (2014); a point which will be examined further below. The cavity pressure distributions (which includes leakage in between each panel) are also discussed in detail in a later section.

3.4.3   Pressure Trends Based on Location on Roof

Table 3.1 and Table 3.2 provide a summary of the largest of the peak values of GCp_{eq}^{ext}, considering all wind angles for all metal shingles and metal panels, respectively. The corresponding GCp_{eq}^{net} at the moment of peak GCp_{eq}^{ext} (and the resulting PEF value that is obtained by dividing the net pressure by the peak external net pressure) are included with this. Previous studies (e.g., Morrison & Cope, 2015) have also examined this point, finding the PEF value from the peak net pressure instead of the peak external pressure, but found little difference between the two methodologies; hence, its omission in this study. Table 3.1 and Table 3.2 also present a PEF based on the absolute worst values of GCp_{eq}^{net} and GCp_{eq}^{ext}, even if they do not occur at the same time or same wind direction. Since the critical wind directions indicate that the most highly loaded panels are in a region of separated flow, it would appear that the dominant loading mechanism is related to pressure equalization and not to local flow around the panel, unlike for the Peterka et al. (1997) model for asphalt shingles. Tables 1 and 2 also indicate that there is quite a large range of instantaneous PEF values across the roof, which raises the question of the practicality of obtaining a design value for PEF at a single instance in time. For example, Panel 2 and Panel 11 experience identical external pressures but the PEF values are different. As well, there is a wide range of PEF values for each of the traditional ASCE roof zones, showing again that PEF does not depend significantly on the load level (and consequently, the location on the roof), within the context of a relatively large range of variations. For example, Panels 58, 60, & 61 are all located in the same roof zone but experience different PEF values.

Table 3.1: Summary of largest GCp_{eq}^{net}, GCp_{eq}^{ext}, and PEF for the metal shingles across all wind directions.

Panel	Largest GCp_{eq}^{ext}	Corresponding GCp_{eq}^{net}	Critical θ	$\dfrac{GCp_{eq}^{net}}{Largest\ GCp_{eq}^{ext}}$ (PEF)	$\dfrac{Largest\ GCp_{eq}^{net}}{Largest\ GCp_{eq}^{ext}}$ (PEF)
1	-1.39	-0.46	210	0.33	0.39
2	-0.92	-0.39	90	0.42	0.47
7	-0.98	-0.48	240	0.50	0.56
8	-1.90	-0.79	170	0.42	0.42
11	-0.91	-0.53	240	0.57	0.59
13	-1.66	-1.10	170	0.66	0.66
15	-1.99	-0.82	230	0.41	0.47
22	-1.68	-0.62	230	0.37	0.42
25	-1.16	-0.32	220	0.28	0.53

Table 3.2: Summary of largest GCp_{eq}^{net}, GCp_{eq}^{ext}, and PEF for the metal panels across all wind directions.

Panel	Largest GCp_{eq}^{ext}	Corresponding GCp_{eq}^{net}	Critical θ	$\dfrac{GCp_{eq}^{net}}{Largest\ GCp_{eq}^{ext}}$ (PEF)	$\dfrac{Largest\ GCp_{eq}^{net}}{Largest\ GCp_{eq}^{ext}}$ (PEF)
29	-1.22	-0.55	190	0.45	0.45
31	-0.85	-0.31	170	0.36	0.53
36	-1.32	-0.96	40	0.73	0.73
38	-1.13	-0.67	260	0.59	0.59
42	-1.22	-0.73	190	0.60	0.60
52	-0.95	-0.46	10	0.49	0.55
54	-0.87	-0.49	260	0.56	0.63
58	-1.42	-0.28	110	0.20	0.37
60	-1.34	-0.50	110	0.38	0.45
61	-1.25	-0.55	110	0.44	0.47

3.4.4   Pressure Equalization Factors

Figure 3.17(a) presents the peak PEF values vs. GCp_{eq}^{ext} for all metal shingles across all wind angles, while Figure 3.17(b) presents the peak PEF values vs. GCp_{eq}^{ext} for all metal panels across all wind angles. Although there are currently design guidelines for pressure equalization factors for solar panels and roof pavers in some building codes, there is no prescribed method for determining design pressure equalization factors from experimental data. Examining Table 3.1 and Table 3.2, the highest PEF value for the metal panels is 0.66, and the highest PEF value for the metal panels is 0.73. These values encompass all pressure equalization factors at extreme external pressures. The similarity in PEF values between the two DMR systems is surprising given the differences between the two products and the geometry of the cavity space beneath the panels. The similarity suggests that the PEF for all air-permeable multilayer systems may be close enough in magnitude, that a single design value could be sufficient for both systems.
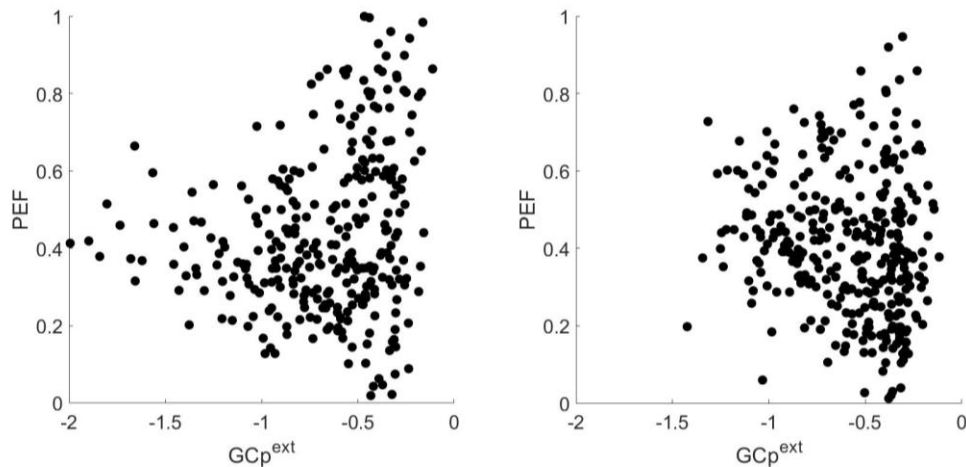
Figure 3.17: PEF values irrespective on wind direction or roof location vs. GCp_{eq}^{ext} for a) metal shingles and b) metal panels.

3.5 Mechanisms of Pressure Equalization

3.5.1   Overall Statistics

Figure 3.18 depicts contour plots of the mean external, cavity, and net pressure respectively, along with the edges of the panel and the location of the pressure taps. Linear interpolation is used in between the pressure taps to create the contour plot, but no extrapolation is performed between the pressure taps and the edge of the panel. The net pressure contour plot also indicates the approximate location of the neutral pressure line. This figure demonstrates that the mean cavity pressure distribution is more uniform than the external pressure or net pressure distribution. These contour plots also show the neutral pressure line can be present across a single panel. However, due to the complicated geometry of the cladding, the neutral pressure line is not as simple as expressed in Figure 1.8, which was for a one-dimensional situation. The contour plots also show that the external pressure gradients are much larger than the cavity pressure gradients.

3.5.2   Cavity Pressure Distribution Across A Panel

The cavity pressure plays an important role in the overall net load of the cladding, as discussed earlier. Figure 3.19 shows a segment of the cavity pressure time histories of the individual pressure taps for a single panel at a single wind direction. Examining this short section of time history, the cavity pressures are generally similar across the panel, although there are instantaneous variations.
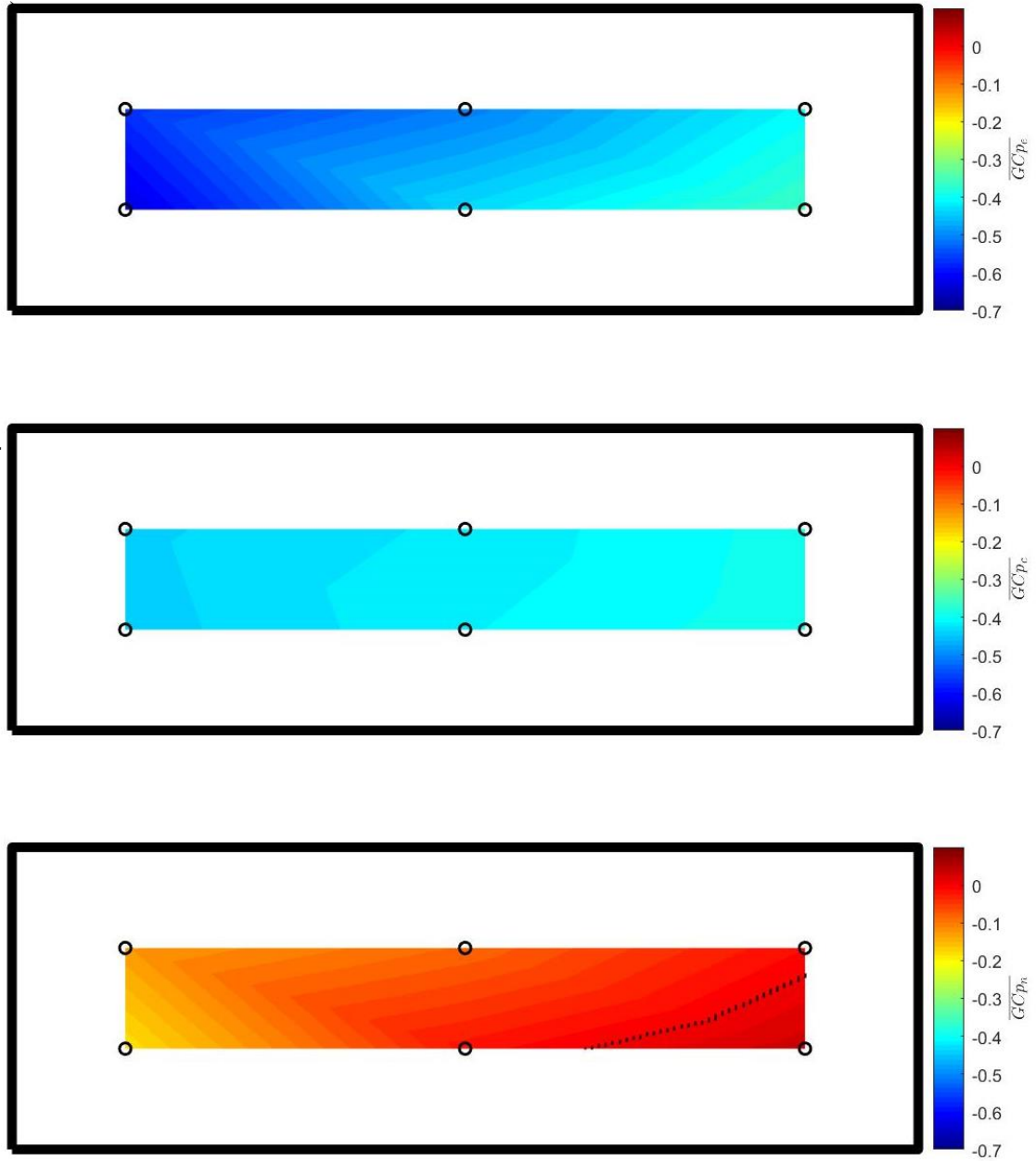
Figure 3.18: Contour plots showing the mean distribution of the (top) external pressure, (middle) cavity pressure, and (bottom) net pressure, respectively, across Panel 1 for a wind direction, $\theta = 180°$. The neutral pressure line is also shown on the net pressure graph.
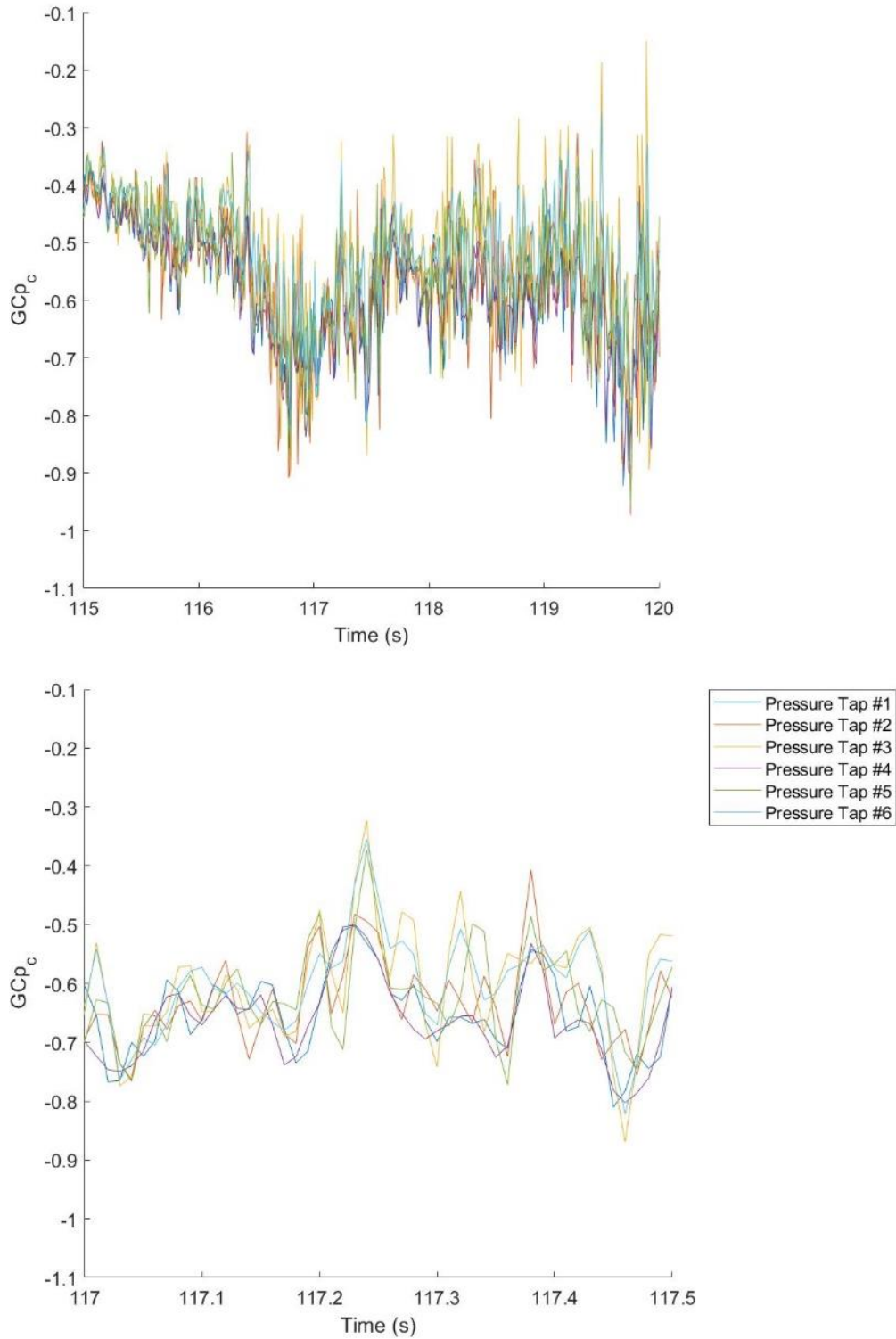
Figure 3.19: A (top) 5 sec segment, and a (bottom) 0.5 sec segment of the cavity pressure time history of individual pressure taps (Panel 1 for a wind direction, θ = 180°).

Figure 3.20 shows the cavity pressure variations from the same six pressure taps expressed as a histogram. This figure indicates that all pressure taps across this single panel have similar statistics, within measurement uncertainty, indicating that the cavity pressure time histories are largely similar.
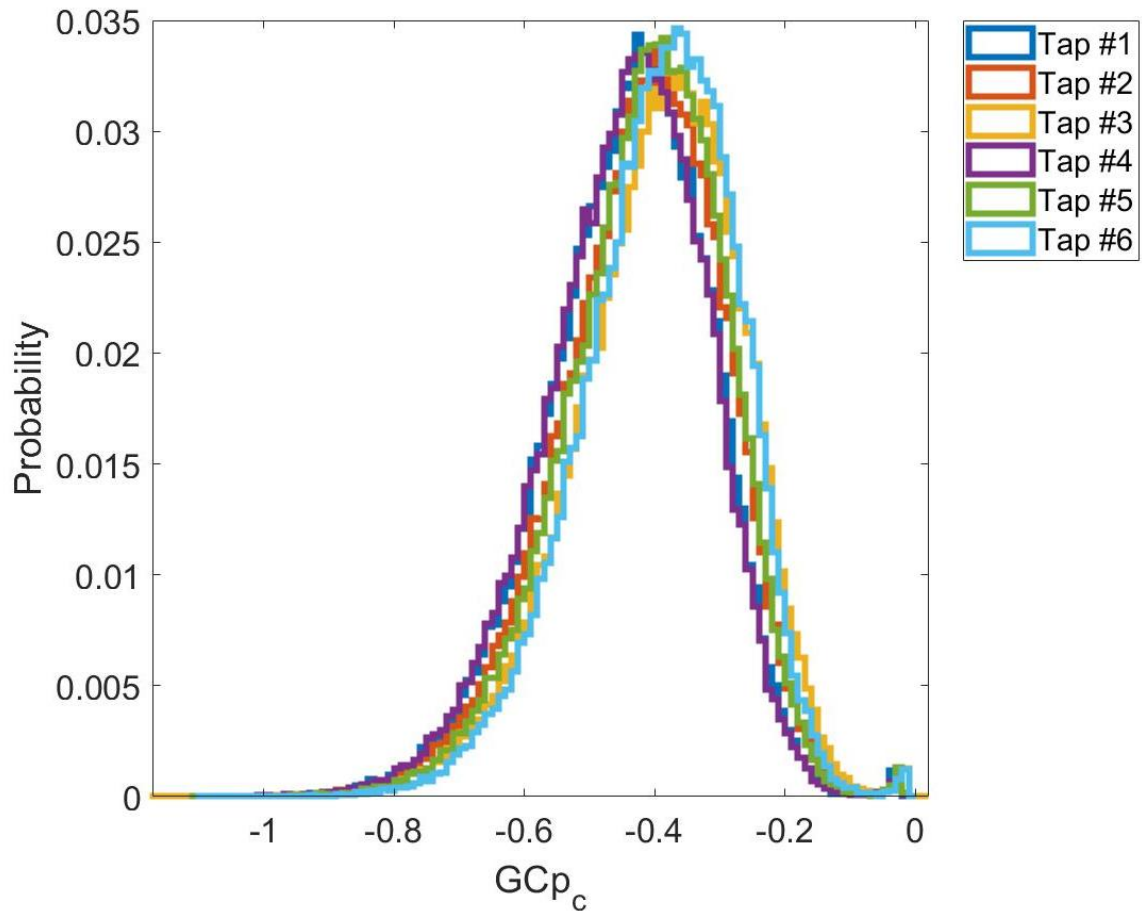
Figure 3.20: Histogram of all six cavity pressure taps (Panel 1 for a wind direction, $\theta = 180°$.).

Finally, to further examine the similarity in the cavity pressure across the pressure taps, the correlation coefficients were calculated as,

$$\rho(A, B) = \frac{cov(A, B)}{\sigma_A \sigma_B} \qquad [3.36]$$

Calculating the correlation coefficients between all six pressure taps results in the following 6x6 matrix,

$$\rho = \begin{bmatrix} 1.00 & 0.882 & 0.788 & 0.957 & 0.889 & 0.866 \\ \cdots & 1.00 & 0.767 & 0.891 & 0.907 & 0.839 \\ \cdots & \cdots & 1.00 & 0.833 & 0.798 & 0.949 \\ \cdots & \cdots & \cdots & 1.00 & 0.918 & 0.905 \\ \cdots & \cdots & \cdots & \cdots & 1.00 & 0.873 \\ \cdots & \cdots & \cdots & \cdots & \cdots & 1.00 \end{bmatrix}$$

The cavity pressure taps have a strong positive correlation, with no correlation less than 0.76 Overall, the correlations, along with the rest of the data presented in this section indicate that there are not substantial variations of the cavity pressure across one cladding element (panel). This indicates that the magnitude of the cavity pressure is a more important factor to reduce the overall net load across the cladding, and not a large gradient of the cavity pressures.

3.5.3   Cavity Pressure Distribution Across Multiple Panels

Although the two DMR systems have different cavity depths, both systems share cavities along the length of their panels. From the gable end of the roof to the hip ridge, the cavities run along the x direction of the roof. On the hip section of the roof, they run along the y direction of the roof. The ridges and the edges of the roof seal off each cavity, meaning that cavities do not run from one section of the roof to another.

The cavity pressure distributions across multiple panels that share a common cavity are examined. Figure 3.21 shows the time history for a small segment of the time histories of the cavity pressures along Panels 28 – 37. Figure 3.22 presents the mean values of the external pressure at each tap, and the panel-averaged external pressure, along with the mean values of the cavity pressure at each tap, and the panel-averaged cavity pressure, both as a function of position along the row of panels, normalized by the roof height.
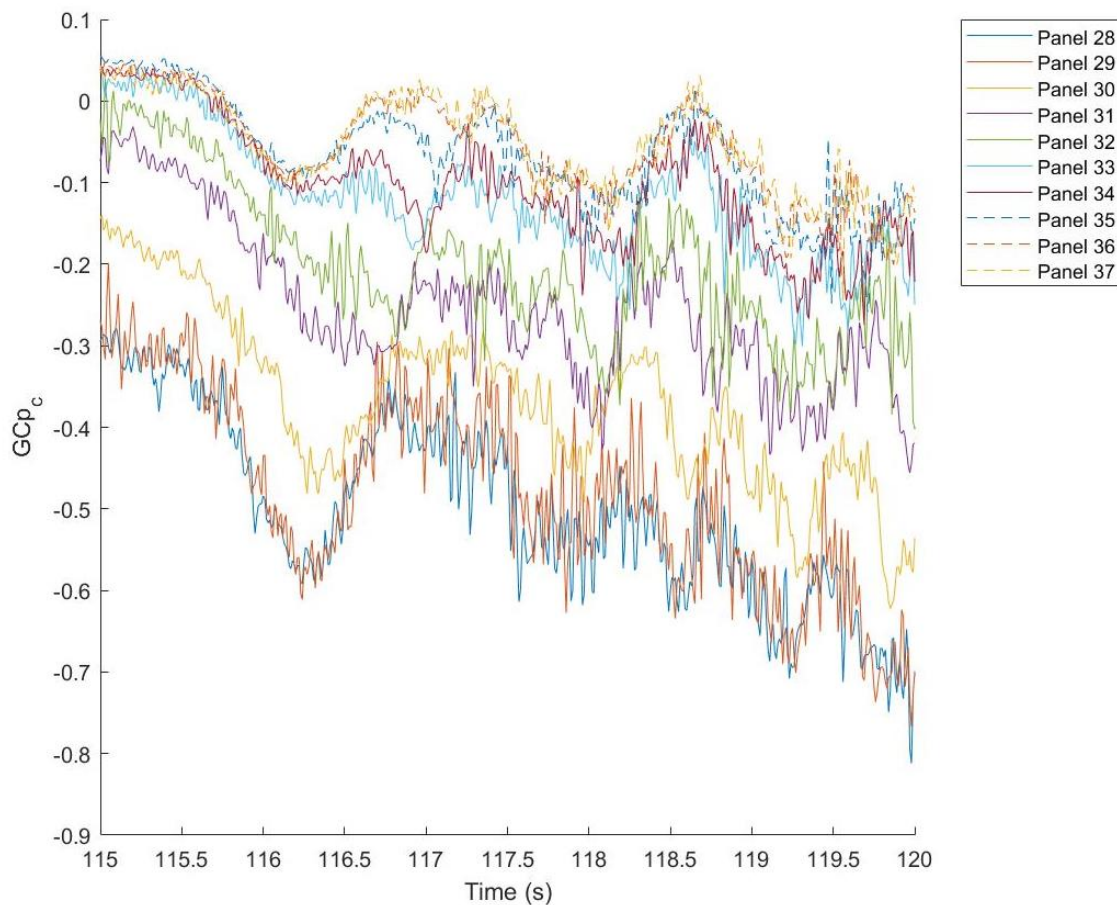
Figure 3.21: Cavity pressure time history of area-averaged panels. (Panels 28 – 37, for a wind direction, θ = 180°).
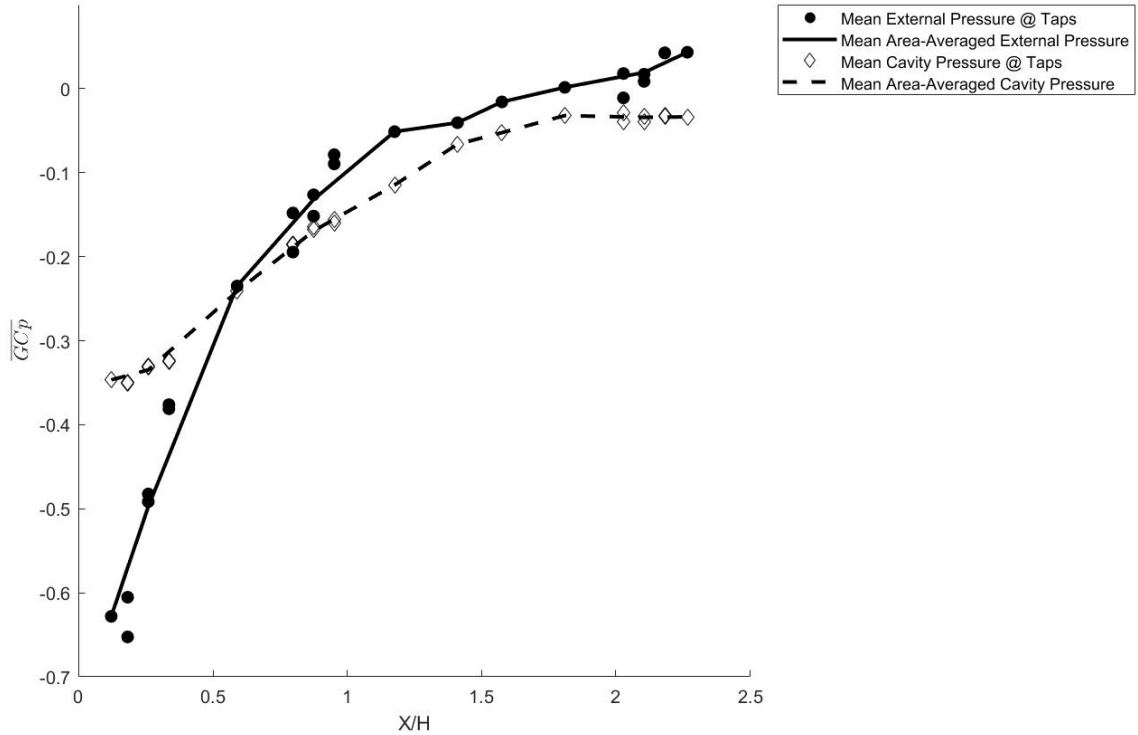
Figure 3.22: Mean pressure coefficients vs. distance along roof in X direction, normalized by roof height. (Panels 28 – 37, for a wind direction, $\theta = 180°$).

Several observations can be made regarding these figures. First, the overall trends of the time histories of cavity pressures are the same along the rows of panels, while the mean cavity pressures change monotonically along the rows of panels. For this wind direction and roof position, the mean external pressure distributions are typical of those for the separated-reattaching flow near a roof edge. Using the method of Wu et al. (2017), the mean reattachment point is estimated to be at X/H=0.7. The cavity pressure distributions are similar, but relatively smoothed such that the lowest suctions are reduced in magnitude, while further from the roof edge, they are larger in magnitude. Looking at both the external and cavity pressure, the mean neutral pressure line can be clearly seen at approximately

X/H=0.6. Figure 3.23 shows a graph of the net mean panel pressures overlaid with a diagram of the external flow, and the directions of flow between the panels.
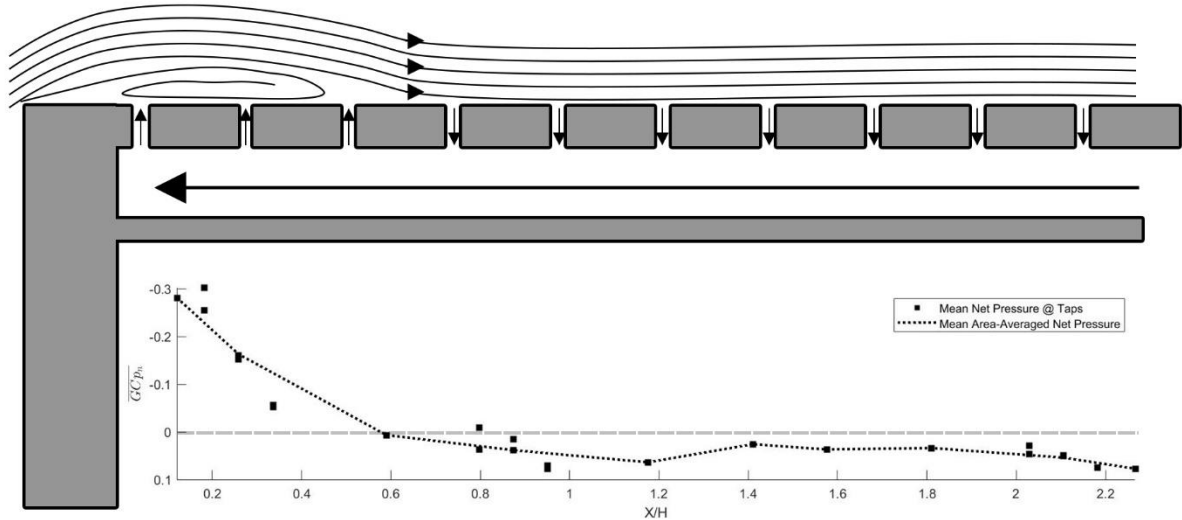
Figure 3.23: Net pressure vs. distance along roof in X direction, normalized by roof height, overlaid on a drawing showing the resulting cavity flows, along with the location of the neutral pressure line.

3.5.4   Inertial Effects on Net Pressures

As shown in Miller et al. (2017), external pressure differences are much more vital to the overall net load than the temporal variations for these types of cladding systems. However, there are two main pressure differences across the panel. There is the pressure difference along the length of the cavity in the long (or horizontal direction), ΔP_{E_H}, where the gaps for leakage are much larger and play a larger role on the cavity pressure. There is also the pressure difference across the width of the cavity (in the vertical direction), ΔP_{E_V}, with leakage on a much smaller scale due to the relatively tight connections between the

interlocking panels. Therefore, ΔP_{E_H} is used for the rest of the section to directly compare to the external pressure, cavity pressure, and net pressure.

Figure 3.24 shows a short segment of the time history of the external pressure difference at a peak, along with the corresponding area-averaged external pressure, cavity pressure, and net pressure. This figure offers numerous insights to how critical the resultant external pressure difference is in relation to the net load acting on air-permeable multilayer cladding. First, Figure 3.24 illustrates how the cavity pressure is directly related to the external pressure difference. The largest magnitude cavity pressure occurs at the same moment as the largest magnitude external pressure difference. However, variations in the cavity pressure are complicated due to the leakage and flow velocities, so this is not always evident by examining the time histories. The figure also shows that large net pressures occur when the external suction is large, and the cavity suction is small (which is expected). However, it also shows that this tends to occur as both the external pressure difference and cavity pressure are decreasing directly after a large external peak. It appears that peak external pressure differences lead to an increase in the cavity flow, which should be expected. This leads to a decrease in cavity suction, which, along with the increase in overall external suction, results in peak net loads. Figure 3.25 expands this idea of the inertial effects leading to a time lag between the external pressure difference and the net pressure by plotting the correlation of the peak external pressure difference and the net pressure coefficients, against the time lag for Panel 1 across all wind angles. Each time series was divided up into 5 segments, and the peak external pressure coefficient, along with a 0.01 second time history on each side of the peak was taken and used to create this figure. The figure shows that peak correlation between the two time histories occurs after

a time lag about 0.3 sec, indicating that there is an inertial effect leading to a time lag overall in these air-permeable multilayer systems. Since the entire duration of a peak in the external pressure is often less than 0.5 sec, this time lag is significant. Thus, the time lag, such as those in Figure 3.24 desynchronize the external and cavity pressures, leading to a reduction in the peak net loads on the system.
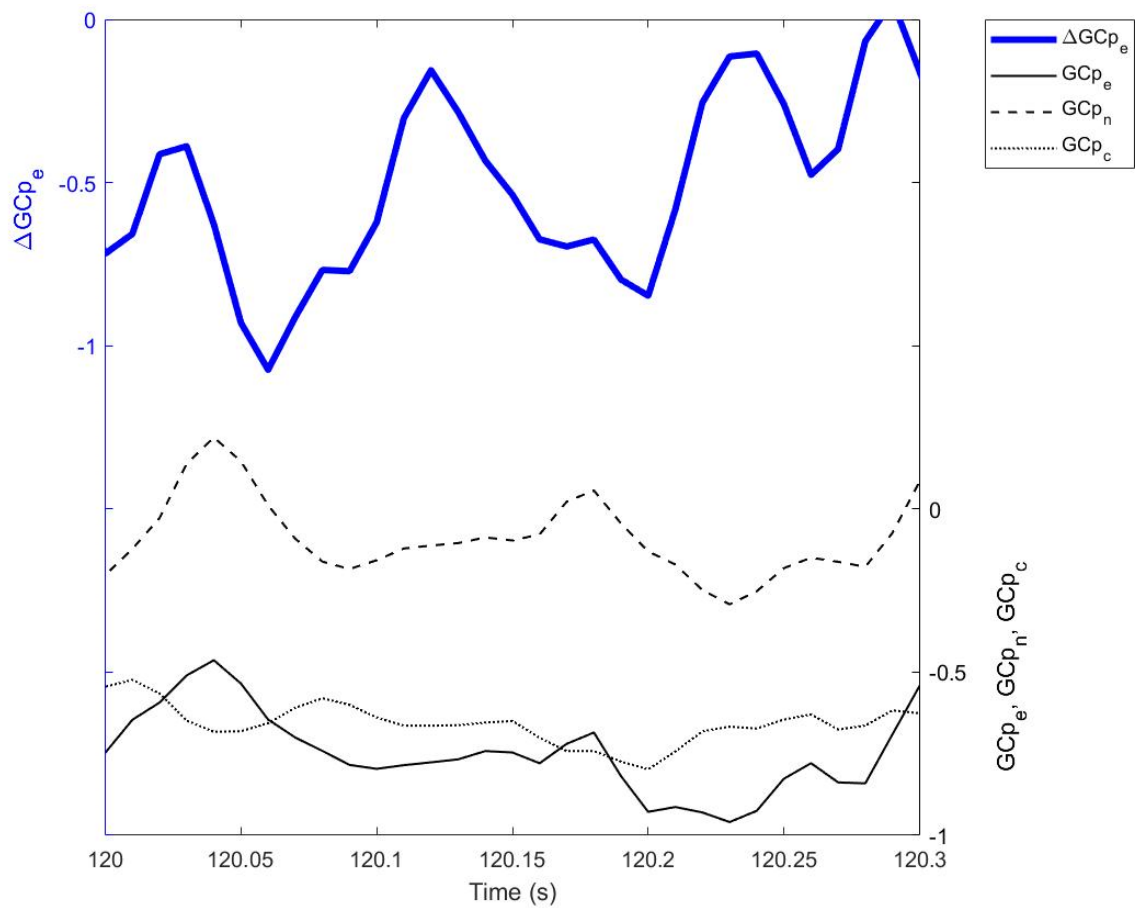
Figure 3.24: Time history graphs of the external pressure difference across the cladding, along with the corresponding area-averaged external pressure, cavity pressure, and net pressure. (Panel 1, 180°). (Although both y axes are equal, the zero line has been shifted for clarity.)
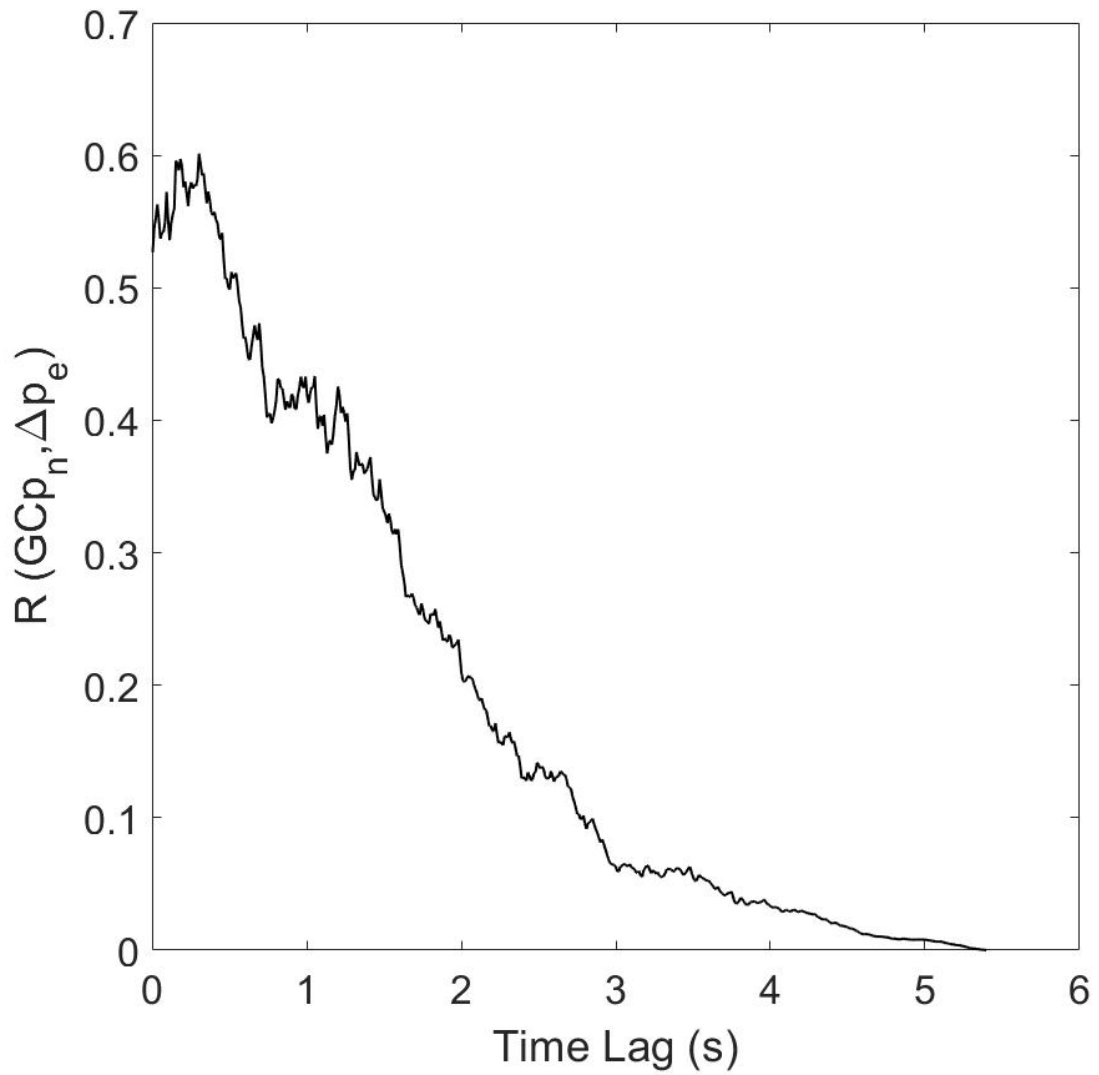
Figure 3.25: Correlation between the net pressure coefficient and the peak external pressure difference, plotted against the time lag for Panel 1 across all wind angles.

3.6   Summary

External and net wind pressures were measured on two discontinuous metal roofing systems installed on a full-scale steep slope residential building and tested in a full-scale wind field. The results show that the highest loaded panel for both systems experienced approximately 70% of the highest external pressures on the panels. Although the systems have different panel sizes, assembly methods, air pathways, and cavity geometries, they result in similar PEF values. This is due to both systems having small openings into the cavity and relatively large cavity volumes, which leads to relatively uniform pressure along the cavity (compared to the external pressure), resulting in similar PEF values. These PEF values were also shown to be unaffected by wind directions as well as load level. Consequently, the location of the critically loaded panel occurs near the location of the highest external pressures. This suggests that the pressure zones in design standards do not need to be altered for this type of cladding system. However, the magnitude of the pressures, together with the presence of a neutral pressure line, lead to loads on air-permeable multilayer cladding reducing faster with tributary area when compared to single layer systems, as pointed out by Oh & Kopp (2014). This indicates that connecting panels structurally has the significant benefit of greatly reduced design pressure coefficients since external pressures drop exponentially with area.

In terms of the aerodynamic mechanisms, the results indicate that the dominant loading mechanism for discontinuous metal roofing is related to pressure equalization and not to local flow around the panel. This contrasts with the model for asphalt shingles developed by Peterka et al. (1997) in spite of the similar external shapes of asphalt shingles and the

current roof cladding systems. The highest loads on the Peterka et al. (1997) model would occur when the near-surface wind speeds are highest, which is following reattachment. However, the highest measured net loads occur in the region of highest external pressure, which is near the roof edge in a region of separated flow. The role of the external pressure gradient, which drives the flow in the cavity, also plays a significant role in the pressure equalization.

The current results indicate that there is a time lag between the peak external gradient and the net pressure because of the flow inertia. This means that the inertial term in the unsteady Bernoulli equation applied to the cavity flow plays a role in reducing the net loads. Since the maximum flow rate leads to maximum pressure drop across the cladding later, the delay caused by the fluid inertia de-synchronizes the peak external and cavity pressures, reducing the peak net loads. Variability in the inertial term undoubtedly plays a role in variability of PEF values such that statistical approaches for design values, not unlike those for external pressures are required.

4   A Unified Approach to the Pressure Equalization Factor

4.1   Objectives

Chapter 1 shows that over the past twenty years, many studies have been done on pressure equalization. However, there is no current consensus on what equations or methods should be used to calculate the PEF of air-permeable multilayer cladding; or whether different air-permeable multilayer cladding should use the same pressure equalization factors. Chapter 2 demonstrates that the design PEF values for some air-permeable multilayer cladding systems were unconservative, due to a lack of spatial gradients in the standardized testing. It also demonstrated the challenges of developing a standardized test using airboxes due to a lack of clarity of what type of spatial gradients are appropriate for design values. Since Miller et al. (2017) has been published, ASTM D3679-13 (2013) has been updated to require a PEF value of 0.50 for vinyl siding (ASTM D3679, 2017). However, this value does not appear to be well aligned with the data obtained from multiple different studies on the pressure equalization on vinyl siding (Cope et al., 2012, Moravej et al., 2016, Miller et al., 2017). Chapter 3 shows that air-permeable multilayer cladding systems with significantly differing geometries (such as the G/H ratio) still result in similar PEF values. This holds for systems having small openings into the cavity with relatively large cavity volumes, which leads to relatively uniform pressure along the cavity. It also shows that the PEF at design-level wind loads is relatively unaffected by load level, and wind direction. Finally, it demonstrated that a there is a time lag between the peak external and cavity pressures, caused by the fluid inertia of the system. This inertial term desynchronizes the peak external and cavity pressures, reducing the peak net loads.

All of this previous work indicates that a unified approach for determining the pressure equalization factor may be more practical and appropriate for all air-permeable multilayer systems that have small openings and relatively large cavity volumes instead of having a more modified test standard. To accomplish this, an appropriate statistical method for calculating pressure equalization will be determined by examining all of the methods used previously and determining which approach would be the best for determining design values. Following that, the PEF values from the previous studies done on different building products will be extracted and examined. Finally, based on these values, and the factors that govern them, a design guideline for determining the PEF on air-permeable multilayer systems will be determined (along with recommendations for implementing these guidelines into current building codes).

4.2   Expressions of Pressure Equalization Factor

Chapter 1 of this thesis defined PEF as "the proportion of external load acting on the cladding". Chapter 2 used the envelope method developed by IBHS in order to allow for a direct comparison with the wind tunnel study on vinyl siding performed by Cope et al. (2012) to determine the validity of the multichamber airbox testing. Chapter 3 used multiple different methods to calculate pressure equalization, and directly compared them in Table 3.1 and Table 3.2. However, there is no definitive method used to calculate the pressure equalization factor. This section explores the most common methods of calculating PEF, and then compares them to determine which is the most appropriate for creating design values.

As shown in Chapter 1, the external pressures that are applied to air-permeable multilayer cladding are given as pressure coefficients, which are typically defined relative to the mean wind speed at the roof height to remove the influence of the building height on the magnitudes of the minimum and maximum pressure coefficients. These pressure coefficients are a function of the location on the building, time, and the wind direction for a given building shape (x, t, θ).

$$C_{pe} = \frac{p_e - p_0}{\frac{1}{2}\rho U_H^2}$$
[4.1]

The cavity pressure coefficient can be defined in a similar manner:

$$C_{pc} = \frac{p_c - p_0}{\frac{1}{2}\rho U_H^2}$$
[4.2]

From this, the net pressure coefficient can be expressed as:

$$C_{pn} = C_{pe} - C_{pc}$$
[4.3]

Or, substituting equation 4.1 & 4.2 into equation 4.3:

$$C_{pn} = \frac{p_e - p_c}{\frac{1}{2}\rho U_H^2}$$
[4.4]

Keeping the simple definition of pressure equalization factor from Chapter 1 - "the proportion of external load acting on the cladding" - the pressure equalization factor can be defined as,

$$PEF = C_{pn}/C_{pe} \tag{4.5}$$

which is the ratio of the net pressure coefficient to the external pressure coefficient. Alternatively, substituting in equation 4.1 and 4.4 into equation 4.5, the PEF can be written as:

$$PEF = \frac{p_e - p_c}{p_e - p_0} \tag{4.6}$$

This demonstrates that it does not matter whether the PEF value is calculated from pressures, or pressure coefficients. These equations also assume that the inner surface of the cavity is sealed. Because the pressure coefficients in equation 4.5 are a function of the location on the building, time, and the wind direction for a given building shape, the PEF may be a function of the location on the cladding element, time, and the wind direction (x, t, θ) for a given cladding system.

All of the pressure coefficients can be written as a peak value across all locations, time, and wind directions by enveloping the range of values across all of the defined functions of the pressure coefficient, or:

$$\left\{ \widehat{C_{pn}} \left| \begin{matrix} x \\ t \\ \theta \end{matrix} \in \mathbb{R} \right. \right\} \tag{4.7}$$

This statement can be rearranged to define the peak value for a particular position,

$$\left\{ \widehat{C_{pn}}(x) \left| \begin{matrix} t \\ \theta \end{matrix} \in \mathbb{R} \right. \right\} \tag{4.8}$$

or the peak value at a particular position and wind direction,

$$\{\widehat{C_{pn}}\,(x,\theta)\,\big|\,t \in \mathbb{R}\} \qquad\qquad [4.9]$$

These statements also apply for peak external pressure coefficients and peak cavity pressure coefficients. These enveloped values can then be used to define the PEF as a peak value at a particular position, or a particular position and wind direction.

$$PEF_{Non-S}(x) = \frac{\left\{\widehat{C_{pn}}\,(x)\,\Big|\begin{matrix} t \\ \theta \end{matrix} \in \mathbb{R}\right\}}{\left\{\widehat{C_{pe}}\,(x)\,\Big|\begin{matrix} t \\ \theta \end{matrix} \in \mathbb{R}\right\}} \qquad\qquad [4.10]$$

$$PEF_{Non-S}(x,\theta) = \frac{\{\widehat{C_{pn}}\,(x,\theta)\,|\,t \in \mathbb{R}\}}{\{\widehat{C_{pe}}\,(x,\theta)\,|\,t \in \mathbb{R}\}} \qquad\qquad [4.11]$$

Both of these expressions for PEF are non-simultaneous. The expressions for PEF can be written as a simultaneous function for a particular moment in time and location :

$$PEF_{Sim}(x,t) = \frac{\{C_{pn}\,(x,t)\,|\,\theta \in \mathbb{R}\}}{\{C_{pe}\,(x,t)\,|\,\theta \in \mathbb{R}\}} \qquad\qquad [4.12]$$

Cope et al. (2012) proposed this instantaneous pressure equalization coefficient, as written above in equation 4.12, Thus $PEF_{Sim}(x,t)$ represents the time history of PEF values enveloped over all wind directions. They are typically plotted as scatter plots of the PEF vs. the external pressure coefficient. Instantaneous PEF scatter plots have a high dispersion at low external pressure coefficients. This makes it unclear which PEF value to use for design, since the maximum value typically occurs for low magnitude external pressures. To combat this, Cope et al. (2012) also proposed an enveloped simultaneous pressure equalization value, as the ratio of the net pressure normalized by the peak external pressure, across all locations and wind directions, plotted as a scatter plot similar to Figure 2.14.

$$PEF_{Sim}(t) = \frac{\left\{ C_{pn}(t) \left|\begin{matrix} x \\ \theta \end{matrix}\right. \in \mathbb{R} \right\}}{\left\{ \widehat{C_{pe}}(t) \left|\begin{matrix} x \\ \theta \end{matrix}\right. \in \mathbb{R} \right\}}$$ [4.13]

The peak value can then be taken from equation 4.13 by examining the scatter plot and taking the PEF value at the peak external pressure, similar to the study shown in Chapter 2.

Geurts (2000) proposed a non-simultaneous pressure equalization coefficient, as the ratio of the largest magnitude value of the peak net pressure at any point in time over the largest magnitude value of the peak external pressure at any point in time, across all wind directions.

$$\widehat{PEF_{Non-S}} = \frac{\left\{ \widehat{C_{pn}} \left|\begin{matrix} x \\ t \\ \theta \end{matrix}\right. \in \mathbb{R} \right\}}{\left\{ \widehat{C_{pe}} \left|\begin{matrix} x \\ t \\ \theta \end{matrix}\right. \in \mathbb{R} \right\}}$$ [4.14]

ASCE 7-16 (2017) performs a similar enveloping method for their external pressure, by using:

$$\left\{ \widehat{C_{pe}} \left|\begin{matrix} x \\ t \\ \theta \end{matrix}\right. \in \mathbb{R} \right\}$$ [4.15]

To remain consistent with current enveloping methods, it is recommended to envelope the net pressure in a similar fashion, as previously shown in equation 4.7. Therefore, the most appropriate manner to describe the design pressure equalization factor is the pressure equalization coefficient method (or used by Geurts, 2000), and restated as:

$$PEF_{ASCE\ 7} = PEF_{Non-S} = \frac{\left\{ \widehat{C_{pn}} \left| \begin{array}{c} x \\ t \in \mathbb{R} \\ \theta \end{array} \right. \right\}}{\left\{ \widehat{C_{pe}} \left| \begin{array}{c} x \\ t \in \mathbb{R} \\ \theta \end{array} \right. \right\}} \qquad [4.16]$$

This method is what is already currently used in ASCE 7-16 (2017) for determining the pressure equalization in solar panels, which is discussed further in Section 4.4.4. Enveloping the worst-case value for each effective area is a common method of obtaining design wind loads on components and cladding (Stathopoulos et al., 2000). The downside of this approach is that design loads are a step removed from the equations and numerical models used to calculate cavity pressures in air-permeable multilayer systems.

4.3 Pressure Equalization Studies

4.3.1 Data Selection & Reduction

This section contains a review of studies that have published values for the PEF on air-permeable multilayer cladding using equation 4.16 (Geurts, 2000). For studies that originally used equation 4.13 (Cope et al., 2012), but have published values for the peak net pressure and peak external pressures, these pressure values are then used to calculate the peak PEF using equation 4.16. No other methods are commonly used to calculate the PEF in air-permeable multilayer systems. The effective area of each PEF value is also noted, along with other factors that are significant for each specific air-permeable

multilayer system (e.g., whether the system is lined with foam insulation, which is only found on vinyl siding). Their impact on the PEF is discussed further in Section 4.4.

Several statistical methods to define the peak pressure coefficient (GCp) for use in design standards (e.g., ASCE 7-16) have been documented in the literature. Since the variability of pressure coefficients and PEF values are significant, statistical approaches are required for design values. First, each GCp at an individual pressure tap is weighted based on the tributary area of its pressure tap within the effective wind area, creating an area-averaged time history for that effective wind area. In the single worst peak method (as documented in Stathopoulos (1979)), the peak area-averaged pressure coefficient is not subject to any sort of statistical analysis and is defined as the extreme value over the entire sampling period. This single worst peak can be obtained multiple times from a long single sampling period by dividing the time histories into multiple time series. Morrison & Kopp (2018) recommended that the sampling period is at least divided into 4 segments. A Gumbel-fitting method can then be used to define a statistical peak GCp at a certain percentile of the probability of exceedance using the Lieblein BLUE method (1974), or another method. This methodology is often used when reporting peak pressures from wind tunnel results (see Gavanski et al. (2016) for a recent, detailed discussion). Peak values tend to be defined using 78th percentile values, as specified in ISO (2009). Although there is currently no consensus on a standard for defining the peak GCp, this method has been shown to provide an appropriate statistical value of the peak GCp (Gavanski et al., 2016). For determining the peak external GCp in each zone, multiple effective wind areas are considered for each ASCE 7-16 zone, enveloping all locations in that zone, time, and wind direction.

However, as noted in Chapter 3, the PEF at design-level wind loads is relatively unaffected by load level and wind direction. Therefore, enveloping the peak net GCp should follow the same guidelines as enveloping the peak external GCp, but the entire roof or wall should be considered as one zone. To summarize, the peak net GCp will be calculated as a statistical peak at a 78th percentile value, as detailed in Gavasnki et al. (2016) and applied by Kopp & Morrison (2018) at multiple locations across the roof or wall, with varying effective wind areas, enveloping all locations, time, and wind direction. For GCp values with the same effective wind areas, only those with the highest net GCp will be considered as a form of further data reduction. The peak external GCp for each effective wind area with the highest net GCp will be calculated in the same method, and then used in equation 4.16 to calculate the PEF for that effective wind area.

As an example, the data from Table 3.1 and Table 3.2 from the discontinuous metal roofing study are presented again below in Table 4.1 and Table 4.2, however, the peak GCp_n is shown rather than the corresponding GCp_n at the peak GCp_e. As discussed in Section 3.3.5, the pressure time histories obtained for each pressure sensor were converted into GCp_{eq} values that are comparable to GCp values provided by ASCE 7-16 (2017), and then area-averaged across the panel. The pressure time histories were then divided into five segments. The peaks from each segment are extracted and fit with a Gumbel distribution using the Lieblein BLUE method (1974) with 78th percentile values for the duration of the time history. The PEF values reported are then calculated using these statistical peak external and net pressures using equation 4.16 (enveloped for all locations on the cladding element, time, and the wind direction (x, t, θ)). From this, we can get the design PEF values for a

single panel of these two different DMR products by obtaining the PEF value at the highest

GCp_n (since all values in Table 4.1 and Table 4.2 have the same effective wind area).

Table 4.1: Summary of largest GCp_{eq}^{net}, GCp_{eq}^{ext}, and PEF for the metal shingles across all wind directions, highlighting the peak net pressure and corresponding PEF.

Panel	Largest GCp_{eq}^{ext}	Largest GCp_{eq}^{net}	$\dfrac{\left\{\widehat{C_{pn}}\Big\|_{\theta}^{x} t \in \mathbb{R}\right\}}{\left\{\widehat{C_{pe}}\Big\|_{\theta}^{x} t \in \mathbb{R}\right\}}$ (Equation 4.16)
1	-1.39	-0.54	0.39
2	-0.92	-0.43	0.47
7	-0.98	-0.55	0.56
8	-1.90	-0.79	0.42
11	-0.91	-0.53	0.59
13	-1.66	-1.10	0.66
15	-1.99	-0.93	0.47
22	-1.68	-0.71	0.42
25	-1.16	-0.61	0.53

Table 4.2: Summary of largest GCp_{eq}^{net}, GCp_{eq}^{ext}, and PEF for the metal panels across all wind directions, highlighting the peak net pressure and corresponding PEF.

Panel	Largest GCp_{eq}^{ext}	Largest GCp_{eq}^{net}	$\dfrac{\left\{\widehat{C_{pn}}\Big\|_{\theta}^{x} t \in \mathbb{R}\right\}}{\left\{\widehat{C_{pe}}\Big\|_{\theta}^{x} t \in \mathbb{R}\right\}}$ (Equation 4.16)
29	-1.22	-0.55	0.45
31	-0.85	-0.45	0.53
36	-1.32	-0.96	0.73
38	-1.13	-0.67	0.59
42	-1.22	-0.73	0.60
52	-0.95	-0.53	0.55
54	-0.87	-0.55	0.63
58	-1.42	-0.53	0.37
60	-1.34	-0.60	0.45
61	-1.25	-0.59	0.47

Unfortunately, due to a lack of access to pressure data in some studies, the data reduction method detailed above is not always possible. In those cases, the published values for PEF will be used, and the statistical methods used in their analysis will be noted. Although this is not ideal, gathering this data will give us a preliminary idea whether the concept of a unified approach to the pressure equalization factor is possible.

4.3.2   Discontinuous Metal Roofing

Table 4.3 presents area-averaged peak external pressure coefficients, peak net pressure coefficients, and peak enveloped PEF values across rows of panels (see Figure 3.14) from the discontinuous metal roofing data from Chapter 3. Since the pressure tap distribution is very sparse across certain sections of the roof, only certain grouping of panels along the lengths of certain cavities were considered for area-averaging. The data presented in this table are statistical peaks using the data reduction method presented in Section 4.3.1. Table 4.4 presents a summary of the peak PEF values along with the effective wind area on two different discontinuous metal roofing products taken from Table 4.1, Table 4.2, and Table 4.3.

Table 4.3: Summary of largest area-averaged GCp_{eq}^{net}, GCp_{eq}^{ext}, and PEF for metal shingles and metal panels across all wind directions.

DMR Type	Panels	Effective Wind Area (m^2)	Largest GCp_{eq}^{ext}	Largest GCp_{eq}^{net}	$\dfrac{\left\{\widehat{C_{pn}}\Big\|_{\theta}^{x}\,t\in\mathbb{R}\right\}}{\left\{\widehat{C_{pe}}\Big\|_{\theta}^{x}\,t\in\mathbb{R}\right\}}$ (Equation 4.16)
Shingles	22:23	0.558	-1.69	-1.00	0.59
	24:25:26	0.837	-1.14	-0.67	0.59
	22:23:24:25:26:27	2.137	-1.12	-0.70	0.62
Panels	28 - 37	3.967	-0.68	-0.27	0.40
	41 - 53	3.340	-0.78	-0.18	0.23
	57 - 63	2.832	-1.00	-0.28	0.28

Table 4.4: Summary of PEF values along with the effective wind area taken from studies done on different discontinuous metal roofing products.

Author	Year	Title	DMR Type	$\dfrac{\left\{\widehat{C_{pn}}\Big\|_{\theta}^{x}\,t\in\mathbb{R}\right\}}{\left\{\widehat{C_{pe}}\Big\|_{\theta}^{x}\,t\in\mathbb{R}\right\}}$ (Equation 4.16)	Effective Wind Area (m^2)
Miller	2020	Chapter 3 (current study)	Shingles	0.66	0.279
				0.59	0.558
				0.59	0.837
				0.62	2.137
			Panels	0.73	0.379
				0.28	2.832
				0.23	3.340
				0.40	3.967

4.3.3   Vinyl Siding

Morrison & Cope (2015) (and Cope et al. (2012)) tested wind loads on a full-scale multilayered wall assembly in the IBHS test chamber in order to compare to the PEF value given in ASTM D3679-13. Table 4.5 presents the tabular values of the pressure equalization factors along with the effective wind area from this study. Both vinyl siding (Wall 1) and foam-backed vinyl siding (Wall 6) were tested (the two most common types of products used in residential construction). This foam backing is used to provide extra insulation for the building envelope. The data presented in Table 4.5 were taken from Table 2 of Morrison & Cope (2015), using the data reduction method presented in Section 4.3.1.

As may be expected, there is a clear reduction in the PEF as the effective wind area increases. There is also a significant reduction of the peak PEF values of foam-backed vinyl siding, compared to regular vinyl siding. This is due to the foam insulation significantly reducing the cavity height, while keeping the same gap width (therefore, increasing the G/H ratio and reducing the PEF). The effect of G/H ratio on the PEF, and the design recommendations surrounding this factor are discussed further in Section 4.4.2.

Table 4.5: Summary of PEF values along with the effective wind area taken from studies done on vinyl siding and foam-backed vinyl siding.

Author	Year	Title	$\dfrac{\left\{\widehat{C_{pn}}\left\lvert\begin{smallmatrix}x\\t\in\mathbb{R}\\\theta\end{smallmatrix}\right.\right\}}{\left\{\widehat{C_{pe}}\left\lvert\begin{smallmatrix}x\\t\in\mathbb{R}\\\theta\end{smallmatrix}\right.\right\}}$ (Equation 4.16)	Effective Wind Area	Foam-Backed?
Morrison & Cope	2015	Wind Performance and Evaluation Methods of Multi-Layered Wall Assemblies	0.88	0.732	
			0.73	1.098	
			0.88	1.440	
			0.81	1.464	
			0.61	2.160	
			0.55	2.880	
			0.56	3.240	
			0.58	4.320	
			0.58	5.760	
			0.53	0.732	✔
			0.48	1.098	✔
			0.51	1.440	✔
			0.53	1.464	✔
			0.42	2.160	✔
			0.37	2.880	✔
			0.37	3.240	✔
			0.33	4.320	✔
			0.34	5.760	✔

4.3.4   Roof Pavers

Mooneghi et al. (2014, 2015) performed a 1:2 scale wind tunnel study at the Wall of Wind facility at Florida International University. Table 4.6 presents the tabular values of the pressure equalization factors along with the effective wind area from this study. Peak external and net GCp values are presented as statistical peaks by using the method outlined in Sadek and Simiu (2002). This process is very similar to the data reduction process outlined in Section 4.3.1 but with some minor differences. Instead of obtaining multiple peaks by dividing time histories into multiple segments, the Sadek and Simiu (2002) method uses the probability distribution of the time series to consider the entire effect of the entire time series. A Gumbel distribution is then applied at an 85th percentile to obtain the peak pressure coefficients. Since this method and the data reduction method used in Section 4.3.1 both use Gumbel distributions at similar percentiles, the values from this study will be taken as statistically comparable for the purposes of this study. The data presented in Table 4.6 was taken from Table 3 of Mooneghi et al. (2015).

All of the data given in Mooneghi et al. (2015) is taken from a single critical paver (Figure 13 of Mooneghi et al. (2015) shows the reduction of the peak net load over multiple panels, it does not show the reduction of the external net load over multiple panels). Therefore, the peak PEF values can not be examined over larger effective wind areas. Another limitation of this study is that due to the building scale, the paver area to roof area is relatively large, which may affect the results. However, this study does examine how the peak PEF varies as a function of different G/H ratios, and how the parapet height can affect the peak PEF values. Both of these concepts are examined further in Section 4.4.

Table 4.6: Summary of PEF values along with the effective wind area taken from studies done on roof pavers.

Author	Year	Title	$\dfrac{\left\{\widehat{C_{pn}}\left\vert\begin{matrix}x\\t\in\mathbb{R}\\\theta\end{matrix}\right.\right\}}{\left\{\widehat{C_{pe}}\left\vert\begin{matrix}x\\t\in\mathbb{R}\\\theta\end{matrix}\right.\right\}}$ (Equation 4.16)	Effective Wind Area	G/H	h_p/H
Mooneghi et al.	2015	Towards guidelines for design of loose-laid pavers for wind uplift	0.58	0.093	0.25	0.05
			0.57	0.093	0.25	0.067
			0.55	0.093	0.25	0.1
			0.74	0.093	0.083	0.033
			0.75	0.093	0.083	0.05
			0.69	0.093	0.083	0.1
			0.64	0.093	0.083	0.15
			0.82	0.093	0.028	0
			0.83	0.093	0.028	0.05
			0.81	0.093	0.028	0.1

4.3.5　Tile Roofing

Smith & Morrison (2019) tested wind loads on a full-scale building with a tile roof in the IBHS test chamber. Both North American and Australian roofing tile systems were tested. For both types of roofing systems, the effect of tile profile (flat vs. s-shape) were tested. Additionally, the effect of tile attachment and battens were examined for the North American system and the effect of sarking (impermeable water membrane beneath the sheathing) was investigated for the Australian system. Importantly, the North American system was installed with no gutters around the edges of the buildings, this results in flow impingement on the eave tiles directly (rather than the gutters), increasing the PEF dramatically on the corner and edge tiles. Therefore, for this analysis, the edge and corner tiles of the North American system shall be treated separately from the tiles in the middle

of the roof. The Australian system was installed with gutters on the roof, removing the

effects from an exposed edge. Using data provided directly from IBHS, Table 4.7 presents

peak PEF results from the North American system, using the data reduction method

presented in Section 4.3.1, and Table 4.8 presents peak PEF results from the Australian

system, using the data reduction method presented in Section 4.3.1. No area-averaging

across the tile roofs was possible due to the sparsity of pressure taps across the roof.

Peak PEF values cannot be examined over larger effective wind areas due to the lack of

area-averaged values across multiple panels. Overall, when the edges of the tile roof are

exposed to wind flow, the peak pressure equalization values increase dramatically. When

comparing tiled roofing to other air-permeable systems, these edge values are not

considered. However, the exposed edge effect is explored further in Section 4.4.3 using the

edge values from Table 4.7.

Table 4.7: Summary of PEF values along with the effective wind area taken from studies done on North American tile roofing.

Author	Year	Title	Tile Profile	Fastening	Battens	Roof Zone	$\dfrac{\left\{\widehat{C_{pn}}\left\|\begin{matrix}x\\t\in\mathbb{R}\\\theta\end{matrix}\right.\right\}}{\left\{\widehat{C_{pe}}\left\|\begin{matrix}x\\t\in\mathbb{R}\\\theta\end{matrix}\right.\right\}}$ (Equation 4.16)	Effective Wind Area (m^2)
Smith & Morrison	2019	Full-scale wind tunnel testing of North American and Australian roofing tile systems	Flat	Screws	Yes	Field	0.79	0.124
						Edge	1.42	0.124
					No	Field	0.80	0.124
						Edge	1.55	0.124
			S-Shape		Yes	Field	0.93	0.132
						Edge	1.00	0.132
				Foam	No	Field	0.93	0.132
						Edge	1.00	0.132

Table 4.8: Summary of PEF values along with the effective wind area taken from studies done on Australian tile roofing.

Author	Year	Title	Tile Profile	Sarking	$\dfrac{\left\{\widehat{C_{pn}}\left\vert\begin{smallmatrix}x\\t\in\mathbb{R}\\\theta\end{smallmatrix}\right.\right\}}{\left\{\widehat{C_{pe}}\left\vert\begin{smallmatrix}x\\t\in\mathbb{R}\\\theta\end{smallmatrix}\right.\right\}}$ (Equation 4.16)	Effective Wind Area (m^2)
Smith & Morrison	2019	Full-scale wind tunnel testing of North American and Australian roofing tile systems	Flat	Yes	0.95	0.124
			Flat	No	1.00	0.124
			S-Shape	Yes	0.95	0.132
			S-Shape	No	0.94	0.132

4.3.6   Solar Panels

Roof mounted solar panels that are parallel to the roof surface have the same cavity flow interaction with external flows that air-permeable multilayer cladding systems do, causing pressure equalization on the panels. Roof mounted solar panels that are not parallel to the roof surface are not affected by pressure equalization. Stenabaugh (2015) performed a 1/20 scale wind tunnel study on solar panels with multiple G/H ratios mounted parallel to a roof. Peak external and net GCp values were presented as statistical peaks by dividing the time history into 10 sections, and then using the Gumbel distribution with the Lieblien BLUE fitting method. The PEF values were then calculated using the Geurts (2000) method shown in equation 4.16. Using data taken from Figure 7.3 of Stenabaugh (2015), Table 4.9 presents peak PEF results for each effective wind area, for solar panels with a G/H ratio smaller than 1, and solar panels with a G/H ratio larger than or equal to 1. Only effective wind areas that are contained within the middle of the array are considered in order to remove the effect of the exposed edge (Case 1 & 2 in Stenabaugh (2015)).

Table 4.9: Summary of PEF values along with the effective wind area taken from studies done on solar panels.

Author	Year	Title	$\dfrac{\left\{\widehat{C_{pn}}\ \middle\|\ \begin{array}{c}x\\ t\in\mathbb{R}\\ \theta\end{array}\right\}}{\left\{\widehat{C_{pe}}\ \middle\|\ \begin{array}{c}x\\ t\in\mathbb{R}\\ \theta\end{array}\right\}}$ **(Equation 4.16)**	Effective Wind Area	G/H
Stenabaugh	2015	Design wind loads for solar modules mounted parallel to the roof of a low-rise building.	0.85	0.7275	< 1
			0.99	0.7275	< 1
			0.85	1.455	< 1
			0.92	1.455	< 1
			0.80	2.183	< 1
			0.76	2.183	< 1
			0.75	2.91	< 1
			0.78	2.91	< 1
			0.64	4.365	< 1
			0.71	4.365	< 1
			0.63	5.82	< 1
			0.63	5.82	< 1
			0.61	7.275	< 1
			0.30	0.7275	≥ 1
			0.35	0.7275	≥ 1
			0.25	1.455	≥ 1
			0.25	1.455	≥ 1
			0.22	2.183	≥ 1
			0.20	2.183	≥ 1
			0.20	2.91	≥ 1
			0.18	2.91	≥ 1
			0.15	4.365	≥ 1
			0.18	4.365	≥ 1
			0.12	5.82	≥ 1
			0.11	5.82	≥ 1
			0.11	7.275	≥ 1

This study was then used to develop section 29.4.4 in ASCE 7-16 – "*Rooftop Solar Panels Parallel to the Roof Surface on Buildings of All Heights and Roof Slopes*". Figure 4.1 presents Figure 29.4-8 from ASCE 7-16 (2017), showing the solar panel pressure equalization factor.
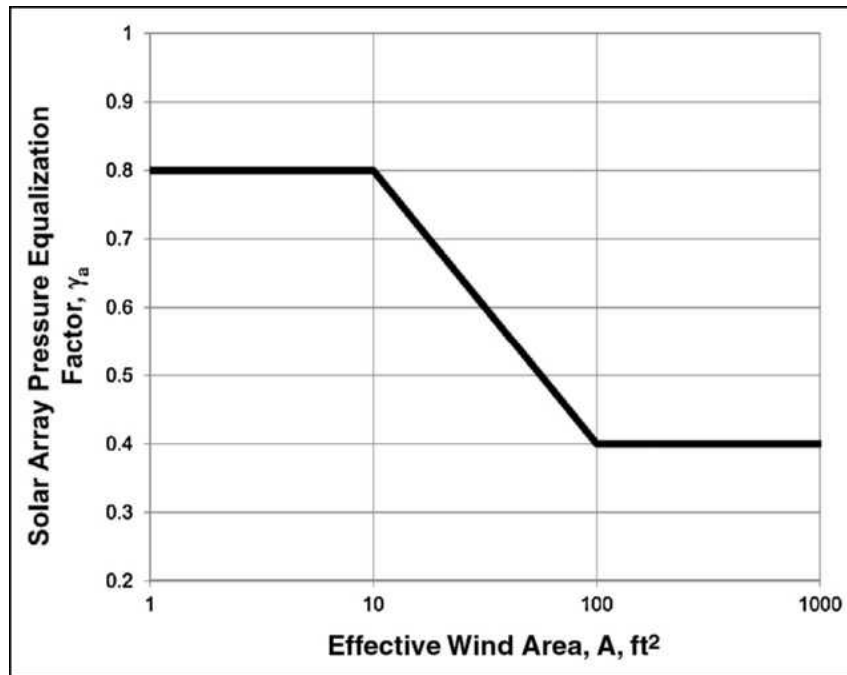
Figure 4.1: Pressure equalization factor as a function of effective wind area for solar panels (Figure 29.4-8 in ASCE 7-16 (2017)).

Section 29.4.4 in ASCE 7-16 also gives guidelines on an array edge factor, γ_ϵ, to account for the turbulent effects at the exposed edges of the system. This is discussed further in Section 4.4.3 of this paper, and is not accounted for in Figure 4.1 (the array edge factor is applied as a separate multiplication factor). As the only design guideline for any type of air-permeable multilayer cladding, Figure 4.1 can be used to compare to the peak PEF data of the other studies presented earlier in this section.

4.4   Design Recommendations

4.4.1   Effective Wind Area

Using the data from Section 4.3, Figure 4.2 presents the pressure equalization factor for different air-permeable multilayer systems as a function of the effective wind area.
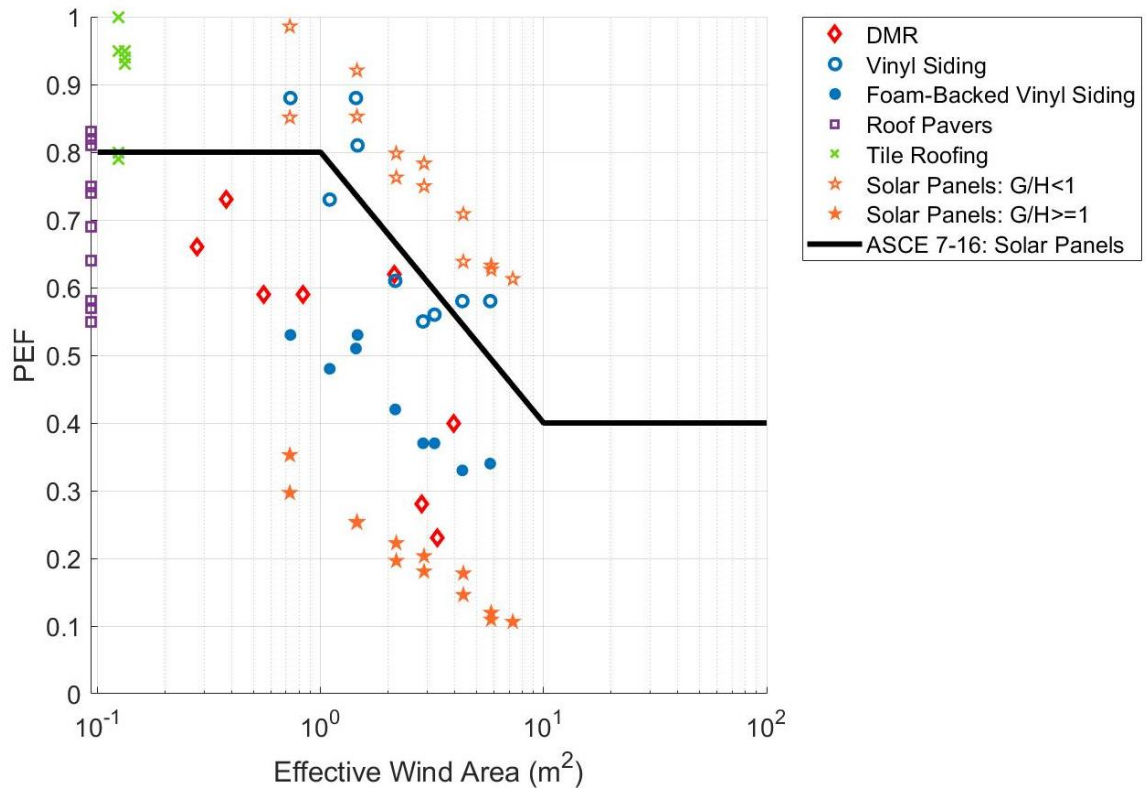
Figure 4.2: Pressure equalization factor as a function of the effective wind area for multiple types of air-permeable multilayer systems.

Although it is clear that the differing geometry between the types of air-permeable multilayer cladding is causing some differences in the data, this figure shows that the peak PEF values across all air-permeable multilayer systems are following a similar pattern to

the guidelines for solar panels in ASCE 7-16. Some systems with a small G/H ratios (such as vinyl siding) are exceeding the guidelines, while some systems with a large G/H ratio (such as foam backed vinyl siding) are much lower than the guidelines. However, all systems follow a similar slope of PEF as a function of the effective wind area to the current ASCE 7-16 guidelines for solar panels, The rest of this section deals with other factors that play a role in the PEF of air-permeable multilayer systems.

4.4.2   G/H Ratio

Chapter 1 explored the idea that the geometry of air-permeable multilayer systems is often convoluted and hard to define. However, the literature on air-permeable multilayer systems has shown that the G/H ratio is an important geometric ratio for determining the pressure equalization in a system (Oh & Kopp, 2014; Stenabaugh, 2015). Figure 4.3 shows a graph presented in Stenabaugh (2015) that shows the pressure equalization coefficient versus the G/H ratio for different tributary areas of solar panels. This shows that for all areas, the pressure equalization coefficient decreases from G/H=0 to G/H=1. From there, it reaches an asymptote, leading to a consistent pressure equalization coefficient for larger G/H ratios. However, due to the scale of this graph, it is hard to examine the relationship of PEF at small G/H values.
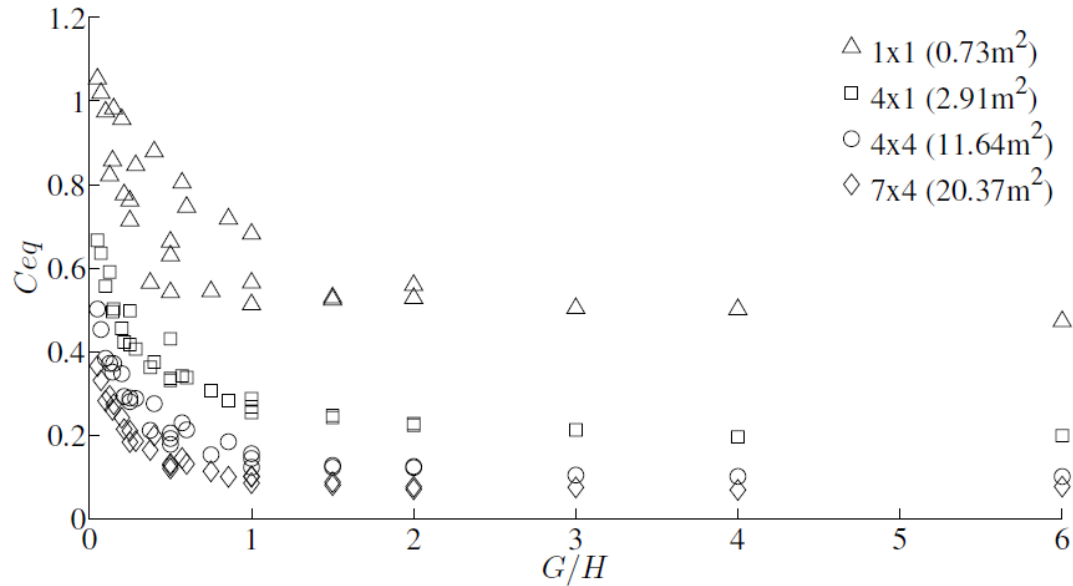
Figure 4.3: Pressure equalization coefficients with respect to the G/H ratio for four tributary areas of solar panel (from Stenabaugh (2015)).

Mooneghi et al. (2015) also examined the relationship between the G/H ratio and the peak PEF value of roof pavers. Using the data from Table 4.3 and Figure 4.3, Figure 4.4 presents a plot of the PEF values as a function of the G/H ratio for a roof pavers and solar panels of varying effective wind areas (only values of G/H between 0 and 1 are plotted because, as shown in Figure 4.3, PEF values with a G/H ratio larger than 1 remain constant). Figure 4.4 and Figure 4.3 show that the relationship between the PEF and G/H is negatively exponential (i.e. PEF increases exponentially as G/H decreases). To simplify this for design, the trend of PEF values between G/H=0 to G/H=1 can be approximated as two linear trendlines (which are also plotted on Figure 4.4). A cutoff of G/H of 0.25 was chosen by visually examining where the trend in data changes dramatically. The linear trendlines are similar across the different products with different effective wind areas, demonstrating

that the effect of the G/H ratio is similar across air-permeable multilayer cladding types and effective wind areas. There are some variations in the data, which are likely due to the exposed edge effects in the solar panel study (which are further explained in section 4.4.4). This shows that linear interpolation between G/H=0 to G/H=0.25 and linear interpolation between G/H=0.25 to G/H=1 is an appropriate method to find the value of PEF for any G/H ratio between G/H=0 to G/H=1.
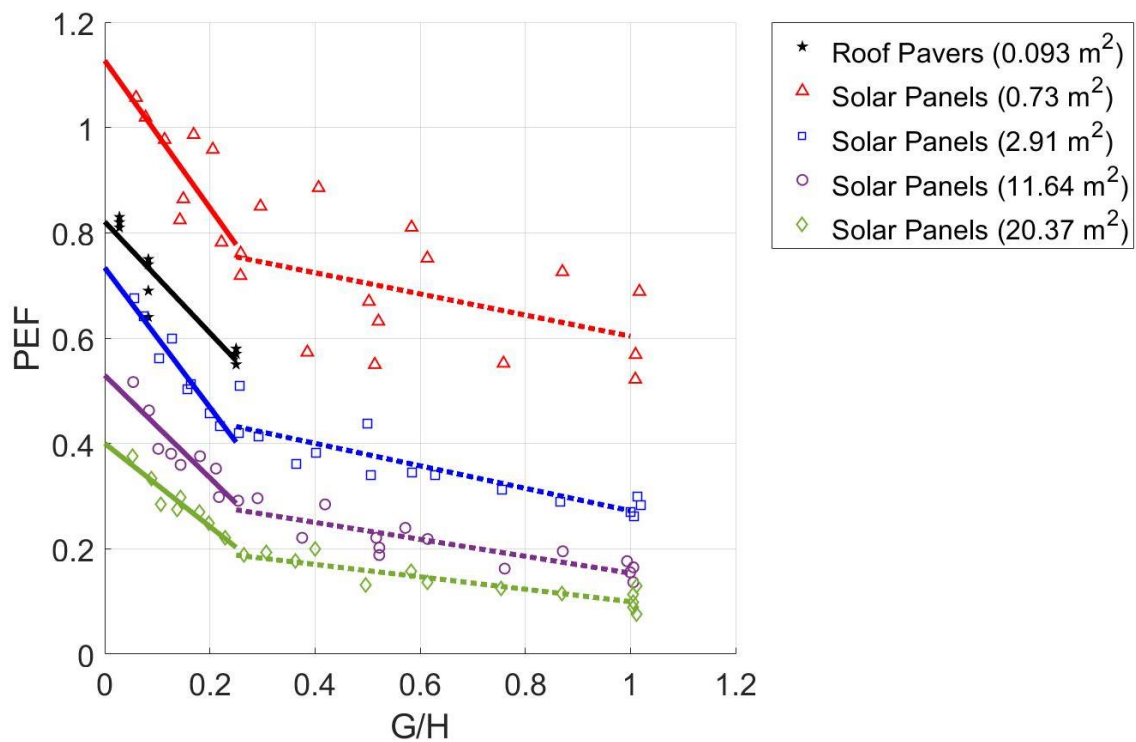
Figure 4.4: Pressure equalization factor as a function of the G/H ratio for roof pavers and solar panels with varying effective wind areas. Linear trendlines of each system are given for G/H=0 to 0.25 (solid line) and G/H=0.25 to 1 (dashed line).

However, for materials like vinyl siding, foam-backed vinyl siding, and discontinuous metal roofing, and potentially other air-permeable multilayer systems, it is extremely difficult, perhaps impossible, to calculate this ratio. Recommendations for determining an

effective G/H ratio $(G/H)_{eff}$ of air-permeable multilayer systems with difficult to define geometry are made in Section 4.6.

4.4.3 Panel Size

Figure 4.4 also showed that although the roof pavers have a smaller effective area, they have an overall lower PEF than solar panels with a higher effective area. This is because the panel size of the roof pavers is smaller than the panel size of the solar panels. The effect of panel size only applies to air-permeable multilayer cladding systems. This is because as the panel size increases on air-permeable multilayer cladding systems, the peak external pressure remains the same, but the peak cavity pressure suction decreases, which increases the PEF. This demonstrates that the effect of the panel size is aerodynamically caused by the cavity pressure distribution of air-permeable multilayer systems. Oh & Kopp (2015) determined a parameter that controls the cavity pressure distribution by defining it as the ratio of losses across the air-permeable layer over the losses along the cavity, or:

$$\phi = \left[\frac{G}{H}\right]^2 \left[\frac{fL/H}{C_L}\right] \tag{4.17}$$

where $f = 24/Re$ is the friction factor for laminar Couette flow between parallel plates. The results from Oh & Kopp (2015) show that the boundary between varying cavity pressures and uniform cavity pressures can be characterized as $\phi = 1$, i.e.,

$$\begin{cases} \phi > 1 & varying\ cavity\ pressure\ (approx.linear) \\ \phi < 1 & uniform\ cavity\ pressures \end{cases} \tag{4.18}$$

This transition from varying cavity pressures to uniform cavity pressures is what decreases the peak cavity pressure suction, causing the increase in PEF. This parameter also shows the cavity pressure distribution is proportional to L/H^3. The dataset currently presented in this section is not robust enough to perform an analysis of the panel size vs. PEF. However, because the data collected is full-scale data with cladding sizes that are used in typical North American construction, the results for the effective wind area still hold. Future work should be done to develop a panel size factor for the PEF for air-permeable multilayer cladding systems that have variable panel sizes such as roof pavers and solar panels. For now, some limitation on panel size should be noted for the validity of the design values for air-permeable multilayer cladding systems.

4.4.4   Exposed Edges

Although it was shown in Chapter 3 that the location on the roof does not matter for PEF values, this study was done with edges that were sealed from the turbulent flow field that is created on the leading edges of building materials. Some air-permeable multilayer systems are frequently installed with exposed edges (e.g., solar panels). This means that the cavity at the edges of the system are exposed to the turbulent flow field created when the wind interacts with the leading edge of the air-permeable multilayer system. Figure 4.5 shows a schematic showing the exposed edge effect created from flow separation.
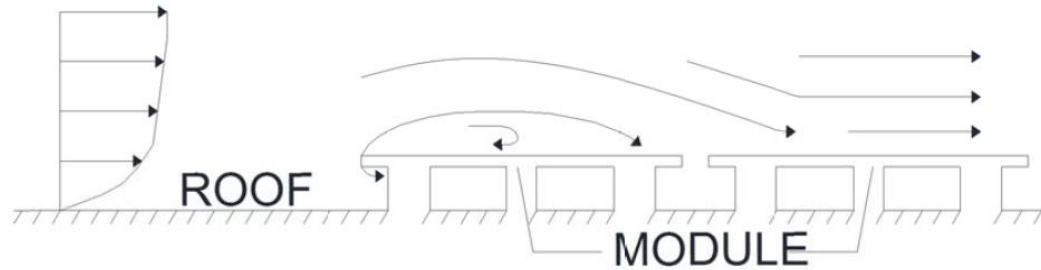
Figure 4.5: Schematic showing the exposed edge effect created from flow separation (from Stenabaugh, 2015)).

This exposed edge effect is accounted for in ASCE 7-16 (2017), where Figure 29.4-7 gives guidelines on an array edge factor, γ_ϵ. This is a multiplicative factor that is applied to the edges of the array only, specifically, $\gamma_\epsilon = 1.5$ at a distance of 1.5 times the width of the cladding from an exposed edge. As an example of this, Smith & Morrison (2019) also noted in their full-scale study on tile roofing that when the flow is perpendicular to the eave line, the peak net pressure can exceed the peak external pressure. This can also be seen in Table 4.7, where the PEF is increased at the eaves and corners by a factor of $1.08 - 1.94$. This study also showed that this large range of factors is partially attributed to the shape of the exposed edge. As shown in Table 4.7, tiles with an S-shaped profile had a much smaller increase than the tiles with a flat profile. Future work should be done to develop a value for an exposed edge factor, as well as quantify the effect that the profile of the exposed edge has on the exposed edge factor.

4.4.5　Parapet Height

On certain types of air-permeable multilayer systems such as roof pavers, it is common to install parapets along the edges of the roof. These parapets provide sheltering from the worst turbulent flow at the corners and edges of the roof. Therefore, parapets have a reducing effect on the overall net load considered on a system. Mooneghi et al. (2015) examined the relationship between the parapet height (normalized by the eave height), and the peak PEF value of roof pavers. Figure 4.6 shows a graph of this reduction factor, (from Mooneghi et al. (2015)) as a function of h_p/H_E, where h_p is the height of the parapet, and H_E is the eave height. . Future work should be done to develop a value for a shielding factor not only to account for the shielding effect due to parapets, but any obstruction on the edges of air-permeable multilayer cladding systems.
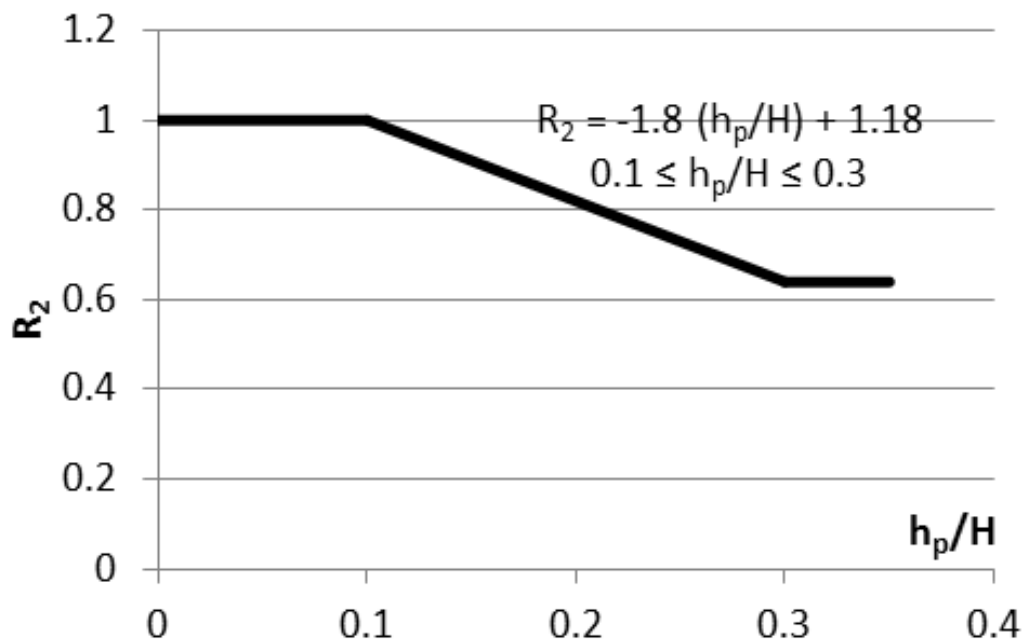
Figure 4.6: Parapet reduction factor as a function of the parapet height over the height of the cavity (from Mooneghi et al., 2015)).

4.5 Potential Guidelines for ASCE 7 (γ_A)

This section (although conservative and simplified) provides, for the first time, design guidelines for calculating the pressure equalization factor (and consequently the net load) of typical air-permeable multilayer systems. These guidelines could then be used to alter equation 29.4-7 in ASCE 7-16 (2017) so that the net pressure can be obtained for any air-permeable multilayer system rather than just solar panels mounted parallel to a roof, or:

$$p_n = q_h(GCp)(PEF) \tag{4.19}$$

where the PEF is equal to:

$$PEF = \gamma_A \gamma_\phi \gamma_\epsilon \gamma_S \tag{4.20}$$

where γ_A is the effective area factor, γ_ϕ is the panel size factor γ_ϵ is the exposed edge factor, and γ_S is the shielding factor. Although this study recommends the use of a panel size factor, an exposed edge factor and a shielding factor, it makes no direct recommendations for what those values should be.

The effective area factor (γ_A) accounts for the effect that the effective wind area has on the pressure equalization factor. This factor also encompasses the effect that the G/H ratio has on the pressure equalization factor. As shown in Figure 4.2 in Section 4.4.1, the PEF decreases as the effective wind area increases. Figure 4.7 presents design recommendations for ASCE 7-16 for the effective area factor (along with the data used to develop these recommendations). The three design lines on Figure 4.7 are for systems with a G/H ratio that approaches zero (systems with a G/H ratio of exactly zero are single-layered systems

with no pressure equalization), systems with a G/H ratio of 0.25, and systems with a G/H ratio of 1 or larger. The three design lines were chosen for those specific G/H ratios in order to be able to linearly interpolate between 0 and 0.25, as well as 0.25 to 1, to coincide with the trendlines detailed in Figure 4.4. All of the design lines remain constant at an effective wind area equal to or larger than 10 m^2 This is because no data is available for air-permeable multilayer systems with an effective wind area that large, except for the current ASCE 7-16 guidelines on solar panels. This could be further refined in the future by obtaining data with larger effective wind areas. Similarly, all of the design lines remain constant at an effective wind area equal to or smaller than 1 m^2. This cut-off has practical value in terms of expressing the maximum PEF (it is also consistent with the current ASCE 7-16 guidelines for solar panels), but future work should be done to ensure the aerodynamics of air-permeable multilayer systems at small effective wind areas are being properly represented.

As mentioned in Section 4.4.2, the G/H ratio for air-permeable systems with small gap widths and small cavity heights can be challenging to measure. A proposed guideline to deal with this challenge is to use the data presented in Figure 4.2 to determine which G/H curve is appropriate for each type of air-permeable multilayer system by using linear interpolation of the design graphs presented in Figure 4.7. This could be defined as an effective G/H ratio, or $(G/H)_{eff}$. Table 4.10 presents $(G/H)_{eff}$ values for air-permeable multilayer cladding with hard to define geometries such as vinyl siding, foam-backed vinyl siding, discontinuous metal roofing, and tiled roofing.
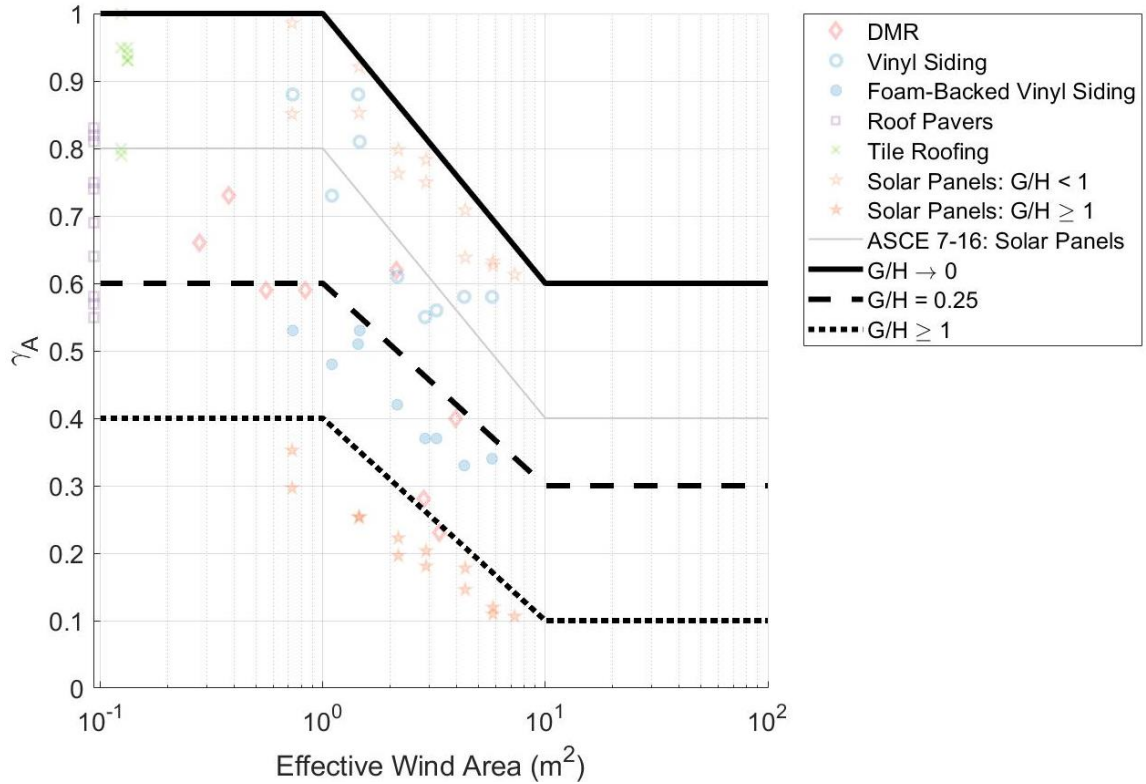
Figure 4.7: Recommended design guidelines for the pressure equalization of air-permeable multilayer systems, taking into account the effective area and the G/H ratio.

Table 4.10: Effective G/H ratio for air-permeable multilayer cladding systems.

Air-Permeable Multilayer Cladding Type	$(G/H)_{eff}$
Discontinuous Metal Roofing	3/16
Vinyl Siding	1/16
Foam-Backed Vinyl Siding	1/4
Tile Roofing	1/64

These $(G/H)_{eff}$ can be used as a conservative estimate for determining the effective wind area in Figure 4.7 rather than attempting to measure G/H on a real system. This table could accompany a potential design standard for air-permeable multilayer cladding systems to aid in the calculating of the effective wind area. Further work should be done to synthesize more data to add more types of air-permeable multilayer cladding to this list.

The panel size factor (γ_ϕ) accounts for effect that larger panel sizes have on the PEF. As panel sizes get larger, the peak external pressure remains the same, but the cavity pressure distribution changes from linear to uniform, resulting in a decrease in the peak cavity suction. These effects combined raise the PEF value.

The exposed edge factor (γ_ϵ) accounts for cavities at the edges of the system that are exposed to the turbulent flow field created when the wind interacts with the leading edge of the air-permeable multilayer system. This creates a separation bubble on the upper surface of the cladding, leading to a negative external pressure; the leading exposed edge also allows air to flow directly into the cavity, creating a positive pressure on the lower surface of the cladding; the net result of these pressures is a suction pressure greater than the negative external pressure applied to the system, thereby increasing the PEF value.

The shielding factor (γ_S) accounts for the shielding effect that parapets (or any type of obstruction on the edges of roofs or walls) have on air-permeable multilayer systems. The shielding prevents the separation bubble caused by the leading edge of the roof from forming directly on the surface of the air-permeable multilayer cladding, thereby reducing the PEF value.

4.6 Summary

Although there have been individual studies done on pressure equalization, there is no current consensus on what methods should be used to calculate the PEF of air-permeable multilayer cladding, or whether different air-permeable multilayer cladding should use the same methods to determine the pressure equalization factor. The objective of this chapter was to develop a unified approach to the pressure equalization factor for typical air-permeable multilayer systems with small openings and a relatively large cavity volume.

Definitions of pressure equalization factors were examined in order to determine the most appropriate definition for use in developing design values of PEF for air-permeable multilayer systems. It was determined that the most appropriate definition to use was the non-simultaneous pressure equalization coefficient proposed by Geurts (2000), due to the fact that it is consistent with the enveloping methods for external pressure coefficients used in ASCE 7-16 (2017).

Pressure equalization studies on air-permeable multilayer systems (discontinuous metal roofing, vinyl siding, roof pavers, tile roofing, and solar panels) were examined in order to develop design guidelines for air-permeable multilayer systems. The peak PEF values for each effective area were obtained using the data reduction method highlighted in Gavanski et al. (2016). The value for each of these studies were then synthesized and directly compared by plotting each of them against their effective area. It showed that has the effective area increases, the PEF decreases. The effect of the G/H ratio was also examined for roof pavers and solar panels. It showed that the PEF has a negative exponential relationship to the G/H ratio. This relationship was approximated using two linear

trendlines. The effect of panel size, exposed edges, and shielding were also briefly examined, but was not the focus of this study.

By synthesizing these studies and considering the factors that affect peak PEF values, design PEF values were given as a multiplication factor to apply to external pressure coefficients such as those found in ASCE 7. These design values were created by enveloping the worst PEF values as a function of effective wind area and the G/H ratio. Considerations were given for panel size, exposed edges or shielding by utilizing additional multiplication factors for those scenarios. Effective G/H ratios were also provided for air-permeable multilayer cladding with hard to define geometry. It is recommended that these design PEF values should be considered for inclusion in building standards, as this fills a current gap in knowledge of air-permeable multilayer systems. Although ASCE 7-16 (2017) is used as an example, these design PEF values could be applied to any building code where this gap in knowledge is present. It is recommended that the provision of PEF values be removed from individual manufacturing standards (such as the one present in ASTM D3609 (2013)), and instead be provided generally in building codes. Future wind tunnel studies should be performed to verify the model provided in this chapter, as well as to potentially add to the database of values for PEF (using the data reduction method, and the same definition for PEF for consistency).

5   Conclusions

5.1   Key Findings

Although building codes continue to improve, monetary losses from severe wind storms continue to increase, primarily due to failures of the building envelope and connections in residential buildings. Therefore, mitigating the losses in these severe wind storms depends significantly on protecting the components and cladding of buildings. A common type of cladding used in the construction of these buildings in North America is air-permeable multilayer cladding systems such as vinyl siding and roof pavers. However, they are not well accounted for in current building codes. As an example, ASCE 7-16 (2017), section C30.1.5. indicates that:

> *"[…] If the designer desires to determine the pressure differential across a specific cladding element in combination with other elements comprising a specific building envelope assembly, appropriate pressure measurements should be made on the applicable building envelope assembly or reference should be made to recognized literature […]"*

The lack of accurate and specific building code guidance is due to the complexity of the cavity flow and resulting pressure equalization between the cladding and sheathing layers of the building. Some air-permeable multilayer products have manufacturing standards that deal with design loads by eliminating the cavity flow and applying a pressure equalization factor to account for the reduction in net load caused by this cavity flow. Unfortunately, these pressure equalization factors can be inaccurate due to not accounting for the spatial

variations of external pressures. With this in mind, the objective of this thesis was to attempt to unify the different pressure equalization studies on different air-permeable multilayer systems to develop design recommendations for pressure equalization factors for use in design standards.

First, the typical airbox test for vinyl siding was expanded upon to a multichambered approach, which was then compared to a benchmark study performed by the Insurance Institute for Business & Home Safety. The results indicate that using multichambered, pressure-based testing to obtain wind loads for air-permeable, multilayer wall systems with flexible cladding provides similar results to a full-scale wind tunnel. It also demonstrated that the spatial variations in pressure play a much larger role than the temporal variations. Finally, it showed that the pressure equalization factor for vinyl siding in ASTM D3679-13 (2013) is inaccurate, which could be leading to some of the common failure seen in damage surveys.

Another issue with the codification of the wind loads on air-permeable multilayer systems is that design approaches to determine loads on different types of building cladding elements can vary significantly by product type, even though they may have similar basic geometries. Using the full-scale wind tunnel at the Insurance Institute for Business & Home Safety, external and net wind loads on two discontinuous metal roof systems were measured. Although the systems have different panel sizes, assembly methods, air pathways, and cavity geometries, they result in similar PEF values. This is due to both systems having small openings into the cavity and relatively large cavity volumes, which leads to relatively uniform pressure along the cavity (compared to the external pressure), resulting in similar PEF values. These PEF values were also shown to be unaffected by

wind directions as well as load level. The results also indicate that the dominant loading mechanism for discontinuous metal roofing is related to pressure equalization and not to local flow around the panel and that the external pressure gradient, which drives the flow in the cavity, also plays a significant role in the pressure equalization.

Finally, the results indicate that there is a time lag between the peak external gradient and the net pressure because of the flow inertia. This means that the inertial term in the unsteady Bernoulli equation applied to the cavity flow plays a role in reducing the net loads. Since the maximum flow rate leads to maximum pressure drop across the cladding later, the delay caused by the fluid inertia de-synchronizes the peak external and cavity pressures, reducing the peak net loads. Variability in the inertial term undoubtedly plays a role in variability of PEF values such that statistical approaches for design values, not unlike those for external pressures are required.

With these in mind, a unified approach to the pressure equalization factor for all air-permeable multilayer cladding was created by enveloping the worst case PEF values for each type and taking into account the effect that exposed edges and parapets have on the net loads. To do this, multiple methods of defining pressure equalization factor were examined. It was recommended that the envelope method as described in Geurts (2000) should be used,

$$\widehat{PEF_{ASCE\ 7}} = \frac{\left\{ \widehat{C_{pn}} \left| \begin{matrix} x \\ t \in \mathbb{R} \\ \theta \end{matrix} \right. \right\}}{\left\{ \widehat{C_{pe}} \left| \begin{matrix} x \\ t \in \mathbb{R} \\ \theta \end{matrix} \right. \right\}} \qquad [5.1]$$

due to its similarity to how external pressures are enveloped in ASCE 7-16. The peak net pressure and peak external pressure are determined from the time series using the data reduction method described in Gavanski et al. (2016).

Using this definition for the pressure equalization factor, studies on multiple different air-permeable multilayer systems were examined to create a design value for PEF taking into account the effective wind area, panel size, exposed edges, and shielding. Figure 5.1 gives a summary of the design recommendations for ASCE 7. These design recommendations could be used to fill the current gap in knowledge in air-permeable multilayer cladding in building codes such as ASCE 7 or NBCC.

$$PEF = \gamma_A \gamma_\phi \gamma_\epsilon \gamma_S$$

where:
γ_A = Effective Area Factor
γ_ϕ = Panel Size Factor
γ_ϵ = Exposed Edge Factor
γ_S = Shielding Factor

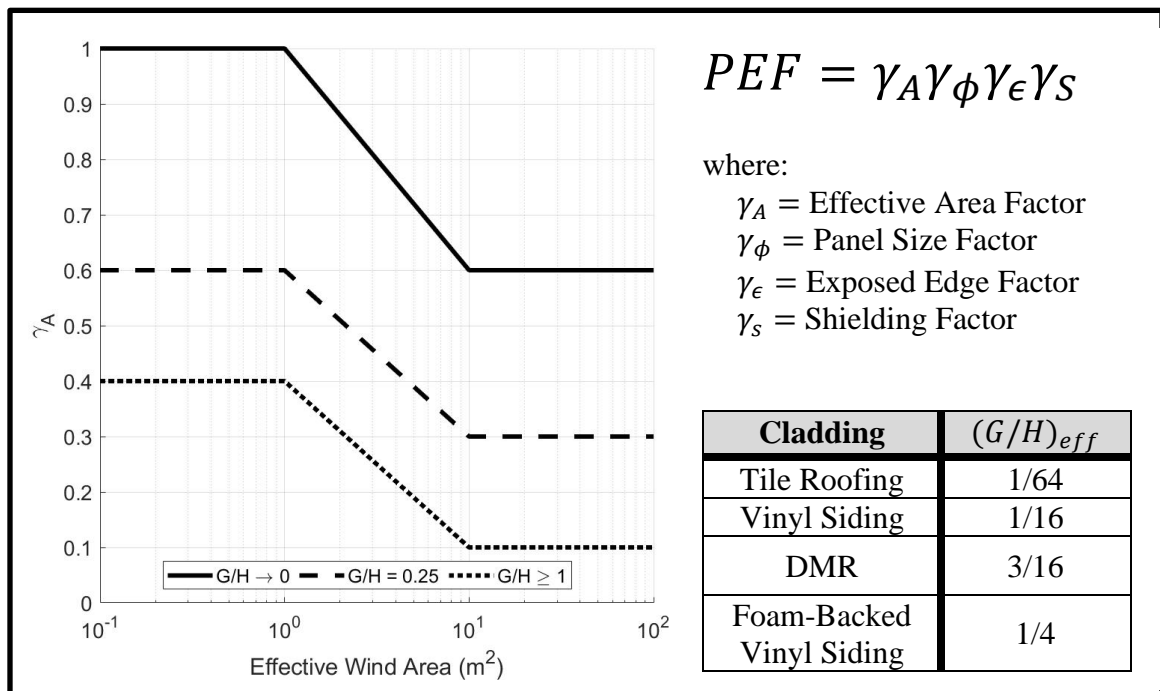| Cladding	$(G/H)_{eff}$
Tile Roofing	1/64
Vinyl Siding	1/16
DMR	3/16
Foam-Backed Vinyl Siding	1/4

Figure 5.1: Recommended design guidelines for pressure equalization of air-permeable multilayer systems, taking into account the effective area, panel size, exposed edges, and parapets.

5.2 Recommendations for Future Work

Although this thesis advances the field of research of pressure equalization on air-permeable multilayer systems, there is still much more that could be done. This section of the thesis explores the limitations of the work and makes recommendation for future study.

- The downside of using the Geurts (2000) method for defining the pressure equalization coefficient is that the design loads obtained using this approach are a step removed from the equations and numerical models used to calculate cavity pressures in air-permeable multilayer systems. Further developments to the theoretical models would be useful.

- Chapter 4 synthesizes the experimental data from many different cladding systems. However, the dataset is still small for creating design recommendations. Future testing (or the continued synthesis of data) is recommended to further refine the values for γ_A presented in Chapter 4.

- Further testing is required at large ($> 10 \; m^2$) effective wind areas to validate the design values for those effective wind areas. The design values at large effective wind areas are likely conservative (safe) due to this limitation.

- Another limitation of this study is the difficulty of determining G/H values on some types of air-permeable multilayer systems, such as vinyl siding and discontinuous metal roofing. A more robust way to define the G/H ratio (or an effective G/H ratio) for these types of systems would also improve the design standard.

- Future work should be done to determine the effect of the panel size on the cavity pressure distribution of air-permeable multilayer systems.

- Future work should be done to determine the net loads on the exposed edges of air-permeable multilayer systems, as well as the effect that the profile of the cladding edge has on these net loads.

- Future work should also be done to full quantify the effect that shielding the edges of roofs or walls has on the net loads of air-permeable multilayer systems.

References

Ali, H. M., and Senseny, P.E. (2003). Models for standing seam roofs. *J. Wind Eng. Ind. Aerodyn.* 91, 1689-1702, doi:10.1016/j.jweia.2003.09.014

Aly, A., & Bitsuamlak, G. (2014). Wind-induced pressures on solar panels mounted on residential homes. *J. Arch. Eng.* 20(1): 4013003.

Amano, T., Fujii, K., and Tazaki, S., (1988). Wind loads on permeable roof-blocks in roof insulation systems. *J. Wind Eng. Ind. Aerodyn.* 29:39-48.

American Society for Civil Engineering. 2017. ASCE 7-16: Minimum Design Loads For Buildings And Other Structures.

Architectural Testing, Inc. (2002). *Wind Pressure Equalization Research Project Report. No. 01-40776.01 for the Vinyl Siding Institute,* Washington, DC.

ASTM D3679 (2013). *Standard Specification for Rigid Poly (Vinyl Chloride) (PVC) Siding*. ASTM International, West Conshohocken, PA, 2013, www.astm.org.

ASTM D3679 (2017). *Standard Specification for Rigid Poly (Vinyl Chloride) (PVC) Siding*. ASTM International, West Conshohocken, PA, 2017, www.astm.org.

ASTM D5206 (2012). *Standard Test Method for Windload Resistance of Rigid Plastic Siding*. ASTM International, West Conshohocken, PA, 2013, www.astm.org.

ASTM E1300 (2012). *Standard Practice for Determining Load Resistance of Glass in Buildings*. ASTM International, West Conshohocken, PA, 2012, www.astm.org.

ASTM E1592 (2012). *Standard Test Method for Structural Performance of Sheet Metal Roof and Siding Systems by Uniform Static Air Pressure Difference*. ASTM International, West Conshohocken, PA, 2012, www.astm.org.

Baskaran, B., and Brown, W., (1992). Performance of pressure equalized rainscreen walls under cyclic loading. *J. Therm. Enve. Build. Sci.* 16: 183-193.

Bienkiewicz, B., & Sun, Y., (1992). Wind-tunnel study of wind loading on loose-laid roofing systems. *J. Wind Eng. Ind. Aerodyn.* 41-44: 1817-1828.

Bienkiewicz, B. and Sun, Y. (1997). Wind loading and resistance of loose-laid roof paver systems. *J. Wind Eng. Ind. Aerodyn* 72: 401-410. doi:10.1016/s0167-6105(97)00235-3

Bienkiewicz, B., and Endo, M., (2009). Wind considerations for loose-laid and photovoltaic roofing systems. *2009 Structures Congress -Don't Mess with Structural Engineers: Expanding Our Role.* 2578-2587. Reston, VA: American Society of Civil Engineers.

Burgess, J.C., (1995). Air pressure equalization in rainscreened joints by geometric alteration. *Build. Env.* 30: 13-18.

Choi, E., and Wang, Z., (1998). Study on pressure-equalization of curtain wall systems. *J. Wind Eng. Ind. Aerodyn.* 73: 251-266.

Cook, N.J., Keevil, A.P., and Stobart, R.K. (1988). "Brerwulf - the big bad wolf". *J. Wind Eng. Ind. Aerodyn.* 29 (1-3): 99-107. doi:10.1016/0167-6105(88)90149-3.

Cope, A.D., Crandell, J.H., Johnston, D., Kochkin,V., Liu, Z., Stevig, L., and Reinhold, T.A., (2012). Wind loads on components of multi-layer wall systems with air-permeable exterior cladding. *Proceedings of the ATC-SEI Advances in Hurricane Engineering Conference*. Miami, FL.

Cope, A.D., Crandell, J.H., Liu, Z., and Stevig, L., (2014). Wind loads on fasteners used to attach flexible porous siding on multi-layer wall systems. *J. Wind Eng. Ind. Aerodyn.* 133, 150-159. doi:10.1016/j.jweia.2014.06.007

Emswiler, J.E., (1926). The neutral zone in ventilation. *ASHVE Journal.* 32.

Engineering Data Science Unit. (1983). *Strong Winds in the Atmosphere Boundary Layer. Part 2: Discrete Gust Speeds, Data Item 83045*. London, UK.

Fazio, P., & Kontopidis, T., (1988). Cavity pressure in rainscreen walls. *Build. Env.* 23: 137-143.

Gavanski, E., and Kopp, G.A., (2011). Examination of load resistance in window glass design. *J. Arch. Eng.* 17, 42-50. doi:10.1061/(asce)ae.1943-5568.0000030

Gavanski, E., and Kopp, G.A., (2011). Glass breakage tests under fluctuating wind loads. *J. Arch. Eng.* 17, 34-41. doi:10.1061/(asce)ae.1943-5568.0000028

Gavanski, E., and Kopp, G.A., (2012). Effects of pressure equalization on the performance of residential wall systems under extreme wind loads. *J. Struct. Eng.* 138, 526-538. doi:10.1061/(asce)st.1943-541x.0000476

Gavanski, E., Gurley, K.R., and Kopp, G.A., (2016). Uncertainties in the estimation of local peak pressures on low-rise buildings by using the Gumbel distribution fitting approach. *J. Struct. Eng*, 142:11.

Gerhardt, H.J., and Jansen, F., (1994). Wind loads on wind permeable facades. *J. Wind Eng. Ind. Aerodyn.* 53, 37-48.

Geurts, C. (2000). Wind loads on permeable roof covering products. *Fourth Colloquium on Bluff Body Aerodynamics and Applications*. Bochum, Germany: Rufr Universitat.

Geurts, C., and Blackmore, P., (2013). Wind loads on stand-off photovoltaic systems on pitched roofs. *J. Wind Eng. Ind. Aerodyn.* 123:239-249.

Ginger, J.D., Holmes, J.D. and Kim, P.Y. (2010). Variation of internal pressure with varying sizes of dominant openings and volumes. *J. Struct. Eng.* 136(9): 1319-1326.

Ginger, J., Payne, M., Stark, G., Sumant, B., & Leitch, C. (2011). *Investigation on Wind Loads Applied to Solar Panels Mounted on Roofs.* Townsville, Australia: Cyclone Testing Station.

Gurley, K.R., and Masters, F.J., (2011). Post-2004 hurricane field survey of residential building performance. *Nat. Haz. Review*. 12, 177–183. doi:10.1061/(asce)nh.1527-6996.0000044

Henderson, D.J., Williams, C., Gavanski, E., and Kopp, G.A., (2013). Failure mechanisms of roof sheathing under fluctuating wind loads. *J. Wind Eng. Ind. Aerodyn.* 114, 27-37. doi:10.1016/j.jweia.2013.01.002

Henderson, D.J., Morrison, M.J. and Kopp, G.A., (2013). Response of toe-nailed, roof-to-wall connections to extreme wind loads in a full-scale, timber-framed, hip roof. *Eng. Struct.* 56, 1474-1483. doi:10.1016/j.engstruct.2013.07.001

Holmes, J.D., (1979). Mean and fluctuating internal pressure induced by wind. In: *Proceedings of the fifth international conference on wind engineering.* Colorado State University; 435-450.

Holmes, J.D. (2013). *Wind Loading of Structures - 3rd Edition.* New York, New York: Taylor & Francis.

Inculet, D.R., & Davenport, A.G., (1994). Pressure-equalized rainscreens: A study in the frequency domain. *J. Wind Eng. Ind. Aerodyn*. 53: 63-87.

ISO 4354, (2009). *Wind Actions on Structures.* International Organization for Standardization, Geneva, Switzerland. www.iso.org.

Kala, S., Stathopoulos, T. and Suresh Kumar, K. (2008). Wind Loads on Rainscreen Walls: Boundary Layer Wind Tunnel Experiments. *J. Wind Eng. Ind. Aerodyn.* 96(6-7), 1058-1073.

Killip, I.R., & Cheetham D.W., (1984). The prevention of rain penetration through external walls and joints by means of pressure equalization. *Build. Env.* 19: 81-91.

Kind, R., & Wardlaw, R., (1982). Failure mechanism of loose-laid roof-insulation systems. *J. Wind Eng. Ind. Aerodyn.* 9: 325-341.

Kopp, G.A., Oh, J.H., and Inculet, D.R., (2008). Wind-induced internal pressures in houses. *J. Struct. Eng.* 134(7): 1129-1138.

Kopp, G.A., Morrison, M.J., Gavanski, E., Henderson, D., and Hong, H.P., (2010). The 'three little pigs' project: hurricane risk mitigation by integrated wind tunnel and full-scale laboratory tests. *Nat. Haz. Review.* 11, 151-161. doi:10.1061/(asce)nh.1527-6996.0000019

Kopp, G.A., Farquhar, S., Morrison M.J., (2012). Aerodynamic mechanisms for wind load on tilted, roof-mounted solar arrays. *J. Wind Eng. Ind. Aerodyn.* 111, 40-52.

Kopp, G.A., Morrison, M.J., and Henderson, D.J., (2012). Full-scale testing of low-rise, residential buildings with realistic wind loads. *J. Wind Eng. Ind. Aerodyn.* 104-106, 25-39. doi:10.1016/j.jweia.2012.01.004

Kopp, G. (2013). Wind loads on low profile, tilted, solar arrays placed on large, flat, lowrise building roofs. *J. Struct. Eng.* 140(2): 04013057.

Kumar, K., Stathopoulos, T. and Wisse, J.A. (2003). Field Measurement Data of Wind Loads on Rainscreen Walls. *J. Wind Eng. Ind. Aerodyn.* 91(11), 401-1417.

Kumar, K., & Van Schijndel, A. (1999). Prediction of pressure equalization performance of rainscreen walls. *Wind and Structures.* 2(4): 325- 345.

Kumar, K., (2000). Pressure equalization of rainscreen walls: a critical review. *Build. Env.* 35, 161-179. doi:10.1016/s0360-1323(9)00015-3

Lieblein, J. 1974. *Efficient methods of extreme-value methodology.* NBSIR 74-602, National Bureau of Standards, Washington, DC.

Lou, W., Huang, M., Zhang, M., and Lin, N., (2012). Experimental and zonal modeling for wind pressures on double-skin facades of a tall building. *Ener Build.* 54:179-191.

Miller, C.S., Kopp, G.A., Morrison, M.J., Kemp G., and Drought, N., (2017). A multichamber, pressure-based test method to determine wind loads on air-permeable, multilayer cladding systems. *Front. Built Env.* 3:7.

Miller, C.S., Kopp, G.A., Morrison, M.J., (2020). Aerodynamics of air-permeable multilayer roof cladding. Submitted to *J. Wind Eng. Ind. Aerodyn.* on October 20, 2019.

Mooneghi, M., Irwin, P., and Chowdhury, A.G., (2014). Large-scale testing on wind uplift of roof pavers. *J. Wind Eng. Ind. Aerodyn.* 128, 22-36. doi:10.1016/j.jweia.2014.03.001

Mooneghi, M., Irwin, P., and Chowdhury, A.G., (2015). Toward guidelines for design of loose-laid roof pavers for wind uplift. *Wind and Structures.* 22(2):133-160.

Moravej, M., Zisis, I., Chowdhury, A., Irwin, P., and Hajra, B., (2016). Experimental assessment of wind loads on vinyl wall siding. *Front. Built Env.* 2:35.

Morrison, M.J., and Kopp, G.A., (2011). Performance of toe-nail connections under realistic wind loading. *Eng. Struct.* 33, 69-76. doi:10.1016/j.engstruct.2010.09.019

Morrison, M.J., Henderson, D.J., and Kopp, G.A., (2012). The response of a wood-frame, gable roof to fluctuating wind loads. *Eng. Struct.* 41, 498-509. doi:10.1016/j.engstruct.2012.04.002

Morrison M.J., Cope A.D., (2015). Wind Performance and Evaluation Methods of Multi-Layered Wall Assemblies" *Proceeding of ASCE Structures Congress.* Portland, OR.

Morrison M.J., and Kopp, G.A., (2018). Effects of turbulence intensity and scale on surface pressure fluctuations on the roof of a low-rise building in the atmospheric boundary layer. *J. Wind Eng. Ind. Aerodyn..* 183, 140-151.

Munich RE, (2018). Natural disaster risks: Losses are trending upwards. *https://www.munichre.com/en/risks/natural-disasters-losses-are-trending-upwards.html*

National Research Council of Canada. (2015). *NBC 2015 National Building Code of Canada.* Ottawa, Canada: National Research Council of Canada.

Oh, J.H., Kopp, G.A., and Inculet D.R., (2007). The UWO contribution to the NIST aerodynamic database for wind loads on low buildings: part 3. Internal pressures. *J. Wind Eng. Ind. Aerodyn..* 95, 755-779.

Oh, J.H., and Kopp, G.A., (2014). Modelling of spatially and temporally-varying cavity pressures in air permeable, double-layer roof systems. *Build. Env.* 82, 135-150. doi: 10.1016/j.buildenv.2014.08.008

Oh, J.H., and Kopp, G.A., (2015). An experimental study of pressure distributions within a double-layered roof system in a region of separated flow. *J. Wind Eng. Ind. Aerodyn.* 138, 1-12. doi: 10.1016/j.jweia.2014.12.006

Peterka, J.A., Cermak, J.E., Cochran, L.S., Cochran, B.C., Hosoya, N., Derickson, R.G., Jones, J., Metz, B., (1997). Wind uplift model for asphalt shingles. *J. Archit. Eng.,* 147-155.

Sadek, F., and Simiu, E., (2002). Peak non-gaussian wind effects for databse-assisted low-rise building design. *J. Eng. Mech.* 128(5): 530-539.

Sharma, R.N., and Richards, P.J., (1997). Computational modelling of transient response of building internal pressures to a sudden opening. *J. Wind Eng. Ind. Aerodyn.* 72, 149-161.

Sinno, R., Surry, D., Flower, S., and Ho, E., (2003). Testing of metal roofing systems under simulated realistic wind loads. *Proceedings of the Eleventh International Conference on Wind Engineering.* Lubbock, Texas.

Smith, D.J., and Morrison, M.J. (2010). Full-scale wind tunnel testing of North American and Australian roofing tile systems. *Proceedings of the 15th International Conference on Wind Engineering.* Beijing, China.

Sparks, P.R., Schiff, S.D., Reinhold, T.A., (1994). Wind damage to envelopes of houses and consequent insurance losses. *J. Wind Eng. Ind. Aerodyn.* 53, 145–155. doi:10.1016/0167-6105(94)90023-x

Sreedevi, R., (2017). Estimation of cavity pressures in air-permeable, multi-layer systems using a lumped-leakage approach. *Electronic Thesis and Dissertation Repository.* 4549.

Standohar-Alfano, C. D., Estes, H., Johnston, T., Morrison, M. J., and Brown-Giammanco, T. M., (2017). Reducing losses from wind-related natural perils: research at the IBHS Research Center. *Front. Built Env.* 3:9.

Stathopoulos, T. (1979). Turbulent wind action of low-rise buildings. *Ph.D. Thesis.* Western University, London, Ontario, Canada.

Stathopoulos, T. (1981). Load distribution and double skin wall. *J. Struct. Div.* ST10, 2048-2049.

Stathopoulos, T., Wang, K., & Wu, H. (2000). Proposed new Canadian wind provisions for the design of gable roofs. *Can. J. Civ. Eng.* 27(5):1059-1072.

Stenabaugh, S.E., Karava, P., (2010). Deisgn wind loads for photovoltaic systems on sloped roof of residential buildings. *Proceeding of ICWE13.* Amsterdam, Netherlands.

Stenabaugh, S.E., Iida, Y., Kopp, G.A., Karava, P., (2015). Wind loads on photovoltaic arrays mounted parallel to sloped roofs on low-rise buildings. *J. Wind Eng. Ind. Aerodyn.* 139, 16-26.

Stenabaugh, S.E., (2015). Design Wind Loads for Solar Modules Mounted Parallel to the Roof of a Low-rise Building. *Electronic Thesis and Dissertation Repository.* 2817.

Straube, J.F., and Burnett, E., (1999). Rain Control and Design Strategies. *J. Build. Phys.* 23(1): 41-56

Sun, Y., Bienkiewicz, B., (1993). Numerical simulation of pressure distributions underneath roofing paver systems. *J. Wind Eng. Ind. Aerodyn.* 46-47, 517-626. doi:10.1016/0167-6105(93)90319-j

Surry, D., Sinno, R.R., Nail, B., Ho, T.C., Farquhar, S., and Kopp G.A., (2007). Structurally effective static wind loads for roof panels. *J. Struct. Eng.* 133, 871-885. doi:10.1061/(asce)0733-9445(2007)133:6(871)

Tamura, G.T., and Wilson, A.G., (1966). Pressure difference for a nine-storey building as a result of chimney effect and ventilation system operation. *ASHRAE Transactions*. 72, 180-189.

Trung, V.T., Tamura, Y., and Yoshida, A., (2010). Numerical computation for lower surfacepressures on a porous sunshade roof cover sheet. *Proceedings of the 5th International Symposium on Computational Wind Engineering.* Chapel Hill, North Carolina, USA.

Uvslokk, S., (1996). The importance of wind barriers for insulated timber frame constructions. *J. Build. Phys.* 20(1): 40-62.

Van Bentum, C., Kalkman, I., and Geurts, C., (2012). Towards a better understanding of pressure equalization. *The Seventh International Colloquium on Bluff Body Aerodynamics and Applications.* Shanghai, China.

Van Schijndel, A., and Schols, S., (1998). Modeling pressure equalization in cavities. *J. Wind Eng. Ind. Aerodyn.* 74-76:641-649.

Van Straaten, R.A., (2017). Pressure Equalization of Wind-Induced Pressures on Residential Vinyl Siding Cladding in Full-Scale. *Electronic Thesis and Dissertation Repository*. 4940.

Vickery, B., (1986). Gust factors for internal pressures in low-rise buildings. *J. Wind Eng. Ind. Aerodyn.* 23(1): 259-271.

Wu, C.H., Akon, A., Kopp, G.A., (2017). Effects of turbulence on the mean pressure field in the separated-reattaching flow above a low-rise building. *J. Wind Eng. Ind. Aerodyn.* 171, 79-92.

Xie, J., Schuyler, G.D., and Resar, H.R., (1992). Prediction of net pressure on pressure equalized cavities. *J. Wind Eng. Ind. Aerodyn.* 41-44: 2449-2460.

Curriculum Vitae

Name: Connell S. Miller

Post-secondary   Western University
Education and   London, Ontario, Canada
Degrees: 2011 - 2015 B.E.Sc.

Honours and   Dean's Honour List
Awards: 2011-2015

                        3rd Place – Engineering
                        Three Minute Thesis
                        2016

                        Best Paper
                        15th International Conference on Wind Engineering
                        2019

Related Work   Teaching Assistant
Experience   Western University
                        2015 - 2020

                        Visiting Scientist
                        Insurance Institute for Business & Home Safety
                        2017

                        Building Science Assistant
                        RDH Building Science
                        2018 - 2019

                        Research Engineer
                        Northern Tornadoes Project
                        2018 - 2020

Publications:

Miller, C.S., Kopp, G.A., Morrison, M.J., Kemp G., and Drought, N., (2017). A multichamber, pressure-based test method to determine wind loads on air-permeable, multilayer cladding systems. *Front. Built Env.* 3:7.

Miller, C.S., Kopp, G.A., Morrison, M.J., (2020). Aerodynamics of air-permeable multilayer roof cladding. Submitted to *J. Wind Eng. Ind. Aerodyn.* on October 20, 2019.